2005

Chip-scale bioassays based on surface-enhanced Raman scattering: fundamentals and applications

Hye-Young Park
Iowa State University

Chip-scale bioassays based on surface-enhanced Raman scattering: Fundamentals and applications

by

Hye-Young Park

A dissertation submitted to the graduate faculty

in partial fulfillment of the requirements for the degree of

DOCTOR OF PHILOSOPHY

Major: Analytical Chemistry

Program of Study Committee:
Marc D. Porter, Major Professor
Edward S. Yeung
Robert S. Houk
Victor S.-Y. Lin
Nancy Cornick

Iowa State University

Ames, Iowa

2005

Graduate College
Iowa State University

This is to certify that the doctoral dissertation of

Hye-Young Park

has met the dissertation requirements of Iowa State University

Signature was redacted for privacy.

Major Professor

Signature was redacted for privacy.

For the Major Program

TABLE OF CONTENTS

ACKNOWLEDGMENTS

I would like to greatly thank my advisor, Professor Marc D. Porter, for his guidance, patience, encouragement, and support throughout my graduate studies. To Marc, thank you for understanding me and keeping me motivated even through the many frustrations of my research.

I would like to also thank Dr. Robert J. Lipert who became my second advisor, for sharing knowledge of various topics and giving me insights regarding my research projects. Discussions with members of the Raman subgroup, especially Dr. Robert J. Lipert and Jeremy Driskell are also greatly appreciated. I would like to thank all the other past and present members of the research group for the helpful discussions and friendships. In particular, thanks to Hajime Takano for guiding me when I started my research four years ago and to Becky Staedtler for making the work place more enjoyable.

I would like to personally thank my parents, sister, and brother for their unconditional love and support. Finally, I would like to thank my husband for his love, understanding, and humor.

This work was performed at the Institute for Combinatorial Discovery and Ames Laboratory under Contract No. W-7405-Eng-82 with the U.S. Department of Energy. The United States government has assigned the DOE Report number IS-T-1935 to this thesis.

ABSTRACT

This work explores the development and application of chip-scale bioassays based on surface-enhanced Raman scattering (SERS) for high throughput and high sensitivity analysis of biomolecules.

The size effect of gold nanoparticles on the intensity of SERS is first presented. A sandwich immunoassay was performed using Raman-labeled immunogold nanoparticles with various sizes. The SERS responses were correlated to particle densities, which were obtained by atomic force microscopy (AFM). The response of individual particles was also investigated using Raman-microscope and an array of gold islands on a silicon substrate. The location and the size of individual particles were mapped using AFM.

The next study describes a low-level detection of *Escherichia coli* O157:H7 and simulants of biological warfare agents in a sandwich immunoassay format using SERS labels, which have been termed Extrinsic Raman labels (ERLs). A new ERL scheme based on a mixed monolayer is also introduced. The mixed monolayer ERLs were created by covering the gold nanoparticles with a mixture of two thiolates, one thiolate for covalently binding antibody to the particle and the other thiolate for producing a strong Raman signal.

An assay platform based on mixed self-assembled monolayers (SAMs) on gold is then presented. The mixed SAMs were prepared from dithiobis(succinimidyl undecanoate) (DSU) to covalently bind antibodies on gold substrate and oligo(ethylene glycol)-terminated thiol to prevent nonspecific adsorption of antibodies. After the mixed SAMs surfaces, formed from various mole fraction of DSU were incubated with antibodies, AFM was used to image individual antibodies on the surface.

The final study presents a collaborative work on the single molecule adsorption of YOYO-I labeled λ-DNA at compositionally patterned SAMs using total internal reflection fluorescence microscopy. The role of solution pH, λ-DNA concentration, and domain size was investigated. This work also revealed the potential importance of structural defects.

CHAPTER 1. GENERAL INTRODUCTION

Dissertation Organization

This dissertation describes the development and application of surface-enhanced Raman scattering (SERS) based immunoassay biochips. A general introduction and overview of the research is presented in this chapter. The first two data chapters (Chapter 2 and 3) describe efforts to develop biochips based on immunoassays using surface-enhanced Raman scattering (SERS). In Chapter 2, the size effect of gold nanoparticles on the SERS signal is studied. In Chapter 3, the detection of *Escherichia coli* (*E. coli*) O157:H7 and simulants of biological warfare agents using SERS as sensitive and rapid method for biochip readout is presented. The last two data chapters (Chapter 4 and 5) explore the use of self-assembled monolayers (SAMs) in biochip development. In Chapter 4, an assay platform surface using a mixed monolayer is introduced, and in Chapter 5, the interactions and adsorption behavior of DNA on compositionally patterned SAMs is investigated as an approach to examine the nonspecific adsorption of biomolecules on solid surfaces.

The first part of the general Introduction section describes SAMs and specific forms of SAMs that are used throughout the later data chapters, followed by general aspects and various types of immunoassay formats. The last part of the Introduction provides the basics of SERS via a brief overview of electromagnetic theory and then some of its more intriguing applications in biotechnology.

Self-assembled monolayers (SAMs) for biological studies

The stability and the chemical/biological variability of SAMs have led to their widespread use. There are many SAM systems, such as organoalkanethiolate on gold or silver, organosilicon on oxides, and carboxylic acid on metal oxides. Among them, SAMs on gold is the most studied experimentally and theoretically.[1-5] Alkanethiolates are generally composed of three regions: a sulfur head group, a polymethylene or aromatic spacer group, and an end or terminal group (Figure 1). Thiols chemisorb to gold via the sulfur head group while the alkyl chain provides additional stability from interchain van der Waals or π–π stacking forces, leading to well-ordered 2D structures. The surface characteristics of SAMs are typically controlled by the end group functionality, which can be readily varied synthetically. Because of the ability to modify its surface in one simple step, SAMs on gold have been widely used as a model of bio-surfaces as well as platform for sensor construction. In this part of the Introduction, four of the SAM systems often used in those applications are discussed.

Covalent coupling of biomolecules on SAMs. The immobilization of biomolecules (bioimmobilization) such as antibodies onto solid surface provides an excellent approach to optical and electrochemical sensing. Immobilization can be achieved by physical adsorption, covalent binding, entrapment in membranes, and microencapsulation into polymers and hydrogels.[6] Among them, stable covalent coupling not only allows use of the harsh washing steps in immunoassays, but also results in an increased operational stability. Covalent binding methods with SAMs have employed various end group functionalities (e.g., succinimidyl[7-9] and photoactive groups[10]).

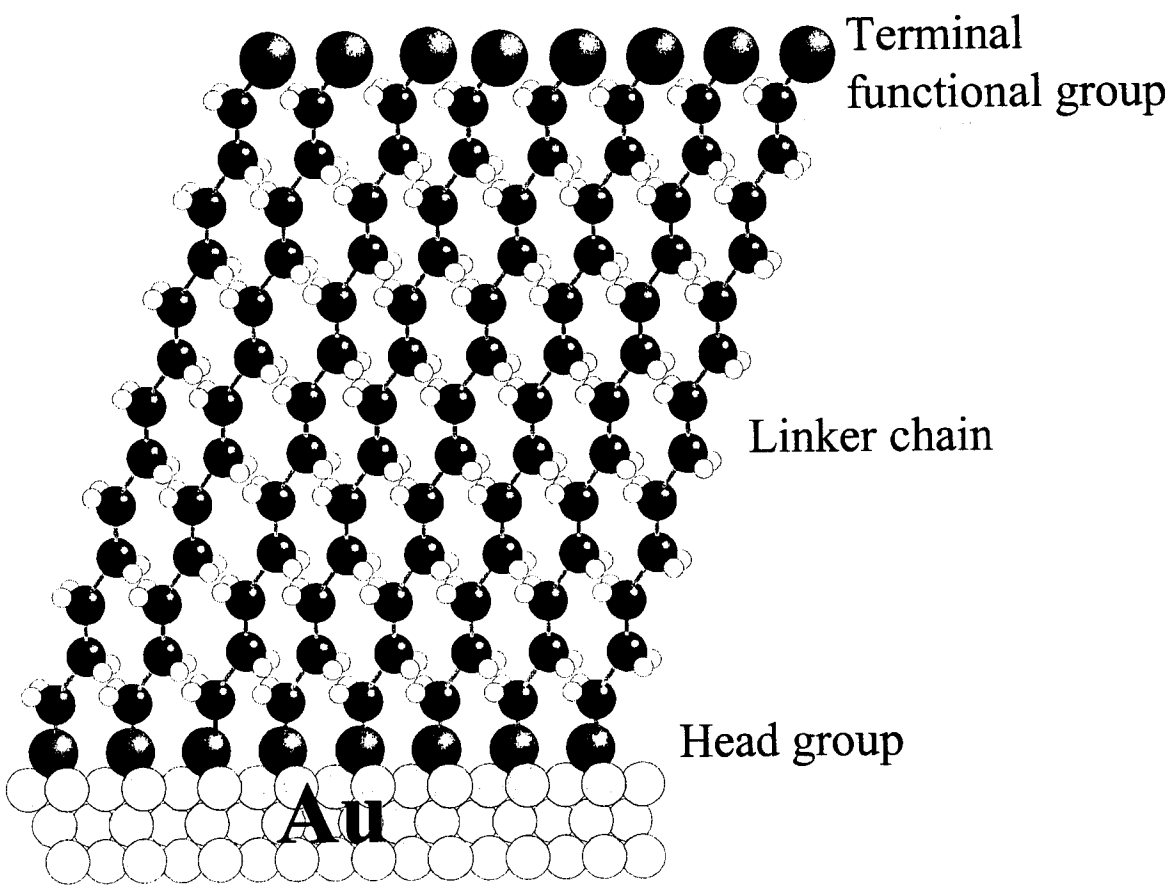

Figure 1. Idealized representation of self-assembled alkanethiolate monolayer on gold.

In this dissertation, covalent coupling is based on SAMs with a succinimidyl functional group and is applied not only for immobilization of antibodies on flat gold substrates but also on gold nanoparticles. SAMs formed from dithiobis(succinimidylundecanoate) (DSU) have been utilized to immobilize a wide variety of biomolecules such as antibodies,[11,12] and enzymes.[7] This dissertation has made exclusive use of SAMs formed from dithiobis(succinimidylpropionate) (DSP) and dithiobis(succinimidylnitrobenzoate) (DSNB), as well as DSU. The succinimidyl end group readily reacts with primary amines in proteins by nucleophilic attack. This reaction forms an amide linkage, resulting in covalent binding of the protein onto the SAM and therefore to gold.

SAMs that resist protein binding. Preventing the nonspecific adsorption of biomolecules is critical in many areas of biotechnology such as biomaterials,[13] tissue engineering,[14-16] drug delivery,[17,18] and biosensors.[19] The most well known surface that resists protein adsorption is poly(ethylene glycol) (PEG). The mechanism for PEG to resist protein adsorption is explained by "conformational freedom".[20-24] Pale-Grosdemange *et al.* explored this idea further by introducing SAMs that present short oligomers of EG, or oligo(ethylene golycol) (OEG), where EGn, n=3-6, on gold.[25] Thereafter, a host of experimental[26-29] and theoretical[30,31] studies have shown these compounds to be effective for resisting the nonspecific adsorption of proteins. While the mechanism by which PEG resists protein adsorption has been detailed extensively, that for OEG is not fully understood. Protein resistance of PEG via "conformation freedom" can be explained by a water barrier mechanism. [32-34] Water molecules tightly bound at PEG interface form a physical barrier

that prevents contact between the protein and the surface. OEG forms a compact monolayer, which restricts conformational freedom.

Grunze *et al.* used a steric repulsion model to compare the mechanism of protein adsorption on OEG SAMs to that of PEG in order to determine how the conformations affect the ability to prevent protein adsorption.[35] They found that EG3OMe exists in different forms when assembled on gold and silver. The OEG moiety formed all trans conformations when adsorbed on silver, but formed helical structure on gold. Interestingly, the EG3OMe-SAM on gold prevented fibrinogen adsorption, but not when adsorbed on silver. They hypothesized the uptake of water into the interior of the adlayer by the OEG moieties is central to the ability to resist protein adsorption and that the greater the solvation of the adlayer, the greater the ability to resist protein adsorption. Shortly thereafter, a sum frequency generation study in the Grunze Laboratory showed that the structural order in EG3OMe SAMs is affected by presence of water solvent.[36] Monte Carlo simulations by Pertsin *et al.* confirmed that a significant number of water molecules can penetrate into the helical-SAM formed on a gold surface, which induces a conformational disordering of the SAM due to the oxygen atoms which induces a hydrogen bonding with the water molecules. On the other hand, the trans-SAM on silver was much more resistant to the penetration of water. Finally, an ab initio calculation also demonstrated that the incorporation of water molecules is favorable in helical SAMs and unfavorable in the all-trans SAMs. [32,37,38]

Although the origin of protein resistance is not fully understood, other surfaces[39-41] have been explored and showed an ability to resist protein adsorption. The functional groups studied include zwitterionic-,[42,43] galactose-,[44] triprophylene sulfoxide-,[45] maltose-terminated[26] SAMs and mannitol groups.[46] At present, however, there is no all

encompassing theory that describes these observations.

Mixed SAMs. Mixed SAMs serve as an experimental system to study interactions of biomolecules with surfaces by tailoring the surface chemical and structural properties. They can also provide means to control gradients of composition, which can also be of value in studies of biomolecules adsorption and manipulation. Mixed SAMs can be formed by co-adsorption from thiol or disulfide mixtures, or by adsorption of asymmetric disulfides. Studies show that the homogeneity and preferential adsorption of these precursors can be affected by chain length, head group, tail group, and solvent.[47,48] When two components with different chain lengths were used, the mixed monolayer phase segregated due to a thermodynamically controlled process. In ethanol, the favorable adsorption of one component over the other was controlled by solubility and ability to form intra-monolayer hydrogen bonds.[47] In a Monte Carlo simulation, Shevade *et al.* found that the mixed monolayer exhibits phase segregation when the chain length difference was more than three carbon atoms, with the longer chain component showing preferential adsorption.[49]

A more interesting form of mixed monolayer can be formed when EG3OMe is mixed with a SAM that can bind biomolecules. This type of mixed monolayer provides a system that can control the surface density of biomolecules, while minimizing protein nonspecific adsorption. In Chapter 2, mixed monolayers formed from EG3OMe and DSU are studied as a route to control the surface density of anti-prostate specific antigen.

Patterned SAMs. Patterned SAMs have multiple components in predetermined spatial locations. Importantly, patterned SAMs can be used to control the spatial positioning and lateral distribution of protein, DNA, and cells, which are important in biology, bioengineering, and biochemical purposes.[13,50-52] The patterning can be achieved

by the spatially selective removal of particular SAMs, placement of SAMs, or reaction of SAMs.

SAMs can be patterned by soft lithography (microcontact printing), photolithography, or scanning probe lithography (SPL). Since Whitesides *et al.* introduced soft lithography, there have been studies utilizing this technique to construct two dimensional features at the nanometer to micrometer scales.[50,53-55] This method uses elastomeric polymers such as polydimethylsiloxane (PDMS) to function as stamps. A PDMS stamp is first immersed in an alkanethiol solution and dried. The stamp is then gently pressed onto a gold substrate, with the inked thiols are transferred from the stamp. Then, the non-patterned (i.e., uncoated) areas can be filled with a second component by its adsorption from solution. The method is rapid and cost-effective. The patterned SAMs produced by this method are as stable as those formed from solution.

Patterning SAMs with UV irradiation uses photographic masks.[56] This method is utilized in formation of compositionally patterned SAMs to study the adsorption behavior of DNA at the liquid-solid interface (Chapter 3). When SAMs on gold are exposed to UV radiation, they are photooxidized by ozone to form oxidized sulfur groups, which can be easily removed with water or other mild solvents. By immersing the SAMs in the second-component thiol solution, compositionally patterned substrates are prepared. In Chapter 3, transmission electron microscopy (TEM) grids are used as photomasks.

SPL patterns SAMs by atomic force microscopy (AFM) or scanning tunneling microscopy (STM). In these techniques, the tip can act as a "pen" to "write" patterns on the surface.[57,58] Mirkin *et al.* developed a new technique called dip-pen nanolithography, which

is a type of SPL.[59-61] Alkanethiol molecules are transferred by AFM tip via capillary action between the tip and sample.

Immunoassays

Immunoassays are a type of analytical method that utilizes antibodies as analytical reagents for the specific recognition of analytes (antigen), often biomolecules.[62,63] A small portion of the antigen surface, the epitope, can bind to the recognition site, a paratope, on the complementary antibody. Based on X-ray diffraction, the molecular interaction between epitope and paratope takes 15-22 amino acid residues of the epitope, with a surface area of about 700-900 $Å^2$.[64,65] These residues are often arranged in a discontinuous configuration, indicating the importance of tertiary structure. The attraction forces between paratope and epitope are from hydrophobic, electrostatic interactions, van der Waals, and hydrogen bonds.

Immunoassays find wide applications in many areas such as clinical science,[66-68] environmental analysis,[69,70] and food industry.[71-73] A major development in these fields is the use of immunosensors based on heterogeneous immunoassays, including surface plasmon resonance (SPR), enzyme-linked immunosorbent assay (ELISA), and fluorescence based immunoassay.

ELISA is by far the most widely used immunoassay method and has become an industry standard.[74-84] ELISA utilizes enzymes as a signal amplifying method. Typical assay procedures involve capture of target analytes into culture wells followed by incubation with antibody. Then, a secondary antibody tagged with enzyme is added to each well. The activity of the enzyme is measured by various methods such as colorimetry and

fluorometry, depending upon the type of enzyme. Horseradish peroxidase (HRP) is the most common enzyme label due to its colorimetric sensitivity.

In fluorescence-based immunoassays, the detection antibody is labeled with fluorescent molecules. The most widely used fluorophores are fluorescein, rhodamine, and umbelliferone derivatives. [85-88] However, fluorescein and rhodamine show only a small Stoke's shift and umbelliferones have a low quantum yield and short emission wavelengths. Time-resolved fluorescence based assays utilize probes with chelates (such as europium ion) with lifetimes much longer than that of other fluorophores to minimize the interference from background fluorescence.[89-99] However, this method still suffers from the general limitations of fluorescence such as light scattering and quenching, which reduces sensitivity dramatically. Also, contamination of enhancement reagent with europium ion in the environment is problematic.

Immunoassay methods without labels, such as SPR, provide simple and rapid assays, and detection limits of 10^{-9} to 10^{-13} M have been reported.[94-103] There have been several successful commercializations of SPR immunosensors. SPR detects changes in the refractive index of a material supported on a thin metal film. The oscillation of electron clouds (surface plasmon) absorbs the evanescent field generated by total internal reflection. The total internal reflection light intensity is plotted as a function of incidence angle and this plot produces a profile with a sharp dip at the angle that generates a resonant condition. When molecules bind on the metal surface, the refractive index changes and shifts the angle of minimum reflection intensity. SPR-based immunosensors show promise especially in the real-time determination of concentration, kinetic constant, and binding specificity of

biomolecules. However, it suffers from interference by changes in the refractive index or temperature.

Our immunoassay, which will be introduced in Chapter 2 and 3, is a sandwich type immunoassay. It uses a novel labeling scheme based on surface-enhanced Raman scattering (SERS). SERS shows large scattering enhancements from molecules adsorbed on nanometrically rough metal structures. In our detection scheme, gold nanoparticles are used as the enhancing medium. Gold nanoparticles modified with Raman reporter molecules and antibodies exhibit strong, biospecific Raman signals. Since, Raman bands are much narrower than those of fluorescence, these Raman labeled immunogold particles, also called extrinsic Raman labels (ERLs), have a strong potential for multiplexing. Chapter 3 describes the use of ERLs in the detection of biological warfare agents and *E.coli* O157:H7. Also, an alternative design of ERL is introduced.

Surface-Enhanced Raman scattering

When the strong Raman signal of pyridine adsorbed on roughened silver electrode surfaces was first observed, Fleishmann et al. attributed this signal to the increased surface area due to a roughening process.[104] However, Jeanmire and Van Duyne[105] and Albrecht and Creighton[106] later independently discovered that the strong Raman signal could not be explained simply by an increase in surface area increasing the number of scatterers. Jeanmire and Van Duyne proposed an electric field enhancement mechanism. Since its discovery, there have been a large number of studies aimed at understanding and explaining the phenomenon. It is generally agreed that SERS enhancement is largely due to electromagnetic (EM) enhancement. In EM enhancement theory, upon irradiation, free

electrons in a roughened metal or a particulate absorb the radiation and oscillate with a resonance frequency determined by the dielectric function of the metal, i.e., the surface plasmon resonance. In this resonance condition, the incident field is greatly increased. In SERS, not only there is an enhancement in this incident field but also an enhancement in the scattered field in shifted frequency (Raman frequency) due to the presence of the metal substrate.

There are many versions of EM theory with different levels of sophistication. Models have been developed to treat spheres, spheroidal particles, interacting spheres, hemispheres and gratings. The simplest model is isolated spherical particles.[107] So, let us consider the isolated spheroidal metal particle coated with Raman scattering molecules. When the particle is irradiated with incident field E_i at frequency ω_0, three different types of fields are generated. Those are Lorenz-Mie scattering by the particle (E_{LM}), Raman scattering by the adsorbed molecule (E_{DIP}), and the field that results from scattering of Raman radiation by the particle (E_{SC}). The Lorenz-Mie scattering (E_{LM}) can be calculated using Lorenz-Mie theory. E_{DIP} is proportional to E_i and E_{LM}. E_{SC} is more complex and must be computed by solving the appropriate boundary value problem at the Raman frequency (ω).[107,108]

The enhancement factor G at the surface of the particle is given by,

$$G \equiv \left\langle \left| \mathbf{E}_p^{\,2} \right| \right\rangle / E_i^{\,2} \times \left\langle \left| \mathbf{E}_R^{\,2} \right| \right\rangle / E_i^{\,2} = 5 \left| 1+2g_0+2g+4gg_0 \right|^2 \qquad (1)$$

where $\left\langle \left| \mathbf{E}_p^{\,2} \right| \right\rangle$ is mean square field intensity from E_i and and E_{LM}, and $\left\langle \left| \mathbf{E}_R^{\,2} \right| \right\rangle$ is the mean square field intensity from E_{DIP} and E_{SC}, respectively. The values g and g_0 are $(\varepsilon-1)/(\varepsilon+2)$ evaluated at ω and ω_0, respectively and correspond to enhancements of the local fields at

each frequency (ω and ω_0). When real part of dielectric function (ε) approaches -2 (resonant condition), the above equation is dominated by the gg_0 term and the enhancement factor becomes,

$$G=80\,|\,gg_0\,|^2 \qquad (2)$$

When the frequency shift is small, then $g \sim g_0$, and the overall enhancement increases roughly as fourth power of the enhancement in the local incident field. Therefore, a small increase in the local field can generate large enhancements in Raman scattering. The maximum calculated values of EM enhancement for isolated spheroidal silver and gold particles are on the order of 10^6-10^7.[109,110] The coinage metals are useful SERS substrates because the resonance condition is satisfied at the visible frequencies widely used in Raman spectroscopy.

Schatz and co-workers calculated the peak value for G (optimized with respect to wavelength) vs. radius (semi major axis for spheroidal particles) and showed that for gold particles smaller than 150 nm, *R* increases as the size of the particle increases.[110] They also calculated the wavelength at which the maximum in G occurs as a function of radius and found that the optimum wavelength increases as the radius increases.

The simple model above qualitatively explains most of the experimental observations. There have been works concerned with different model systems such as two coupled particles,[111] and many coupled particles and gratings.[112-114] However, more improvements are still required on matching the surface modeled and that experimentally tested.

Research efforts continue to explore the applicability of SERS for the very low-level detection of a variety of bioanalytes and the real-time monitoring of the movement of

different biological molecules such as neurotransmitters and cytochrome c.[115-117] With very narrow spectral bands and high sensitivity, SERS has potential to be used as a nearly perfect read-out method for the labels in immunoassays. In an earlier application of SERS in immunoassay, Rohr *et al.* detected thyroid-stimulating hormone (TSH) by performing a sandwich immunoassay on silver film.[118] A silver film coated with anti-TSH captured TSH, then the detection anti-TSH labeled with resonance dye *p*-dimethylaminoazobenzene was added. When the detection anti-TSH was bound on the TSH, the resonance SERS signal was observed. Another immunoassay based on SERS was introduced by our research group.[119] The immunoassay utilized colloidal gold as the SERS-active material. Gold particles are labeled with both organic Raman reporter molecules and antibodies. By covering gold particles with different combinations of antibodies and Raman labels, Ni et al. reported simultaneous detection of rabbit and rat IgG molecules.[119] Later, using a different design of Raman labeled immunogold nanoparticles, femtomolar detection of free-prostate specific antigen[120] and low level detection of virus were reported.[121] Dou *et al.* introduced an enzyme immunoassay for mouse IgG using SERS of the enzyme reaction product.[122] When a secondary antibody labeled with peroxidase was reacted with o-phenylenediamine, azoaniline was produced. The product is adsorbed on colloidal silver particles generating a SERS spectrum. The detection of an enzymatic product was also demonstrated for the membrane bound enzymes in cells.[123]

While the most exciting aspect in biological applications is trace analytical capabilities, SERS still suffers from lack of reproducibility, mainly originating from the fact that the label must be bound to a SERS active substrate. This weakness in reproducibility originates from the irreproducibility in consistently creating SERS active substrates. The

efforts to create SERS substrates with higher reproducibility include self assembly of gold colloids[124] and high quality metal films.[125] Overall, with its excellent features such as photostability and narrow spectral bands, SERS has a bright future in the analytical arena as the reproducibility can be improved as developments in nanotechnology provide better control on SERS active materials. Moreover, instrumental advances in the size, efficiency in spectrometers, and charge-coupled devices promise to further development of SERS-based applications.

Dissertation Overview

Chapter 2 is a study of the effect of the size of gold particles on SERS intensity. Two different systems are employed. In one system, the average SERS intensity was obtained by combining AFM particle counts and SERS measurements on assay substrates. In the second system, the SERS signal from individual particles was recorded for particles with different sizes.

Chapter 3 shows the application of ERLs in the detection of the pathogen *E. coli* O157:H7 and simulants of biological warfare (BW) agents.

Chapter 4 presents the study antibody immobilization on a mixed monolayer system. The effect of solution composition ratio on the protein coverage is studied using atomic force microscopy.

Chapter 5 investigates the non-specific interaction of DNA with compositionally patterned SAMs. The effect of solution pH, topography, and surface heterogeneity on the adsorption of DNA is discussed.

Refererences

(1) Tengvall, P.; Lundstrom, I.; Liedberg, B. *Biomaterials* **1998**, *19*, 407-422.

(2) Tidwell, C. D.; Ertel, S. I.; Ratner, B. D.; Tarasevich, B.; Atre, S.; Allara, D. L. *Langmuir* **1997**, *13*, 3404-3413.

(3) Ulman, A. *Chem. Rev.* **1996**, *96*, 1533-1554.

(4) Allara, D. L.; Dunbar, T. D.; Weiss, P. S.; Bumm, L. A.; Cygan, M. T.; Tour, J. M.; Reinerth, W. A.; Yao, Y.; Kozaki, M.; Jones, L., II *Ann. New York Acad. Sci.* **1998**, *852*, 349-370.

(5) Love, J. C.; Estroff, L. A.; Kriebel, J. K.; Nuzzo, R. G.; Whitesides, G. M. *Chem. Rev.(Washington, DC, United States)* **2005**, *105*, 1103-1169.

(6) Jin, W.; Brennan, J. D. *Anal. Chim. Acta* **2002**, *461*, 1-36.

(7) Zaugg, F. G.; Spencer, N. D.; Wagner, P.; Kernen, P.; Vinckier, A.; Groscurth, P.; Semenza, G. *J. Mater. Sci.: Mater. Med.* **1999**, *10*, 255-263.

(8) Wagner, P.; Hegner, M.; Kernen, P.; Zaugg, F.; Semenza, G. *Biophys. J.* **1996**, *70*, 2052-2066.

(9) Wagner, P.; Kernen, P.; Hegner, M.; Ungewickell, E.; Semenza, G. *FEBS Lett.* **1994**, *356*, 267-271.

(10) Delamarche, E.; Sundarababu, G.; Biebuyck, H.; Michel, B.; Gerber, C.; Sigrist, H.; Wolf, H.; Ringsdorf, H.; Xanthopoulos, N.; Mathieu, H. J. *Langmuir* **1996**, *12*, 1997-2006.

(11) Grubor, N. M.; Shinar, R.; Jankowiak, R.; Porter, M. D.; Small, G. J. *Biosens. Bioelectron.* **2004**, *19*, 547-556.

(12) Bowen, J.; Noe, L. J.; Sullivan, B. P.; Morris, K.; Martin, V.; Donnelly, G. *Appl. Spectrosc.* **2003**, *57*, 906-914.

(13) Kasemo, B. *Surf. Sci.* **2002**, *500*, 656-677.

(14) Niklason, L. E. *Science (Washington, D.C.)* **1999**, *286*, 1493-1494.

(15) Tampieri, A.; Celotti, G.; Landi, E.; Sandri, M.; Roveri, N.; Falini, G. *J. Biomed. Mater. Res., A* **2003**, *67A*, 618-625.

(16) Lee, L. K.; Roth, C. M. *Curr. Opin. Biotechnol.* **2003**, *14*, 505-511.

(17) Santini, J. T., Jr.; Cima, M. J.; Langer, R. *Nature (London)* **1999**, *397*, 335-338.

(18) Stayton, P. S. *Trends Biotechnol.* **2003**, *21*, 465-467.

(19) Holland, N. B.; Qiu, Y.; Ruegsegger, M.; Marchant, R. E. *Nature (London)* **1998**, *392*, 799-801.

(20) Desai, N. P.; Hubbell, J. A. *Biomaterials* **1991**, *12*, 144-153.

(21) Jeon, S. I.; Lee, J. H.; Andrade, J. D.; De Gennes, P. G. *J. Colloid Interface Sci.* **1991**, *142*, 149-158.

(22) Jeon, S. I.; Andrade, J. D. *J. Colloid Interface Sci.* **1991**, *142*, 159-166.

(23) Szleifer, I. *Biophys. J.* **1997**, *72*, 595-612.

(24) Halperin, A. *Langmuir* **1999**, *15*, 2525-2533.

(25) Pale-Grosdemange, C.; Simon, E. S.; Prime, K. L.; Whitesides, G. M. *J. Am. Chem. Soc.* **1991**, *113*, 12-20.

(26) Prime, K. L.; Whitesides, G. M. *Science (Washington, D.C.)* **1991**, *252*, 1164-1167.

(27) Feldman, K.; Haehner, G.; Spencer, N. D.; Harder, P.; Grunze, M. *J. Am. Chem. Soc.* **1999**, *121*, 10134-10141.

(28) Schwendel, D.; Dahint, R.; Herrwerth, S.; Schloerholz, M.; Eck, W.; Grunze, M. *Langmuir* **2001**, *17*, 5717-5720.

(29) Zhu, B.; Eurell, T.; Gunawan, R.; Leckband, D. *J. Biomed. Mater. Res.* **2001**, *56*, 406-416.

(30) Zheng, J.; Li, L.; Tsao, H.-K.; Sheng, Y.-J.; Chen, S.; Jiang, S. *Biophys. J.* **2005**, *89*, 158-166.

(31) Pertsin, A. J.; Hayashi, T.; Grunze, M. *J. Phys. Chem. B* **2002**, *106*, 12274-12281.

(32) Pertsin, A. J.; Grunze, M. *Langmuir* **2000**, *16*, 8829-8841.

(33) Archambault, J. G.; Brash, J. L. *Colloids Surf., B* **2004**, *33*, 111-120.

(34) Zheng, J.; Li, L.; Chen, S.; Jiang, S. *Langmuir* **2004**, *20*, 8931-8938.

(35) Harder, P.; Grunze, M.; Dahint, R.; Whitesides, G. M.; Laibinis, P. E. *J. Phys. Chem. B* **1998**, *102*, 426-436.

(36) Zolk, M.; Eisert, F.; Pipper, J.; Herrwerth, S.; Eck, W.; Buck, M.; Grunze, M. *Langmuir* **2000**, *16*, 5849-5852.

(37) Pertsin, A. J.; Grunze, M.; Garbuzova, I. A. *J. Phys. Chem. B* **1998**, *102*, 4918-4926.

(38) Wang, R. L. C.; Kreuzer, H. J.; Grunze, M. *J. Phys. Chem. B* **1997**, *101*, 9767-9773.

(39) Holmlin, R. E.; Chen, X.; Chapman, R. G.; Takayama, S.; Whitesides, G. M. *Langmuir* **2001**, *17*, 2841-2850.

(40) Ostuni, E.; Chapman, R. G.; Liang, M. N.; Meluleni, G.; Pier, G.; Ingber, D. E.; Whitesides, G. M. *Langmuir* **2001**, *17*, 6336-6343.

(41) Chapman, R. G.; Ostuni, E.; Yan, L.; Whitesides, G. M. *Langmuir* **2000**, *16*, 6927-6936.

(42) Chen, S.; Zheng, J.; Li, L.; Jiang, S. *J. Am. Chem. Soc.* **2005**, *127*, 14473-14478.

(43) Kitano, H.; Kawasaki, A.; Kawasaki, H.; Morokoshi, S. *J. Colloid Interface Sci.* **2005**, *282*, 340-348.

(44) Hederos, M.; Konradsson, P.; Liedberg, B. *Langmuir* **2005**, *21*, 2971-2980.

(45) Deng, L.; Mrksich, M.; Whitesides, G. M. *J. Am. Chem. Soc.* **1996**, *118*, 5136-5137.

(46) Luk, Y.-Y.; Kato, M.; Mrksich, M. *Langmuir* **2000**, *16*, 9604-9608.

(47) Bain, C. D.; Evall, J.; Whitesides, G. M. *J. Am. Chem. Soc.* **1989**, *111*, 7155-7164.

(48) Bain, C. D.; Whitesides, G. M. *J. Am. Chem. Soc.* **1989**, *111*, 7164-7175.

(49) Shevade, A. V.; Zhou, J.; Zin, M. T.; Jiang, S. *Langmuir* **2001**, *17*, 7566-7572.

(50) Kumar, A.; Biebuyck, H. A.; Whitesides, G. M. *Langmuir* **1994**, *10*, 1498-1511.

(51) Castner, D. G.; Ratner, B. D. *Surf. Sci.* **2002**, *500*, 28-60.

(52) Tirrell, M.; Kokkoli, E.; Biesalski, M. *Surf. Sci.* **2002**, *500*, 61-83.

(53) Kumar, A.; Abbott, N. L.; Biebuyck, H. A.; Kim, E.; Whitesides, G. M. *Acc. Chem. Res.* **1995**, *28*, 219-226.

(54) Kumar, A.; Whitesides, G. M. *Appl. Phys. Lett.* **1993**, *63*, 2002-2004.

(55) Xia, Y.; Whitesides, G. M. *Ann. Rev. Mat. Sci.* **1998**, *28*, 153-184.

(56) Tarlov, M. J.; Burgess, D. R. F., Jr.; Gillen, G. *J. Am. Chem. Soc.* **1993**, *115*, 5305-5306.

(57) Kenseth, J. R.; Harnisch, J. A.; Jones, V. W.; Porter, M. D. *Langmuir* **2001**, *17*, 4105-4112.

(58) Hong, S.; Mirkin, C. A. *Science (Washington, D.C.)* **2000**, *288*, 1808-1811.

(59) Piner, R. D.; Zhu, J.; Xu, F.; Hong, S.; Mirkin, C. A. *Science (Washington, D.C.)* **1999**, *283*, 661-663.

(60) Demers, L. M.; Ginger, D. S.; Park, S. J.; Li, Z.; Chung, S. W.; Mirkin, C. A. *Science(Washington, D.C.)* **2002**, *296*, 1836-1838.

(61) Smith, R. K.; Lewis, P. A.; Weiss, P. S. *Prog. Surf. Sci.* **2004**, *75*, 1-68.

(62) Price, C. P.; Newman, D. J.; Editors *Principles and Practice of Immunoassay*, 1991.

(63) Hage, D. S. *Anal. Chem.* **1999**, *71*, 294R-304R.

(64) Price, C. P. *Clin. Chem. Lab. Med.* **1998**, *36*, 341-347.

(65) Dwek, R. A.; Wain-Hobson, S.; Dower, S.; Gettins, P.; Sutton, B.; Perkins, S. J.; Givol, D. **1977**, *266*, 31-37.

(66) Van Enk, R. A.; James, K. K.; Thompson, K. D. *Am. J. Clin. Pathol.* **1991**, *95*, 428-434.

(67) Tsikas, D. *Clin. Chim. Acta; Int. J. Clin. Chem.* **2004**, *344*, 215-217.

(68) Luppa, P. B.; Sokoll, L. J.; Chan, D. W. *Clin. Chim. Acta* **2001**, *314*, 1-26.

(69) Neilson, J. W.; Maier, R. M. *Humic Substances and Chemical Contaminants, Proceedings of a Workshop and Symposium, Anaheim, CA, United States, Oct. 26-27,***2001**, 255-273.

(70) Lee, J. K.; Ahn, K. C.; Stoutamire, D. W.; Gee, S. J.; Hammock, B. D. *J. Agric. Food Chem.* **2003**, *51*, 3695-3703.

(71) Clemente, A.; Chambers, S. J.; Lodi, F.; Nicoletti, C.; Brett, G. M. *Food Control* **2003**, *15*, 65-69.

(72) Henry, J.; Anand, A.; Chowdhury, M.; Cote, G.; Moreira, R.; Good, T. *Anal. Biochem.***2004**, *334*, 1-8.

(73) Sarter, S.; Zakhia, N. *Luminescence* **2004**, *19*, 345-351.

(74) Castillo, M.; Oubina, A.; Barcelo, D. *Environ. Sci. Technol.* **1998**, *32*, 2180-2184.

(75) Ferrin, N. H.; Fang, Y.; Johnson, C. R.; Murtaugh, M. P.; Polson, D. D.; Torremorell, M.; Gramer, M. L.; Nelson, E. A. *Clin. Diagnostic. Lab. Immunol.* **2004**, *11*, 503-514.

(76) Arkel, Y. S.; Ku, D.-H. W.; Le, P.; Carr, A. M. *Thromb. Haemostasis* **2001**, *86*, 1127-1128.

(77) Pickering, J. W.; Martins, T. B.; Schroder, M. C.; Hill, H. R. *Clin. Diagnostic. Lab. Immunol.* **2002**, *9*, 872-876.

(78) Memish, Z. A.; Almuneef, M.; Mah, M. W.; Qassem, L. A.; Osoba, A. O. *Diagnostic Microbiology and Infectious Disease* **2002**, *44*, 129-132.

(79) Shetty, S.; Ghosh, K.; Mohanty, D. *Acta Haematologica* **2002**, *109*, 18-22.

(80) Boehme, M. W. J.; Stremmel, W. *J. Immunol. Methods* **2004**, *286*, 231-240.

(81) Zhao, L.; Lin, J.-M.; Li, Z. *Anal. Chim. Acta* **2005**, *541*, 199-207.

(82) Guglielmo-Viret, V.; Attree, O.; Blanco-Gros, V.; Thullier, P. *J. Immunol. Methods* **2005**, *301*, 164-172.

(83) McKenna, S. L. B.; Keefe, G. P.; Barkema, H. W.; Sockett, D. C. *Vet. Microbiol.* **2005**, *110*, 105-111.

(84) Sletten, G. B.; Lovberg, K. E.; Moen, L. H.; Skarpeid, H. J.; Egaas, E. *Food Agric. Immunol.* **2005**, *16*, 235-243.

(85) Chen, F.-T. A. *J. Chromatogr., A* **1994**, *680*, 419-423.

(86) Diamandis, E. P.; Morton, R. C. In *Can.*; (Nordion International Inc., Can.). Ca, 1994, 60-65.

(87) van Gijlswijk, R. P. M.; Zijlmans, H. J. M. A. A.; Wiegant, J.; Bobrow, M. N.; Erickson, T. J.; Adler, K. E.; Tanke, H. J.; Raap, A. K. *J. Histochem. Cytochem.* **1997**, *45*, 375-382.

(88) Kobayashi, T.; Iijima, S.; Shimada, K. In *Jpn. Kokai Tokkyo Koho*; (Ibiden Co Ltd, Japan). Jp, 1993, p 9 pp.

(89) Allicotti, G.; Borras, E.; Pinilla, C. *J. Immunoassay Immunochem.* **2003**, *24*, 345-358.

(90) Lei, L.-M.; Wu, Y.-S.; Gan, N.-Q.; Song, L.-R. *Clin. Chim. Acta* **2004**, *348*, 177-180.

(91) Michelsen, A. E.; Wergeland, R.; Stokke, O.; Brosstad, F. In *PCT Int. Appl.*; (Medinnova A/S, Norway; Forskningsparken A/S). Wo, 2004, p 34 pp.

(92) Tian, Z.; Guo, Z. *Proc. SPIE-Int. Soc. Opt. Eng.* **2005**, *5638*, 698-704.

(93) Yuan, J.; Wang, G. *J. Fluoresc.* **2005**, *15*, 559-568.

(94) Mullett, W. M.; Lai, E. P. C.; Yeung, J. M. *Methods* **2000**, *22*, 77-91.

(95) Svitel, J.; Dzgoev, A.; Ramanathan, K.; Danielsson, B. *Biosens. Bioelectron.* **2000**, *15*, 411-415.

(96) Kanda, V.; Kariuki, J. K.; Harrison, D. J.; McDermott, M. T. *Anal. Chem.* **2004**, *76*, 7257-7262.

(97) Nakagawa, H.; Saito, I.; Chinzei, T.; Nakaoki, Y.; Iwata, Y. *Sens. Actuators, B* **2005**, *B108*, 772-777.

(98) Yang, C.-Y.; Brooks, E.; Li, Y.; Denny, P.; Ho, C.-M.; Qi, F.; Shi, W.; Wolinsky, L.; Wu, B.; Wong, D. T. W.; Montemagno, C. D. *Lab on a Chip* **2005**, *5*, 1017-1023.

(99) Tian, Y.; Chen, Y.; Song, D.; Liu, X.; Bi, S.; Zhou, X.; Cao, Y.; Zhang, H. *Anal. Chim. Acta* **2005**, *551*, 98-104.

(100) Daniels, P. B.; Deacon, J. K.; Eddowes, M. J.; Pedley, D. G. *Sens. Actuators* **1988**, *15*, 11-18.

(101) VanderNoot, V. A.; Lai, E. P. C. *Spectroscopy* **1991**, *6*, 28-33.

(102) Morgan, C. L.; Newman, D. J.; Cohen, S. B. A.; Lowe, P.; Price, C. P. *Biosens. Bioelectron.* **1998**, *13*, 1099-1105.

(103) Anderson, G. P.; Merrick, E. C.; Trammell, S. A.; Chinowsky, T. M.; Shenoy, D. K. *Sens. Lett.* **2005**, *3*, 151-156.

(104) Fleischmann, M.; Hendra, P. J.; McQuillan, A. J. *Chem. Phys. Lett.* **1974**, *26*, 163-166.

(105) Jeanmaire, D. L.; Van Duyne, R. P. *J. Electroanal. Chem. Interfacial Electrochem.* **1977**, *84*, 1-20.

(106) Albrecht, M. G.; Creighton, J. A. *J. Am. Chem. Soc.* **1977**, *99*, 5215-5217.

(107) Wang, D. S.; Chew, H.; Kerker, M. *Apple. Opt.* **1980**, *19*, 2256-2257.

(108) Kerker, M.; Wang, D.-S.; Chew, H. *Apple. Opt.* **1980**, *19*, 4159-4174.

(109) Kerker, M.; Siiman, O.; Bumm, L. A.; Wang, D. S. *Apple. Opt.* **1980**, *19*, 3253-3255.

(110) Zeman, E. J.; Schatz, G. C. *J. Phys. Chem.* **1987**, *91*, 634-643.

(111) Aravind, P. K.; Nitzan, A.; Metiu, H. *Surf. Sci.* **1981**, *110*, 189-204.

(112) Inoue, M.; Ohtaka, K. *Phys. Rev. B* **1982**, *26*, 3487-3490.

(113) Lazarides, A. A.; Schatz, G. C. *J. Chem. Phys.* **2000**, *112*, 2987-2993.

(114) Lazarides, A. A.; Schatz, G. C. *J. Phys. Chem. B* **2000**, *104*, 460-467.

(115) Wood, E.; Sutton, C.; Beezer, A. E.; Creighton, J. A.; Davis, A. F.; Mitchell, J. C. *Int. J. Pharm.* **1997**, *154*, 115-118.

(116) Picorel, R.; Chumanov, G.; Torrado, E.; Cotton, T. M.; Seibert, M. *J. Phys. Chem. B* **1998**, *102*, 2609-2613.

(117) Murgida, D. H.; Hildebrandt, P. *J. Am. Chem. Soc.* **2001**, *123*, 4062-4068.

(118) Rohr, T. E.; Cotton, T.; Fan, N.; Tarcha, P. J. *Anal. Biochem.* **1989**, *182*, 388-398.

(119) Ni, J.; Lipert, R. J.; Dawson, G. B.; Porter, M. D. *Anal. Chem.* **1999**, *71*, 4903-4908.

(120) Grubisha, D. S.; Lipert, R. J.; Park, H.-Y.; Driskell, J.; Porter, M. D. *Anal. Chem.* **2003**, *75*, 5936-5943.

(121) Driskell, J. D.; Kwarta, K. M.; Lipert, R. J.; Porter, M. D.; Neill, J. D.; Ridpath, J. F. *Anal. Chem.* **2005**, *77*, 6147-6154.

(122) Dou, X.; Takama, T.; Yamaguchi, Y.; Yamamoto, H.; Ozaki, Y. *Anal. Chem.* **1997**, *69*, 1492-1495.

(123) Hawi, S. R.; Rochanakij, S.; Adar, F.; Campbell, W. B.; Nithipatikom, K. *Anal. Biochem.* **1998**, *259*, 212-217.

(124) Grabar, K. C.; Freeman, R. G.; Hommer, M. B.; Natan, M. J. *Anal. Chem.* **1995**, *67*, 735-743.

(125) Chan, H. Y. H.; Takoudis, C. G.; Weaver, M. J. *J. Catal.* **1997**, *172*, 336-345.

CHAPTER 2. SINGLE PARTICLE RAMAN MEASUREMENTS OF GOLD NANOPARTICLES USED IN SURFACE-ENHANCED RAMAN SCATTERING (SERS)-BASED SANDWICH IMMUNOASSAYS

A paper published in *Proceedings of SPIE-Nanosensing: Materials and Devices*[1]

Hye-Young Park,[2] Robert J. Lipert,[2,3] and Marc D. Porter[2,3]

Abstract

The effect of particle size on the intensity of surface-enhanced Raman scattering (SERS) using labeled gold nanoparticles has been investigated. Two sets of experiments were performed, both of which employed 632.8-nm laser excitation. The first entailed a sandwich immunoassay in which an antibody coupled to a smooth gold substrate selectively captured free-prostate specific antigen (f-PSA) from buffered aqueous solutions. The presence of captured f-PSA was then detected by the response of Raman-labeled immunogold nanoparticles with nominal diameters of 30, 40, 50, 60, or 80 nm. The resulting SERS responses were correlated to particle densities, which were determined by atomic force microscopy, by calculating the average response per particle after accounting for differences in particle surface area. This analysis showed that the magnitude of the SERS response increased with increasing particle size. The second set of experiments examined the response of individual nanoparticles. These experiments differed in that the labeled nanoparticles were

---

[1] Reprinted with permission from Proceedings of *SPIE-Nanosensing: Materials and Devices*, **2004,** 5593, 464-477

[2] Ames Laboratory – U.S. DOE and Department of Chemistry, Iowa State University, Ames, Iowa 50011

[3] Corresponding authors: blipert@porter1.ameslab.gov; phone 515-294-8837; fax 515-294-3254, mporter@porter1.ameslab.gov; phone 515-294-6433

coupled to the smooth gold substrate by an amine-terminated thiolate, yielding a much smaller average separation between the particles and substrate. The results revealed that particles with a diameter of ~70 nm exhibited the largest enhancement. The origin of the difference in the two sets of findings, which is attributed to the distance dependence of the plasmon coupling between the nanoparticles and underlying substrate, is briefly discussed.

Keywords: surface-enhanced Raman scattering (SERS), gold, nanoparticles, size, atomic force microscopy (AFM), self-assembled monolayer

Introduction

Our laboratory recently reported on the use of surface-enhanced Raman scattering (SERS) in sandwich-based immunoassays employing labeled gold nanoparticles.[1,2] Paralleling recent developments in the application of SERS in biodiagnostics,[3-8] femtomolar detection of free-prostate specific antigen (f-PSA) in spiked human serum samples was achieved by modifying 30-nm gold nanoparticles with extrinsic Raman labels (ERLs) and anti-f-PSA antibodies. The ERLs were formed by employing dithiobis succinimidyl nitrobenzoate (DSNB) as a bifunctional ligand to covalently couple anti-f-PSA antibodies to the gold particle surface and to provide a distinctive Raman spectrum for detection of the binding of f-PSA to a capture smooth gold films modified with anti-f-PSA. Gold nanoparticles were chosen as the enhancing substrate to facilitate excitation with 632.8-nm laser light, thereby minimizing the fluorescent background that can arise from shorter wavelength excitation of biological media.

The SERS effect for noble metal particles having a sub-wavelength size (i.e., nanoparticles) originates to a large extent from an amplification of the electromagnetic field

upon irradiation due to excitation of the plasmon resonance. Interestingly, the plasmon resonance is strongly particle size and shape dependent, which in turn results in characteristic UV-vis absorption spectra. Current theory predicts that SERS enhancements increase with increasing particle size as a result of the electric field enhancement.[9] However, recent experimental studies at the individual particle level show a strong discrepancy with respect to theoretical expectations. Emory et al. studied the size and shape dependence of enhancement by identifying SERS active silver nanoparticles by the filtration of heterogeneous mixtures of silver colloids. The results showed that the most active particles were collected in the 80-100 nm fraction.[10] Krug et al. found that gold nanoparticles with a 63 (± 3) nm diameter have an unexpectedly large enhancement at an excitation wavelength of 647 nm. In both cases, the discrepancy between theory and experiments was attributed to the presence of facets on the particle surface, which may act as locations of sharp surface asperity with unusually large electric field enhancements and/or as sites active for charge-transfer based enhancements.[11] In adopting a different tactic, Freeman et al. examined the effect of the size of gold nanoparticle aggregates on SERS intensities. The results showed that aggregate sizes less than 200 nm gave highest SERS intensities. These experiments also revealed that the size of the particles that form the aggregates played a key role in the magnitude of enhancement.[12]

These reports indicate the need for an assessment of the effect of particle size and aggregation on the response observed in our SERS-based immunoassays, noting that changes in particle size can have several differing effects on the assay. Size alters the frequency of the plasmon resonance, which has an impact on the optimal excitation wavelength. Size also changes the number of DSNB labels coated on an individual particle. Moreover, size has a

direct impact on the time required for the labeled particles to bind to the captured antibody and on the stability of the colloidal solution with respect to particle precipitation. As a consequence, assay optimization reflects a compromise between maximization of SERS enhancement, the number of labels bound to a particle, and particle stability, and minimization of incubation time.

In this paper, the effect of using different sizes of gold nanoparticles in our ERL-based detection scheme is investigated. Our previous study reported a notable variability in signal across the sandwich assay surface, which was attributed to particle aggregation and/or to a few particles exhibiting anomalously large enhancements.[13,14] While these "hot spots" were omitted from our analysis of the assay results, an understanding of their origin is of both fundamental and technological importance. The experiments described herein were therefore designed to examine enhancements in the absence of particle aggregation as well as to begin an assessment of contributions from plasmon resonance coupling between the particles and underlying gold substrates. Two sets of experiments were performed, both of which employed 632.8-nm laser excitation. The first set of experiments involved the aforementioned sandwich immunoassay in which (1) immobilized anti-PSA selectively bound f-PSA from buffered aqueous solutions, and (2) captured f-PSA was detected by the response of Raman-labeled immunogold nanoparticles with nominal diameters of 30, 40, 50, 60, and 80 nm. The second set of experiments examined the response of individual nanoparticles. These experiments, however, differed in that the labeled nanoparticles were coupled to the underlying smooth gold substrate by an amine-terminated thiolate, yielding a much smaller separation between particle and substrate. The findings of these experiments are discussed, with the differences in the two sets of results in light of theoretical

considerations of the distance dependence of the plasmon coupling between the nanoparticle and underlying substrate.

Experimental Section

Reagents. Gold nanoparticles with differing diameters (30, 40, 50, 60, and 80 nm) and respective concentrations (2.0×10^{11}, 9.0×10^{10}, 4.5×10^{10}, 2.6×10^{10}, and 1.1×10^{10} particles/mL) were purchased from Ted Pella. The cited particle sizes and concentrations are vendor specifications. Capture anti-human f-PSA, f-PSA and detection anti-human PSA were purchased from BiosPacific. Tween 80, bovine serum albumin (BSA), aminoethanethiol (AET), and octadecanethiol (ODT) were purchased from Sigma-Aldrich. Dithiobis (succinimidyl undecanoate) (DSU) and dithiobis (succinimidyl nitrobenzoate) (DSNB) were synthesized according to a slight modification[2] of a literature procedure.[15,16] Photoresists 1813, lift-off resist, and AZ developer were purchased from Shipley. Deionized water (18 MΩ), purified with a Millipore system, was used in the preparation of all aqueous solutions.

Substrate preparation. For the f-PSA assay study, a smooth gold film was used as the capture substrate. These substrates were prepared by the deposition of 300 nm of gold onto cleaned glass slides (size of 0.8 x 1.5 cm) that were previously coated with a 15-nm chromium adhesion layer. The assay area was defined by using a poly(dimethylsiloxane) stamp coated with ODT.[17]

For the single nanoparticle SERS measurements, patterned gold films on a silicon wafer were prepared to create addresses that facilitated the identification of individual particles. These substrates were prepared by first sonicating a silicon(111) wafer in hexane,

acetone, and methanol (30 min in each), which were then dried under a stream of purified nitrogen gas. Patterns were then prepared via lift-off methodology. First, the silicon surfaces were dehydrated on a hot plate at 200 °C for 5 min and then coated with lift-off resist by spin-coating at 4,000 rpm for 30 s. Next, the coated substrate was prebaked at 160 °C for 30 min, coated with photoresist 1813 at 4,000 rpm for 30 s, and soft baked at 115 °C for 5 min. These samples were patterned by using a transmission electron microscopy grid (800-mesh with 22.5 μm-hole width and 11 μm-bar width) as a photomask. The photomask was placed on the substrate and exposed to UV light (275 W Hg lamp) at 365 nm for 15 s. The exposed resin was then removed by using AZ photoresist developer. This process leaves grid-like patterns of photoresist with ~20 by 20 μm "addresses" of exposed silicon that are separated by ~10 μm-wide lines of photoresist. These samples were next coated with a 15-nm chromium adhesion layer, followed by a 300-nm gold film. The remaining photoresist was removed by sonication in acetone. This process yields an array of square-shaped gold addresses on the silicon wafer. The patterned substrate was then cleaned in methanol, dried with nitrogen gas, and immersed in 1 mM of AET in ethanol for 24 h. The substrates were thoroughly rinsed with ethanol and dried under a stream of nitrogen gas. These substrates were then immersed for ~12 h directly into a solution of DSNB-labeled gold nanoparticles, prepared as described below.

Preparation of capture surface and Raman-labeled immunogold particles.

Capture anti-f-PSA was immobilized on gold-coated glass substrates via the linker molecule DSU. A monolayer of the corresponding thiolate of this linker was prepared by immersing the gold substrates in a 1 mM ethanolic solution of DSU for 24 h and then rinsing with ethanol and drying under a stream of high purity nitrogen gas. For antibody

immobilization, 35 μL of 100 μg/mL of anti-PSA in 50 mM borate buffer (pH 9.0) was pipetted on the DSU-based monolayer and allowed to react for 12 h. The succinimidyl group, positioned at the terminus of the monolayer formed from DSU, reacts with amine groups of anti-f-PSA to form an amide linkage, which covalently tethers anti-f-PSA to the organic adlayer.[15,18,19] After incubation, the substrates were rinsed in 25 mM borate buffer with 1% Tween 80.

To prepare labeled immunogold, as-received gold nanoparticles were centrifuged and resuspended in 2 mM borate buffer (pH 9.0) that contained 1% Tween 80. The particles were then coated with a Raman scatterer by adding 100 μL of 1 mM DSNB in acetonitrile to 1 mL of the particle solution, which was reacted at room temperature for ~12 h. The mixture was centrifuged at 2,000 g and resuspended in 2 mM borate buffer three times to remove unreacted DSNB. The next step added 23 μg of detection anti-PSA to the reaction vessel, with the mixture incubated overnight. After three repetitive cycles of centrifugation at 2,000 g and resuspension, the particles were resuspended in 2 mM tris buffer (pH 7.4) that contained 1% BSA. We note that the particles used in the characterization of isolated nanoparticles (i.e., those coupled to the AET-modified gold films) were only coated with DSNB.

Assay protocol. The sandwich immunoassay for f-PSA was performed as previously described.[1,2] Briefly, after blocking with 1% BSA in 50 mM borate buffer, the capture surfaces were exposed to phosphate buffer solutions (pH 7.5) containing various concentrations of f-PSA (1, 10, 100 ng/mL). Bound f-PSA was then detected by exposing the sample to the immunogold reagent for 12 h. After rinsing the substrates to remove excess particles, the samples were characterized by SERS and atomic force microscopy (AFM).

Nanoparticles larger than 80 nm were not characterized because sedimentation occurred on a time scale shorter than the incubation times employed.

SERS. Raman spectra for the sandwich immunoassays were collected using a fiber-optic-based Raman system, the NanoRaman I from NanoRaman Instruments.[2] The system is equipped with CCD (Kodak 0401 E) which is thermoelectrically cooled to 0 °C and a Czerny-Turner imaging spectrometer (*f*/2.0). The power incident on the sample from a HeNe laser (632.8 nm) was 30 mW (390 μm^2 spot size).

For the characterization of single nanoparticle responses, a SERS-microscope was assembled by combining an optical microscope (Olympus BH-2) and spectrograph (SpectraPro, 300i, Acton Research Corp.) equipped with Liquid nitrogen cooled-CCD (LN/CCD-1100PB, Princeton Instruments). The CCD and spectrograph were controlled by computer interface (ST-133 controller, Princeton Instruments). The light source was HeNe laser (632.8 nm) with output power of 7.4 mW. The incident power on sample was 0.4 mW. A microscope objective with a 100x magnification and numerical aperture of 0.95 was used to obtain the optical micrographs and to collect the Raman signal from individual particles. This configuration provides a laser beam focused to a 1.2-μm diameter spot on the sample surface.

AFM. All particle images on the PSA assay substrates were obtained in TappingMode™ under ambient conditions using a Multimode NanoScope III AFM from Digital Instruments that was equipped with a 125-μm tube scanner. The tips were silicon TESP probes (Nanosensors) with resonance frequencies between 298 and 365 k Hz. Histograms were generated by exporting the data from the particle size analysis software resident on the AFM. For single nanoparticle studies, a Dimension 3000 AFM from Digital

Instruments equipped with an optical microscope was used to locate, focus, and image the surface regions of interest.

Results and Discussion

Characterization of the size-dependent response for gold nanoparticles in a sandwich immunoadsorbent assay. SERS spectra and AFM images were collected on five different locations on each sample as a function of particle size (30, 40, 50, 60, and 80 nm) and f-PSA concentration (100, 10, and 1 ng/mL). Figs. 1A , B show representative SERS spectra that were obtained from these samples with the 60-nm and 40-nm Raman-labeled immunogold particles, respectively. Three important inferences can be drawn from these data. First, bands diagnostic of the DSNB-labeled particles (e.g., the symmetric nitro stretch at 1335 cm^{-1} and an aromatic ring stretching mode at 1566 cm^{-1})[20] are present in both sets of data. Second, the changes in the magnitude of the bands track with the differences in f-PSA levels. Third, the responses of the assays that used the 60-nm gold particles are much greater than those for the corresponding assays carried out with the 40-nm gold particles. These results are consistent with the design of our sandwich-based assay. Moreover, the differences in the magnitude of the responses for the 60- and 40-nm gold particles are qualitatively consistent with the dependence of position of the plasmon resonance on particle size.[21]

Correlations of the response magnitude and particle size also entailed sample characterization with AFM. Fig. 2 presents a portion of these findings by showing a set of AFM images (19.7 x 19.7 μm) for the samples used in the assays with the 60-nm (Figs. 2A-C) and 40-nm (Figs. 2D-F) gold particles. The AFM image area was set to approximately the size as the focused laser spot, but do not represent the same areas in which SERS

measurements were made. The results show that (1) the number of particles presented in the image increases, as expected, with the increase in f-PSA concentration; (2) the sizes of the particles are close to those specified by the vendor; and (3) the majority of the particles are not aggregated. With respect to the latter, only 2-5 particle clusters were observed for every 100 particles, with clusters generally composed of less than five particles. We did not find evidence for a correlation between aggregation and particle size. Moreover, these images indicate that the spectra in Fig. 1 and for all other samples reflect enhancements primarily from isolated particles and not aggregates.

Fig. 3 shows a series of representative histograms generated from AFM images of the f-PSA capture surfaces following assays for 100 ng/mL f-PSA using different sized gold particles. Particle counts were collected from five different locations on each sample and averaged. The number of particles for each AFM image was obtained using particle analysis software provided with the AFM by setting the counting threshold just above that of the roughness of the underlying film. For 30-nm particles, there was no clear gap between the background and particle height distribution. Particle analysis for the 30-nm particles was performed based on the assumption that the peak profile is symmetric.

Table 1 shows the particle analysis results. In general, the AFM-determined particle sizes were close to those specified by the vendor. The largest relative differences occurred with the 40 and 50-nm particles, which were both more than 10% smaller than as specified. We used the AFM-determined sizes in the calculations of the size and surface area dependence of the SERS signal.

Table 2 summarizes the SERS and AFM data. It lists the SERS intensity in counts/s for the symmetric nitro stretch of DSNB, the number of particles from the AFM images, and

the SERS intensity in counts/particle/s. To account for the fact that the number of labels per particle is dependent on the particle size, Table 2 also provides the response after accounting for particle surface area. The surface area of the particles is based on the average particle size, assuming all particles were spherically shaped. The data in Table 2 show the following trends. First, as the particle size increases, the SERS intensity tends to increase for all f-PSA concentrations. The particle counting results also show that the increase in SERS intensity is not solely due to an increase in the number of captured particles. By normalizing the SERS intensity to the number of particles in each assay, it is seen that the SERS intensity per particle also increases as the particle size increases. Furthermore, by normalizing the data to particle surface area, which accounts for differences in the total number of scatterers, the signal is still observed to increase with increasing particle size; this trend suggests that the SERS enhancement factor also increases with particle size. These results appear to contradict earlier studies that found a maximum in the enhancement factor for particles smaller than 80 nm.[10, 11] These studies, however, examined the response of nanoparticles deposited on a glass substrate, a support with optical properties markedly different from the smooth gold films employed herein. The single particle SERS measurements described next point to how the plasmon coupling between the nanoparticles and gold capture surface play an important role in determining the optimum particle size for SERS enhancement in our experiments.

Single gold nanoparticle SERS. The above measurements represent SERS responses averaged over a population of particles with unknown exact sizes and shapes. To more fully examine the influence of particle size on the observed SERS intensity, SERS measurements were made using single particles that were also characterized by AFM. To facilitate the evaluation of individual particles, patterned gold substrates were used to define

addresses that could be readily mapped by AFM. The response of these particles was then measured using an optical microscope to locate an address known to contain only a few single particles. A simplified particle immobilization scheme, as shown in Fig. 4, was used to bind a small number of particles to the gold surface, noting that this mode of immobilization reduces the separation between the particles and underlying smooth gold substrate.

Figs. 5A, B present optical microscopy images of the patterned gold substrate. Fig. 5A shows an image of a small portion of the patterned substrate, and confirms the presence of an array of gold addresses of the expected size, shape, and separation. Fig. 5B is a magnified image of the substrate location outlined by the dashed lines in Fig. 5A. The bright spot in the lower left portion of the partial gold address at the top of the image is the focused laser beam. Figs. 5C-E are examples of the topographic AFM images of the patterned substrate modified with DSNB-labeled gold nanoparticles having a nominal diameter of 80 nm. Fig. 5C is the entire area of a square-shaped address, while Figs. 5D, E represent incremental expansions of the image in Fig. 5C. The bright spots in Figs. 5D, E indicate the location of gold particles. In Fig. 5E, the circled areas designate regions where SERS measurements were made.

As is evident in Fig. 5E, regions 1, 2, and 3 contain single gold nanoparticles, whereas region 4 is an area devoid of particles. Cross-sectional analysis from the AFM topographic images indicates that the particles in regions 1-3 have sizes of 80.2, 67.6, and 56.9 nm but are irregularly (i.e., non-spherical) shaped. SERS spectra were measured using the AFM images as a guide to the location of the nanoparticles in a gold address. The focused laser was positioned in regions 1-4 using large aggregates or other surface features visible by optical microscopy as reference points.

A portion of these results are shown in Fig. 5F-I. Spectral features characteristic of DSNB-coated gold particles are evident in each of the measurements made in regions 1-3. Note that the SERS intensity is observed to decrease with decreasing particle size over this size range. No SERS was observed in region 4, indicating that the Raman spectra originate from the observed particles and not from background contamination.

In addition to mapping out the location of the immobilized particles, the AFM images were analyzed to correlate particle size and SERS intensity. Fig. 6 summarizes the first results of these experiments by plotting the SERS intensities, normalized to the particle surface area, for several different sized gold particles. These preliminary results show that the area-normalized response undergoes a gradual increase as the size of the particles decreases, reaching a maximum at ~70 nm. While requiring a larger data set, the findings also suggest that the area normalized response begins to decrease as the particle size moves below ~70 nm. Interestingly, the results in Fig. 6 differ from those found for the experiments based on the immunoadsorbent assay. With the immunoadsorbent assay, the area-normalized response had yet to reach a limiting value for particles with a nominal size of 80 nm, suggesting that larger particles may result in larger enhancements. Qualitatively, the differences in the particle size responses are consistent with expectations that take into account the coupling between the particle plasmon and the underlying smooth gold substrate.[22] That is, the extent of plasmon coupling is dependent on the ratio of the particle diameter (d) to the separation (a) between the particle and substrate. As a consequence, the maximum coupling, as revealed by the location of the extinction maximum, will occur at smaller values of a as d decreases. Our results are in general agreement with this expectation, confirming the importance of substrate coupling on the observed response.

The role of coupling in our two sets of results is further evident from the results of experiments in which we attempted to detect the presence of labeled gold particles effectively dispersed in aqueous solution. These experiments used particle concentrations such that the number of particles in the focused laser beam was much greater than those in the experiments using immobilized particles. We have, to date, not detected a response from the particles in any of these experiments. In contrast, we are able to readily measure SERS from single particle in close proximity to a gold surface, suggesting that the coupling between the particle and surface has shifted the plasmon resonance to a wavelength more favorable for excitation with 632.8-nm light.

Conclusions

This paper has investigated the dependence of SERS enhancements on the size of DSNB-coated gold nanoparticles in two different formats, each of which yielded differences in the average separation between the immobilized nanoparticles and underlying smooth gold substrate. The observed enhancements, which reflected the response of non-aggregated particles, qualitatively followed expectations based on the distance dependence of the plasmon coupling between the nanoparticle and underlying substrate. That is, enhancements in the assay experiments increased with increasing particle size for the range of particle sizes tested (30-80 nm), whereas the enhancement for the particles immobilized with much smaller average particle-substrate separation maximized at a nominal diameter of ~70 nm. Ongoing research will build on these findings in an effort to more fully understand the contribution of plasmon coupling and how to fully exploit this phenomenon for further lowering the limit of

detection in SERS-based immunoassays and other areas in biodiagnoistics and homeland security.

Acknowledgments

This work was supported by Concurrent Analytical, Inc. through a grant from the DARPA CEROS program and by the Institute for Combinatorial Discovery of Iowa Sate University. The Ames Laboratory is operated for the U./S. Department of Energy by Iowa State University under contract W-7405-eng-82.

References

(1) Ni, J.; Lipert, R. J.; Dawson, G. B.; Porter, M. D. *Anal. Chem.* **1999**, *71*, 4903.

(2) Grubisha, D. S.; Lipert, R. J.; Park, H.-Y.; Driskell, J.; Porter, M. D. *Anal. Chem.* **2003**, *75*, 5936.

(3) Freeman, R. G.; Grabar, K. C.; Allison, K. J.; Bright, R. M.; Davis, J. A.; Guthrie, A. P.; Hommer, M. B.; Jackson, M. A.; Smith, P. C.; et al. *Science (Washington, D.C.)* **1995**, *267*, 1629.

(4) Keating, C. D.; Kovaleski, K. M.; Natan, M. J. *J. Phys. Chem. B* **1998**, *102*, 9404.

(5) Graham, D.; Mallinder, B. J.; Smith, W. E. *Biopolymers* **2000**, *57*, 85.

(6) Graham, D.; Mallinder, B. J.; Whitcombe, D.; Smith, W. E. *ChemPhysChem* **2001**, *2*, 746.

(7) Graham, D.; Mallinder, B. J.; Smith, W. E. *Angew. Chem., Int. Ed.* **2000**, *39*, 1061.

(8) Cao, Y. C.; Jin, R.; Mirkin, C. A. *Science (Washington, D.C.)* **2002**, *297*, 1536.

(9) Zeman, E. J.; Schatz, G. C. *J. Phys. Chem.* **1987**, *91*, 634.

(10) Emory, S. R.; Nie, S. *Anal. Chem.* **1997**, *69*, 2631.

(11) Krug, J. T., II; Wang, G. D.; Emory, S. R.; Nie, S. *J. Am. Chem. Soc.* **1999**, *121*, 9208.

(12) Freeman, R. G.; Bright, R. M.; Hommer, M. B.; Natan, M. J. *J. Raman Spectrosc.* **1999**, *30*, 733.

(13) Nie, S.; Emory, S. R. *Science (Washington, D.C.)* **1997**, *275*, 1102.

(14) Kneipp, K.; Wang, Y.; Kneipp, H.; Perelman, L. T.; Itzkan, I.; Dasari, R. R.; Feld, M. S. *Phys. Rev. Lett.* **1997**, *78*, 1667.

(15) Wagner, P.; Hegner, M.; Kernen, P.; Zaugg, F.; Semenza, G. *Biophys. J.* **1996**, *70*, 2052.

(16) Niemz, A.; Jeoung, E.; Boal, A. K.; Deans, R.; Rotello, V. M. *Langmuir* **2000**, *16*, 1460.

(17) Chen, C. S.; Mrksich, M.; Huang, S.; Whitesides, G. M.; Ingber, D. E. *Biotechnol. Prog.* **1998**, *14*, 356.

(18) Jones, V. W.; Kenseth, J. R.; Porter, M. D.; Mosher, C. L.; Henderson, E. *Anal. Chem.* **1998**, *70*, 1233.

(19) Duhachek, S. D.; Kenseth, J. R.; Casale, G. P.; Small, G. J.; Porter, M. D.; Jankowiak, R. *Anal. Chem.* **2000**, *72*, 3709.

(20) Varsany, G. *Assignments for Vibrational Spectra of Seven Hundred Benzene Derivatives*, 1974.

(21) Bohren, C. F.; Huffman, D. R. *Absorption and Scattering of Light by Small Particles*; John Wiley & Sons: New York, 1983.

(22) Okamoto, T.; Yamaguchi, I. *J. Phys. Chem. B* **2003**, *107*, 10321.

Table 1. Results from gold nanoparticle size analyses from histograms in Figure 1.

Nominal particle size (nm)	AFM mean diameter (nm)	Standard deviation of AFM mean diameter (nm)
30	28.9	5.1
40	34.0	5.7
50	45.9	6.4
60	60.3	8.5
80	78.2	8.5

Table 2. Summary of SERS and AFM characterizations for the f-PSA immunoadsorbent assay.

f-PSA concentration : 100 ng/mL

	SERS intensity[a, b] (counts/s)	Number of particles	Counts/particle/s	Counts/s/ nm^2 (x 10^5)
30 nm	15 (±3.5)	402 (±16)	0.04	1.52
40 nm	130 (±18)	633 (±16)	0.21	5.78
50 nm	200 (±25)	546 (±19)	0.36	5.43
60 nm	638 (±35)	367 (±84)	1.74	15.2
80 nm	15333 (±307)	2424 (±109)	6.33	32.9

f-PSA concentration : 10 ng/mL

	SERS intensity[a, b] (counts/s)	Number of particles	Counts/particle/s	Counts/s/ nm^2 (x 10^5)
30 nm	1.3 (±0.25)	42 (±7)	0.03	1.14
40 nm	19 (±3)	88 (±3)	0.21	5.78
50 nm	10 (±1)	55 (±7)	0.17	2.56
60 nm	75 (±12)	57 (±10)	1.31	11.6
80 nm	793 (±16)	113 (±18)	7.00	36.4

f-PSA concentration : 1 ng/mL

	SERS intensity[a, b] (counts/s)	Number of particles	Counts/particle/s	Counts/s/ nm^2 (x 10^5)
30 nm	2 (±1)	34 (±6)	0.05	1.90
40 nm	5 (±1)	29 (±2)	0.17	4.68
50 nm	2 (±1)	13 (±2)	0.14	2.11
60 nm	13 (±4)	19 (±3)	0.70	6.13
80 nm	129 (±15)	25 (±4)	5.16	26.9

a) Intensity of symmetric nitro stretch (1335 cm^{-1}).
b) Uncertainty is within 25% of the reported value.

Figure Captions

Figure 1. SERS spectra collected from the f-PSA sandwich immunoassay samples with 60-nm (A) and 40-nm (B) DSNB-labeled gold particles.

Figure 2. Topographic AFM images of two sets of samples in the SERS-based detection of f-PSA. Images A-C employed 60-nm ERL particles and images D-F used 40-nm ERL particles; each set was obtained at respective f-PSA concentrations of 100, 10, and 1 ng/mL.

Figure 3. Histograms from the AFM particle size distribution analyses for sandwich assay using 100 ng/mL of f-PSA: 80-nm (A); 60-nm (B) ; 50-nm (C); 40-nm (D); and 30-nm (E).

Figure 4. Schematic of DSNB-coated gold nanoparticles immobilized on an AET monolayer on gold.

Figure 5 (A) Microscopic image of patterned Au on Si –10 x objective (Width of each pattern is ~20 μm). (B) Laser focused on particle a – 100 x objective. (C- E) Topographic AFM image of DSNB-coated Au nanoparticles immobilized on AET SAM on gold. (F- H) Single-particle Raman spectra of particle 1, 2, and 3 respectively. (I) blank spectrum (from spot 4). Peak labeled with * due to room lights.

Figure 6. Area normalized single particle-SERS intensity as a function of the gold nanoparticle diameter.

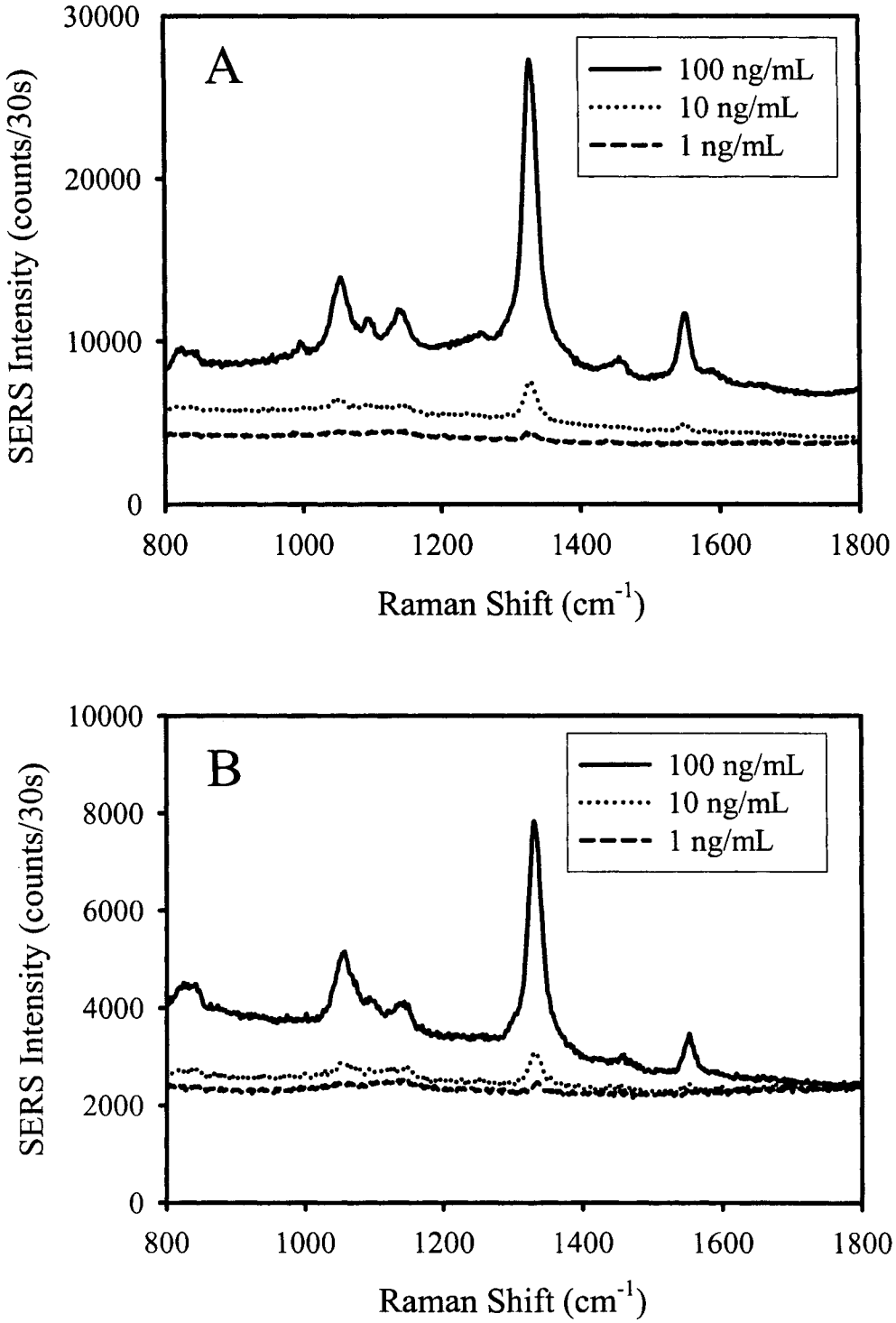
A
100 ng/mL
10 ng/mL
1 ng/mL
SERS Intensity (counts/30s)
30000
20000
10000
0
800
1000
1200
1400
1600
1800
Raman Shift (cm-1)
B
100 ng/mL
10 ng/mL
1 ng/mL
SERS Intensity (counts/30s)
10000
8000
6000
4000
2000
0
800
1000
1200
1400
1600
1800
Raman Shift (cm-1)

Figure 1.

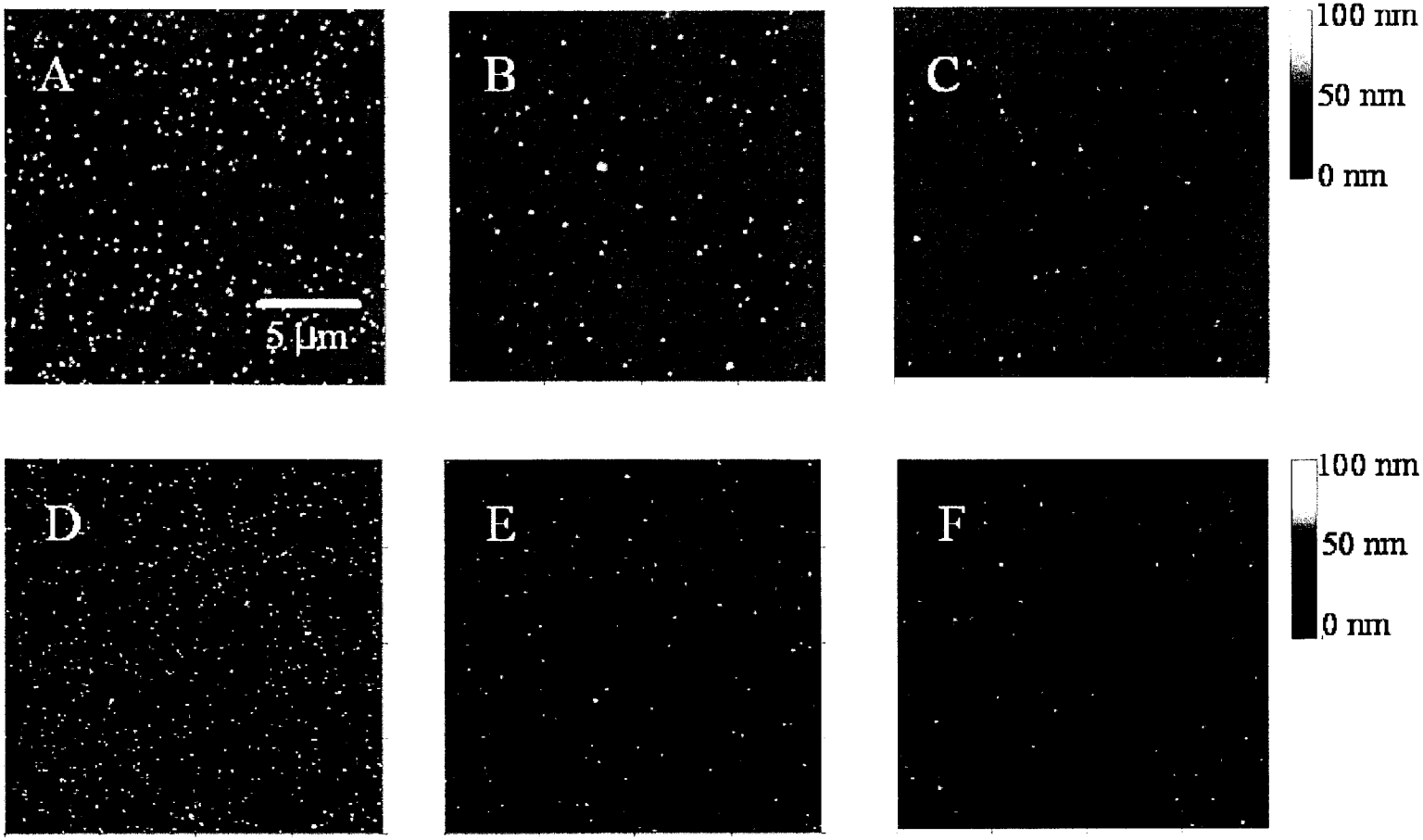

Figure 2.

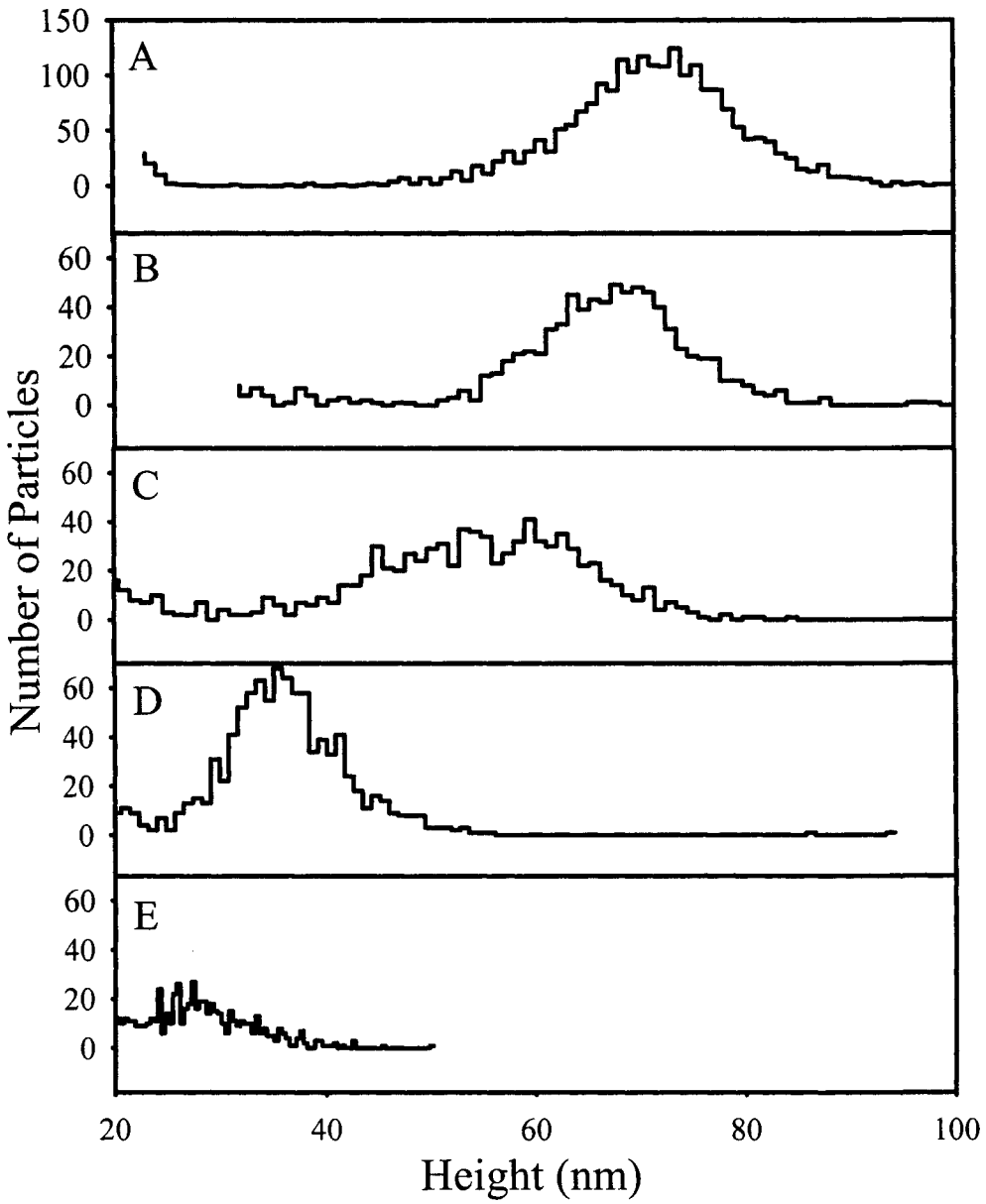
A
B
C
D
E
150
100
50
0
60
40
20
0
Number of Particles
20
40
60
80
100
Height (nm)

Figure 3.

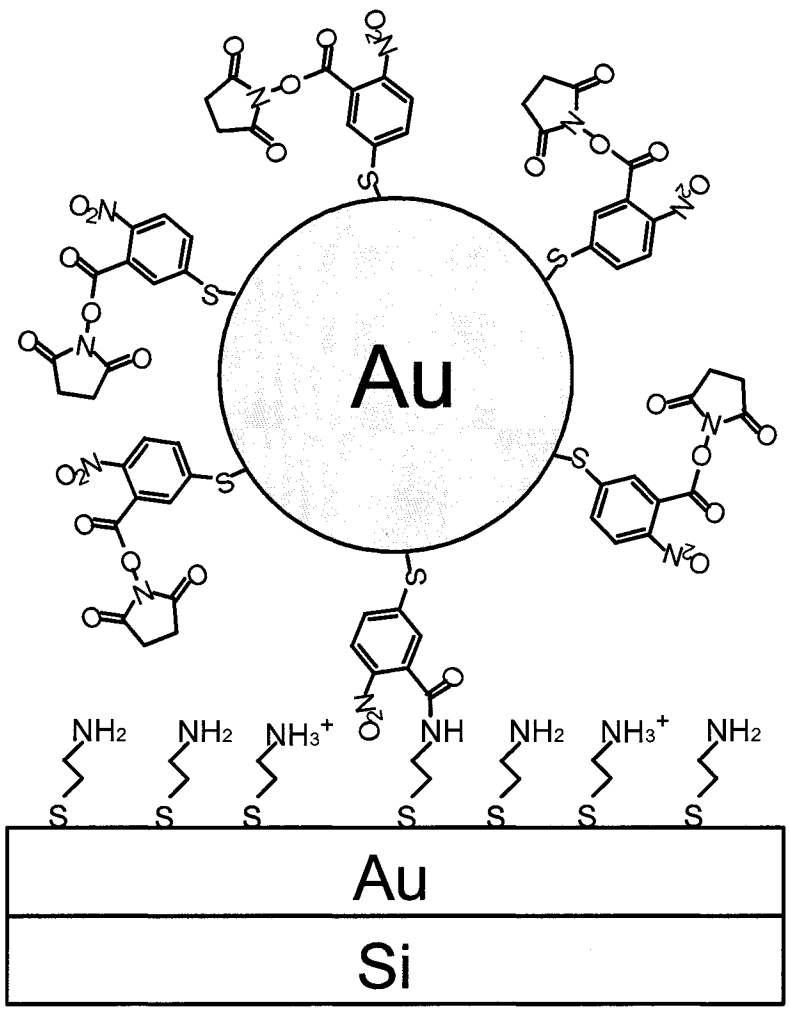

Figure 4.

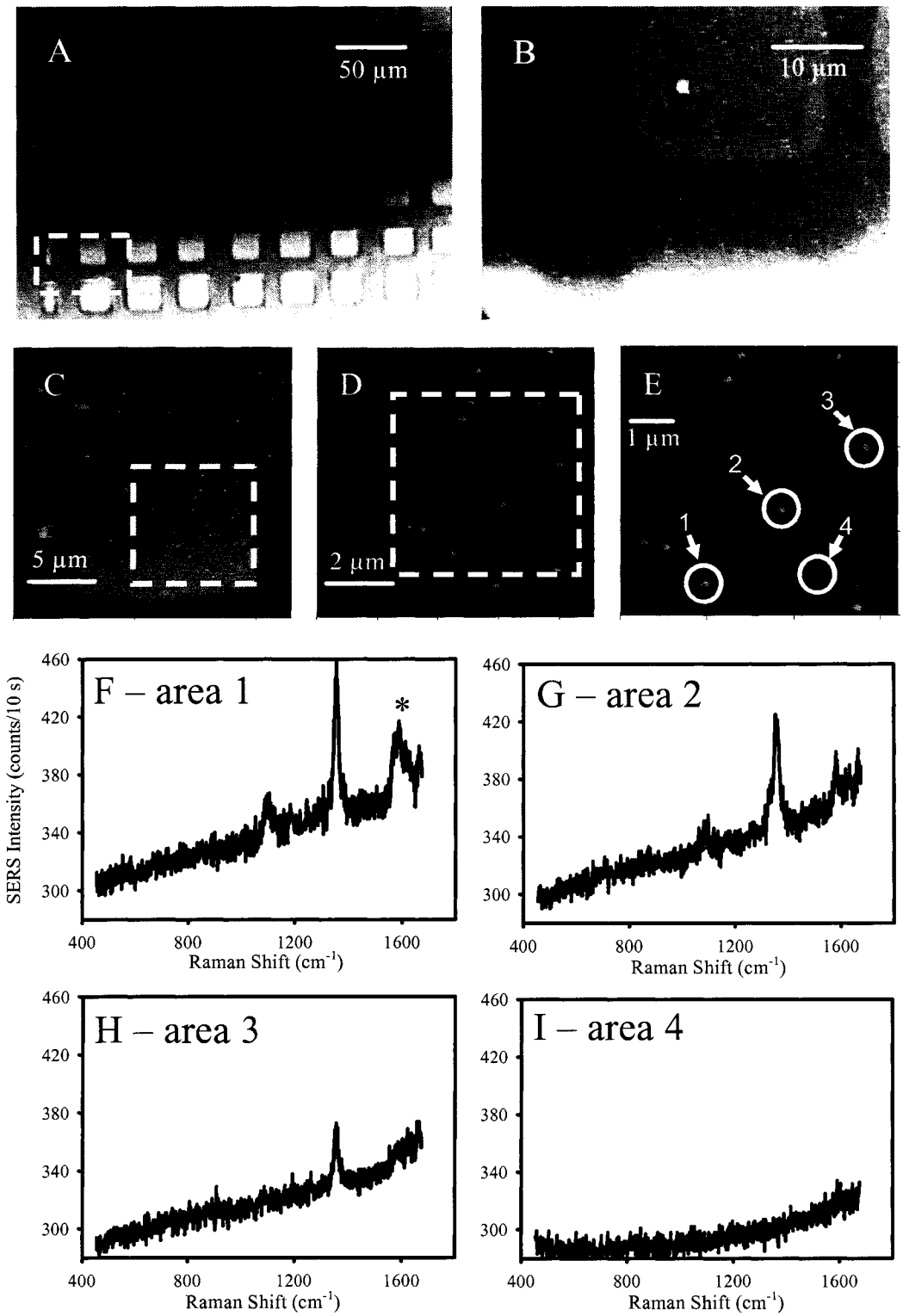
A
50 µm
B
10 µm
C
5 µm
D
2 µm
E
1 µm
1
2
3
4
F – area 1
G – area 2
H – area 3
I – area 4
SERS Intensity (counts/10 s)
Raman Shift (cm-1)
460
420
380
340
300
400
800
1200
1600

Figure 5.

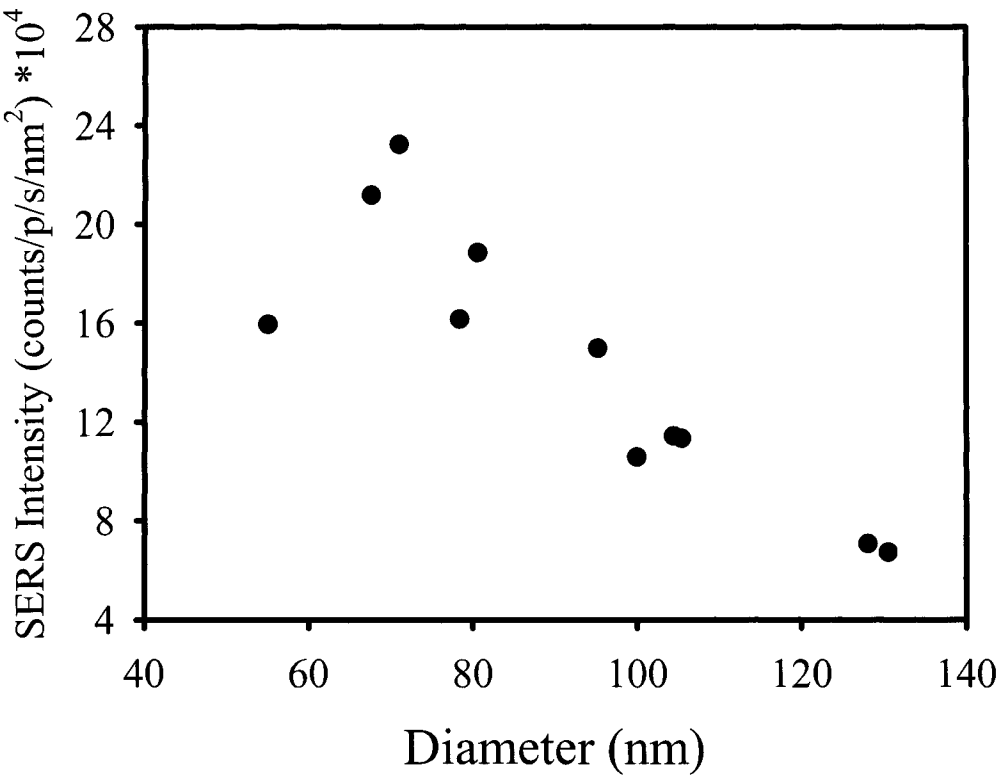
SERS Intensity (counts/p/s/nm^2) *10^4
28
24
20
16
12
8
4
40
60
80
100
120
140
Diameter (nm)

Figure 6.

CHAPTER 3. SURFACE-ENHANCED RAMAN SCATTERING BASED IMMUNOASSAY FOR DETECTION OF *ESCHERICHIA COLI* O157: H7 AND SIMULANTS OF BIOLOGICAL WARFARE AGENTS.

A manuscript in preparation for submission to *Applied Spectroscopy*

Hye-Young Park,[1] Robert J. Lipert,[1,3] Chris Schoen,[2] and Marc D. Porter[1,3]

Abstract

Low-level detection of *Erwinia herbicola* and *bacillus globigii,* simulants for biological warfare agents, and the pathogen *Escherichia coli* O157:H7 is demonstrated utilizing a surface-enhanced Raman scattering (SERS) detection scheme based on a sandwich immunoassay format. SERS labels, also called Extrinsic Raman labels (ERLs™), are created by coating 80-nm gold nanoparticles with a bifunctional thiolate monolayer, which exhibits a strong Raman signal while forming covalent binding with detection antibodies. In the assay, limits of detection of each analyte were determined and single cell detection is demonstrated. Also, a new SERS labeling scheme based on a mixed monolayer is introduced and utilized in the assays of IgG molecules and bacteria. The mixed monolayer ERLs™ are created by covering the gold nanoparticles with a mixture of two thiolates. One thiolate covalently binds antibody to the particle and the other thiolate produces a strong Raman signal. The mixed monolayer ERLs™ can be prepared in

---

[1] Ames Laboratory – U.S. DOE and Department of Chemistry, Iowa State University, Ames, Iowa 50011

[2] Concurrent Analytical Inc.

[3] Corresponding Authors (e-mail) blipert@porter1.ameslab.gov; (phone) 515-294-8837; (fax) 515-294-3254, mporter@porter1.ameslab.gov; phone 515-294-6433

relatively simple steps using commercially available materials, i.e., synthesis of a bifunctional reporter is not required, facilitating the generation of ERLs™ with different Raman labels for potential multiplexing applications.

Introduction

The tragic events of September 11, 2001 have placed the development of techniques for the rapid, low-level detection of biological warfare (BW) agents at the highest possible levels of emphasis.[1] Traditional detection methods for this purpose include culture-[2-5], ELISA-[6], and fluorescence-[7,8] based assays. While generally effective, these methods may have a low level of throughput, be difficult to multiplex, or suffer from photobleaching or shelf-life issues. More recently, research to address these needs have realized breakthroughs such as the polymerase chain reaction,[9] surface plasmon resonance,[10] quartz crystal microbalance,[11,12] immunofiltration,[13] immunomagnetic technology,[14] chemiluminescence,[15] and surface-enhanced Raman scattering (SERS).[16] Nevertheless, the demands of homeland security continue to place a premium on portability, ease of use, and cost, all of which drive the research agenda in a large number of analytical research laboratories.

This paper extends the development and application of a chip-scale readout methodology that has the potential to address many of the challenges presented by the detection of BW agents. The method, which is based on a sandwich-styled immunoassay, utilizes the strong SERS signal from aromatic compounds (i.e., reporter molecules) that are immobilized on gold nanoparticles and subsequently coupled to a molecular recognition element (e.g., antibody). The identity of each antigen is therefore determined from the

characteristic SERS spectrum of the nanoparticle-bound reporter species linked to the tracer antibody, whereas the amount of antigen is quantified by the spectral intensity of the reporter species. The advantages of this detection method largely reflect two unique features of our Extrinsic Raman Labels (ERLs™). First, the intensity of the ERL™ responses for immobilized reporters rival that of fluorescence dyes. Second, the widths of Raman spectral bands for nearly all organic compounds are typically 10-100 times narrower than those of fluorescence, a characteristic that minimizes the potential for spectral overlap in the response from the different labels. These attributes point to the potential of this readout/labeling technology to serve as a highly sensitive, high throughput methodology for pathogen detection.

In earlier reports, we discussed the use of ERLs™ in the detection of proteins such as immunoglobulin G (IgG)[17,18] and free-prostate specific antigen (f-PSA).[19] More recently, we detailed the low level detection of viruses (e.g., feline calicivirus) by a comparable pathway.[20] In this paper, as a first step towards an integrated instrumentation setup capable of fast, sensitive detection with high throughput and multiplexing capability, we have extended our SERS-based platform to the low-level detection of pathogenic bacteria and spores, i.e., *Escherichia coli* (*E. coli)* O157:H7 and simulants of BW agents *Bacillus anthracis* (anthrax) and *Yersinia pestis* (plague) in buffer matrix. The simulant for *Bacillus anthracis* is *Bacillus globigii (B. globigii)* and the simulant for *Yersinia pestis* is *Erwinia herbicola (E. herbicola).* [21,22] Importantly, these targets are much larger in size (*E. coli* 1 × 3 μm, *E. herbicola* 0.5-0.7 × 1-2 μm, and, *B. globigii* 1 × 1.2 μm) than the nanometric proteins (IgG; 5-7 nm, f-PSA; 1-2 nm), and viruses (feline calicivirus; 20-30 nm) previously

detected by ERLs™. This study serves as a vehicle for assessing the potential of the concept to address performance needs, (i.e., accuracy, sensitivity, and specificity), in the detection of BW agents, as well as pathogens central to food and water security.

Herein, the detection of simulants of BW agents is demonstrated first using an ERL™ scheme based on bifunctional reporter molecules that also serve to covalently bind antibodies to gold nanoparticles. Then, in a later section, an alternative ERL™ design based on mixed monolayers is introduced to facilitate the creation of ERLs™ with different Raman reporters, which can be used in multiplexing. The mixed monolayer ERL™ has two components on the same nanoparticle, one component with covalent binding capability and the other component produces a strong Raman signal. Using mixed monolayer ERLs™, single analyte assays for IgG and simulants of BW agents is demonstrated. Finally, SERS signal was measured from tagged single *E. coli* O157:H7 cells using a Raman microscope.

Experimental Section

Reagents. Gold nanoparticles (80 nm in diameter, 1.1 x 10^{10} particles/mL) were purchased from Ted Pella. Dithiobis succinimidyl propionate (DSP), polyclonal goat anti-human IgG, anti-mouse IgG, anti-rabbit IgG, human IgG, mouse IgG, and rabbit IgG were obtained from Pierce Biotechnology. Dithiobis (succinimidyl-2-nitrobenzoate) (DSNB) was synthesized according to a procedure[19] slightly modified from that in the earlier literature.[23,24] Heat killed *E. coli* O157:H7 was the generous gift from Dr. Nancy Cornick (Department of Veterinary Medicine, Iowa State University). Polyclonal anti-*E. coli* O157:H7 was obtained from Kirkgaard & Perry Laboratories. Polyclonal anti-*E. herbicola,*

polyclonal anti-*B. globigii*, *E. herbicola,* and *B. globigii* were acquired from Tetracore. Bovine serum albumin (BSA), borate buffer, and phosphate buffered saline (PBS) buffer packages were from Pierce. Two-part epoxy was purchased from Epotek. Octadecanethiol (ODT), 5, 5'-dithiobis(2-nitrobenzoate) (DNBA), thiophenol (TP), mercaptobenzoic acid (MBA), and NaCl were obtained from Sigma Aldrich. All buffers were prepared in deionized water and then passed through a membrane filter with a 0.22-μm mesh size.

Gold substrate preparation. Template-stripped gold (TSG) substrates were prepared for capture substrate fabrication. First, silicon (111) wafers were cleaned in methanol and dried with a stream of high purity nitrogen gas. The cleaned wafers were placed in an evaporator (Edwards) and coated with a 300-nm gold film. Next, glass slides were cut into 8 x 8 mm sections, sonicated in surfactant (Contrad) -containing water, deionized water, and methanol, each for 30 min, and dried under a nitrogen stream. After drying, two-part epoxy was used to attach the glass sections to the surface of the wafer-supported gold film. The resulting sandwiched materials were then baked in an oven at 150 °C for 90 min. Finally, the careful detachment of the glass sections from the wafers exposed the underlying TSG surface.

Capture substrate preparation. An ODT monolayer was stamped on TSG substrates to define the area addressed in the surface modification and assay procedures. In this process, a PDMS stamp (Dow Corning) with a centered, 3-mm hole was immersed in 2 mM ODT for 1 min and dried with nitrogen gas. The dried PDMS stamp was then gently pressed on a TSG substrate for 30 s. This process leaves an uncoated gold area (3-mm diameter) that is surrounded by a hydrophobic ODT monolayer that acts to confine droplets of aqueous fluids. Next, the substrate was immersed in 0.1 mM DSP in ethanol for 24 h,

rinsed with ethanol, and dried with high purity nitrogen gas, creating a 3-mm diameter DSP-coated address.

The capture antibody substrate was prepared by pipetting 30 μL of 100-μg/mL antibody solution in 50 mM borate buffer on the DSP-monolayer coated address. The substrates were then incubated in a humidity chamber for ~12 h. Substrate preparation was completed by the application of BSA (1% w/w) in 50 mM borate buffer (pH 8.3) as a blocking agent. In the blocking step (1 h), the unreacted succinimidyl groups of the DSP derived monolayer couple with BSA molecules.

ERL™ preparation. To 1 mL of gold nanoparticles (80-nm diameter) in 2 mM borate buffer (pH 8.3) was added 10 μL of 1 mM DSNB in acetonitrile. The mixture was then incubated for 8 h. After the particles were centrifuged at 2,000*g* for 10 min and resuspended in 2 mM borate buffer, and the process repeated an additional two times, 23 μg of antibody was added. The mixture was incubated for 8 h, followed by exposure to 100 μL of 10% BSA. Finally, the particles were rinsed three times and resuspended in borate buffer with 50 mM NaCl.

Assay protocol. The capture substrates were incubated with 30 μL of 10 mM PBS buffer solution (pH 7.4) having concentrations of bacteria and spores ranging from 0 to 10^8 cells (or cfu)/mL. Concentrations of IgGs were varied from 0 to 1000 ng/mL. The substrates were incubated for 3 h and rinsed with PBS buffer. Finally, 30 μL of ERL™ was pipetted onto the substrate and incubated 6 h, followed by a rinse with 2 mM borate buffer.

SERS measurement. All Raman spectroscopic measurements were performed using either a Raman spectrophotometer, (NanoRaman I, Concurrent Analytical), or an in-

house constructed Raman spectroscopy microscope. The NanoRaman I instrument is equipped with fiber optic probe, thermoelectrically cooled CCD (Kodak 0401 E), a Czerny-Turner imaging spectrometer (*f*/2.0), and HeNe laser (30 mW, 632.8 nm). A SERS-microscope was used for single bacterium measurements. This setup consists of an optical microscope (Olympus BH-2) and spectrograph (SpectraPro, 300i, Acton Research Corp.). The spectrograph was equipped with a thinned, back-illuminated, liquid nitrogen-cooled CCD (LN/CCD-1100PB, Princeton Instruments). Substrates are mounted on the microscope sample stage and a HeNe laser (632.8 nm) is used for excitation. This configuration provides a laser beam focused to a 2.5-μm diameter spot with an incident power of 0.4 mW after passage through the 50X objective (numerical aperture of 0.80) of the microscope. The same objective collects the scattered light. All spectra were collected with a 1-s integration time.

Results and Discussion

Assays of *E. coli* O157:H7 and simulants of the BW agents. Based on an earlier study,[25] gold nanoparticles with an 80-nm diameter were employed. In that study, the size of the gold nanoparticles was varied, and the average SERS signal as a function of particle size was obtained using 632.8 nm excitation. The number of captured particles and average diameters were determined by atomic force microscopy (AFM). The results showed that the average enhancement per particle increased with particle size, and that ~80 nm represented a compromise between the normalized enhancement and the stability of the particle suspension.

Figure 1 shows representative spectra from assays for *E. coli* O157:H7, *E. herbicola*, and *B. globigii* using the NanoRaman I system. Features diagnostic of a DSNB-derived monolayer formed on the gold nanoparticles are evident. The largest peak, which is located at 1336 cm^{-1}, is the symmetric nitro stretch of the adlayer and is used to quantify the amount of biolyte captured by the antibody-modified substrate. The smaller peaks are aromatic ring modes. The presence of these features, coupled with the increase in their strength with increasing antigen concentration, demonstrates the general effectiveness of the assays.

Dose-response curves were constructed based on the intensity of the symmetric nitro stretch averaged over five different locations on each capture surface. These curves are shown in Figure 2 for all three biolytes: *E. coli* O157:H7, *E. herbicola*, and *B. globigii.* As is evident, the plot for *E. coli* O157:H7 approximates a linear dependence on concentration, whereas those for *E. herbicola* and *B. globigii* begin to plateau at higher concentrations. We suspect these differences arise, in part, from differences in the antigen-antibody binding affinities of the three distinct systems. The limit of detection (LOD) for *E. coli* O157:H7 was 1,000-2,000 cells/mL, with those for *E. herbicola* and *B. globigii*, roughly 8,000 and for 4,000 cfu/mL, respectively. The LOD was calculated from the signal of the blank sample plus three times the standard deviation of the signal of the blank sample. Sample-to-sample variation of the signals was about 10%, adding that these LODs are about five times better than conventional ELISA methods.[21] The spot-to-spot variation was 3-10%, except for the very low concentrations (0 - 10^5 cfu/mL). In these cases, including the blanks, the variation in signal strength was much greater (15 – 100%). For example, the signal on one spot was several hundred counts whereas that at another spot was only few tens of counts. This is

probably because at very low concentrations, only a small number of captured cells is on the assay substrates, leading to a relatively inhomogeneous distribution of the analytes.

As a preliminary assessment of binding specificity for these assays, three groups of capture substrates were prepared, with each group consisting of three capture substrates coated with antibodies for one of the three antigens. Each group was then incubated with matching antigen, i.e., the three capture substrates coated with anti-*E. coli* O157:H7 were incubated with *E. coli* O157:H7 (10^7 cells/mL, Group 1) and likewise for *E. herbicola* (10^7 cfu/mL, Group 2) and and *B. globigii* (10^7 cfu/mL, Group 3). Next, one substrate from each Group was exposed to ERLs™ conjugated with anti-*E. coli* O157:H7, with the same process repeated for incubations with ERLs™ conjugated with anti-*E. herbicola* and with anti-*B. globigii.* This procedure yielded nine samples exposed to all possible combinations of different captured antigens incubated with different antibody-modified ERLs™.

The results from the SERS-characterization of the three Groups are summarized in Figure 3 by the intensity of the symmetric nitro stretch. In all three Groups, the signal level for the substrate with the ERL™ matched with its target antigen was significantly larger than those for the two mismatches. The largest level of nonspecific binding (~10%) was observed for the Group 1 sample that was exposed to the ERLs™ labeled with anti-*E. herbicola.* In contrast, other combinations yielded a much lower level of detectable nonspecific binding (< 2-3%). Collectively, these results begin to demonstrate the effectiveness of this assay format.

Mixed monolayer based ERL™. This section examines an alternative strategy in the design of ERLs™. Key issues in the design of ERLs™ include Raman signal strength,

biospecificity, and the stability of the colloidal suspension after each step in the modification process. Intense Raman scattering is realized by using aromatic compounds (e.g., benzyl and naphthyl thiols and disulfides) that readily chemisorb to the gold nanoparticle surface. Colloidal stability is affected by various parameters, such as the nanoparticle surface coverage of the reporter and antibody, the energetics of the attachment of the antibody to the gold particle (e.g., adsorption vs. covalent coupling), and the pH and ionic strength of the suspending solution. The presence of surfactants in the suspending solution can also be of importance.

In our earlier work, ERLs™ were prepared by a co-immobilization method in which both the antibody and Raman label were directly adsorbed onto the surface of the gold nanoparticle.[18] Figure 4A depicts of this type of ERL™. While successfully applied to the concurrent qualitative analysis of two biolytes (i.e., rat and rabbit IgG), questions remained regarding a contribution to the apparent nonspecific adsorption of the ERLs™ by the possible transfer of weakly adsorbed antibodies from one ERL™ to another ERL™ that had been modified with a distinctly different antibody coating. There would therefore be the possibility of "cross-talk" between different ERLs present in the same solution during a multiplexed labeling step. This approach was also complicated by occasional problems with the stability of the particle suspension, also potentially the result of the desorption of the protein-based coating.

The next scheme developed, shown in Figure 4B, used a bifunctional Raman reporter molecule to covalently couple the antibody to the particles. This scheme improved particle stability and reduced the limit of detection via a lower level of non-specific ERL™

adsorption.[17] Using this type of ERL™, we recently reported on the femtomolar detection of prostate specific antigen (PSA) directly in human serum,[19] and was used in the experiments described above.

This approach, while working with a high level of effectiveness, nevertheless required the synthesis of the bifunctional reporters. Figure 4C introduces a new design for ERLs™ that eliminates the synthesis of a bifunctional reporter, yet incorporates its attributes. In this scheme, the surface of gold nanoparticles is modified with two different thiolates, each derived from commercially available compounds. One thiolate component has a large Raman cross section and serves as the reporter molecule. The other component is derived from the bifunctional compound DSP, which has both a disulfide and a succinimidyl functional group for the respective chemisorption onto gold and the facile covalent coupling of antibodies to the particle. DSP, however, is an intrinsically weak Raman scatterer. This scheme therefore facilitates the production of distinctive ERLs™, referred to hereafter as mixed-monolayer ERLs, for the potential use in multianalyte assays.

To test the effectiveness of this concept, mixed monolayer ERLs™ were constructed using TP, MBA, and DNBA as Raman reporters and DSP as the coupler. Figure 5 presents representative SERS spectra for assays of (A) human IgG, (B) mouse IgG, and (C) *E. herbicola*. Each set of data was obtained using the appropriate capture substrate, prepared by the procedures described earlier. As expected, the spectra in Figures 5A, C exhibit distinctive peaks for TP, with the respective signal strengths increasing as the concentration of human IgG and *E. herbicola* increases. All the observed bands (999, 1022, 1069, and 1568 cm^{-1}) are from aromatic ring modes of the TP label. The assay of mouse IgG used

DNBA, in contrast, as the reporter. These results are given in Figure 5B. These spectra also undergo an increase in signal strength with antigen concentration. We add that the spectrum for the DNBA-based assay is virtually identical to that for the DSNB-derived spectrum, which reflects the use of DNBA as the starting material in the synthesis of DSNB.[19]

These spectra were used to construct the dose response curves shown in Figure 6. The plots for the assays of human IgG and *E. herbicola* employed the peak at 1069 cm^{-1}, whereas that for mouse IgG utilized the peak at 1336 cm^{-1}. Each data point represents the average of five different measurements. Spot-to-spot variation was ~10%. Using the earlier data treatment, limits of detections were estimated at 0.06 ng/mL for human IgG, 0.04 ng/mL for mouse IgG, and 10^4 cfu/mL for *E. herbicola*. The LOD for *E. herbicola* is about the same as was measured using the bifunctional reporter DSNB. This clearly shows that the mixed monolayer ERL™ approach is successfully applied to detection of bacteria and proteins without losing performance. With excellent particle stability and relatively simple preparation, the mixed monolayer ERL™ shows potential to be used not only for single analytes but also for multi analyte assays for various types of biomolecules.

Single *E. coli* O157:H7 SERS. The SERS signal from a single *E. coli* O157:H7 cell was measured using a SERS microscope. After completing the sandwich immunoassay utilizing DSNB-based ERLs™, the laser beam, focused to a spot 2.5 -3 μm in diameter, was placed onto a single *E. coli* O157:H7 cell tagged with ERLs™. Since the size of the laser spot size is comparable to that of *E. coli* O157:H7, the observed signal originates primarily from the irradiated cell and not other portions of the capture substrate. A strikingly large

signal from a single bacterium is evident. (Figure 7A) On the other hand, no signal was observed on the area (Figure 7B) without *E.coli* O157:H7, further demonstrating the selectivity of our ERLs™. In an earlier single particle SERS study,[25] 80 nm DSNB-coated particles gave a SERS signal of ~6 counts/s/particle using the same instrument setup. The signal of ~ 600 counts/s from a single cell, therefore, suggests that the cell is covered with many particles. Moreover, given the large size of *E.coli* O157:H7 cells, it is not expected that ERLs™ captured on the top surface of the cells will contribute strongly to the SERS signal, based on the importance of particle-substrate electromagnetic coupling in producing the enhanced Raman scattering in these experiments and the rapid decay of this coupling as the particle-substrate separation distance increases.[25,26] We estimate that in the previous study, ERLs™ were located somewhere between 10 to 20 nm from the metal substrate. Here, ERLs™ on the upper surface of captured cells could be as much as 1000 nm away from the substrate. It is possible that some ERLs™ are localized around the periphery of the cells and near the substrate. It is also possible that the SERS signal in bacterial assays is further enhanced by particle-particle coupling of ERLs™ on the cell surface. Although not fully investigated, the drying process may have caused the dehydration of the cells, bringing the particles closer to the surface and closer to each other, both contributing to the enhancement of the signal. Nevertheless, this result demonstrated the potential of ERLs™ in single bacterium detection.

Conclusions

The flexibility of Raman labeled immunogold nanoparticles, ERLs™, was successfully demonstrated by the application to the low-level detection of bacteria and spores, i.e., *E. coli* O157:H7 and simulants of BW agents using a bifunctional reporter molecule for ERL™ fabrication. Also, a new labeling design based on mixed monolayer coated gold nanoparticles was introduced and applied in the assay of IgGs and bacteria. The mixed monolayer ERLs™ have proven to perform as well as ERLs™ based on a bifunctional reporter molecule.

ERLs™ were also used to obtain SERS signal from labeled single *E. coli* O157:H7 cells. The result suggested the binding of many ERL™ on each cell, producing a large signal for a single *E. coli* O157:H7.

Acknowledgments

This work was supported by Concurrent Analytical, Inc. through a grant from the DARPA CEROS program and by the Institute for Combinatorial Discovery of Iowa Sate University. The Ames Laboratory is operated for the U.S. Department of Energy by Iowa State University under contract W-7405-eng-82.

References

(1) Henderson, D. A. *Science (Washington, D.C.)* **1999**, *283*, 1279.

(2) Bordet, J.; Renaux, E. *Ann. inst. Pasteur* **1930**, *45*, 1.

(3) Depla, H. *Arch. Int. Pharm. Ther.* **1923**, *28*, 223.

(4) Hewlett, R. J.; Hall, G. N. *J. Hygiene* **1912**, *2*, 473.

(5) Moore, B.; Williams, S. *Biochem. J.* **1911**, *5*, 181.

(6) Vo-Dinh, T.; Griffin, G. D.; Ambrose, K. R. *Appl. Spectrosc.* **1986**, *40*, 696.

(7) Peruski Anne, H.; Johnson Linwood, H., 3rd; Peruski Leonard, F., Jr. *J. Immunol. Methods* **2002**, *263*, 35.

(8) Seaver, M.; Eversole, J. D.; Hardgrove, J. J.; Cary, W. K., Jr.; Roselle, D. C. *Aerosol Sci. Technol.* **1999**, *30*, 174.

(9) Belgrader, P.; Benett, W.; Hadley, D.; Long, G.; Mariella, R., Jr.; Milanovich, F.; Nasarabadi, S.; Nelson, W.; Richards, J.; Stratton, P. *Clin. Chem. (Washington, D. C.)* **1998**, *44*, 2191.

(10) Slavik, R.; Homola, J.; Brynda, E. *Biosens. Bioelectron.* **2002**, *17*, 591.

(11) Koenig, B.; Graetzel, M. *Analy. Lett.* **1993**, *26*, 1567.

(12) Prusak-Sochaczewski, E.; Luong, J. H.; Guilbault, G. G. *Enzyme Microb. Technol.* **1990**, *12*, 173.

(13) Libby, J. M.; Wada, H. G. *J. Clin. Bicrobiol.* **1989**, *27*, 1456.

(14) Yu, H.; Raymonda, J. W.; McMahon, T. M.; Campagnari, A. A. *Biosens. Bioelectron.* **2000**, *14*, 829.

(15) Vidziunaite, R.; Dikiniene, N.; Miliukiene, V.; Mikulskis, P.; Kulys, J. *J. Biolumin. Chemilumin.* **1995**, *10*, 193.

(16) Zhang, X.; Young, M. A.; Lyandres, O.; Van Duyne, R. P. *J. Am. Chem. Soc.* **2005**, *127*, 4484.

(17) Ni, J. In *Chemistry*; Iowa State University: Ames, 2000, pp 135.

(18) Ni, J.; Lipert, R. J.; Dawson, G. B.; Porter, M. D. *Anal. Chem.* **1999**, *71*, 4903.

(19) Grubisha, D. S.; Lipert, R. J.; Park, H.-Y.; Driskell, J.; Porter, M. D. *Anal. Chem.* **2003**, *75*, 5936.

(20) Driskell, J. D.; Kwarta, K. M.; Lipert, R. J.; Porter, M. D.; Neill, J. D.; Ridpath, J. F. *Anal. Chem.* **2005**, *77*, 6147.

(21) McBride, M. T.; Gammon, S.; Pitesky, M.; O'Brien, T. W.; Smith, T.; Aldrich, J.; Langlois, R. G.; Colston, B.; Venkateswaran, K. S. *Anal. Chem.* **2003**, *75*, 1924.

(22) Rowe, C. A.; Tender, L. M.; Feldstein, M. J.; Golden, J. P.; Scruggs, S. B.; MacCraith, B. D.; Cras, J. J.; Ligler, F. S. *Anal. Chem.* **1999**, *71*, 3846.

(23) Wagner, P.; Hegner, M.; Kernen, P.; Zaugg, F.; Semenza, G. *Biophys. J.* **1996**, *70*, 2052.

(24) Niemz, A.; Jeoung, E.; Boal, A. K.; Deans, R.; Rotello, V. M. *Langmuir* **2000**, *16*, 1460.

(25) Park, H.-Y.; Lipert, R. J.; Porter, M. D. *Proc. SPIE-Nanosensing: Mater. and Devices* **2004**, *5593*, 464.

(26) Okamoto, T.; Yamaguchi, I. *J. Phys. Chem. B* **2003**, *107*, 10321.

Figure Captions

Figure 1. Immunoassay results for (A) *E. coli* O157:H7, (B) *E. herbicola,* and (C) *B. globigii.* For *E. coli* O157:H7, solid, dotted, short dashed, dot-dashed, and long-dashed lines indicate SERS spectra for concentrations of 5 x 10^7, 5 x 10^6, 1 x 10^6, 2 x 10^5 cell/mL, and blank, respectively and for *E. herbicola* and *B. globigii*, 1 x

10^8, 1 x 10^7, 2 x 10^6, 4 x 10^5 cfu/mL, and blank, respectively. Sample volumes were 30 μL.

Figure 2. Dose-response curves for (A) *E. coli* O157:H7, (B) *E. herbicola,* and (C) *B. globigii.* These plots were constructed using the intensity of the symmetric nitro stretch (1336 cm^{-1}) from the ERLs. Each data point represents the average signal for measurements from five different locations on each sample. The dashed lines indicate the signal from the blank sample.

Figure 3. SERS signal for substrates covered with *E. coli* O157:H7 (Group 1), *E. herbicola* (Group 2), and *B. globigii* (Group 3) incubated with ERLs™ with anti-*E. coli* O157:H7, anti-*E. herbicola*, and anti-*B. globigii.* Each data bar indicates the signal averaged from five different areas on the sample.

Figure 4. ERL™ schemes based on (A) co-immobilization, (B) bifunctional reporter, and (C) mixed monolayer.

Figure 5. SERS spectra of assays for (A) human IgG, (B) mouse IgG, and (C) *E. herbicola* using the mixed monolayer based ERL™ scheme. For human IgG and mouse IgG, solid , dotted, short dashed , dot-dashed lines are concentrations of 100, 10, 1 ng/mL, and blank, respectively and for E. herbicola, each lines indicate the concentrations of 10^8, 10^6, 10^4, and blank, respectively.

Figure 6. Dose-response curves of assays for (A) human IgG, (B) mouse IgG, and (C) *E. herbicola* using the mixed monolayer based ERL™ scheme.

Figure 7. SERS spectra of (A) a single labeled *E. coli* O157:H7 cell and (B) a blank area.

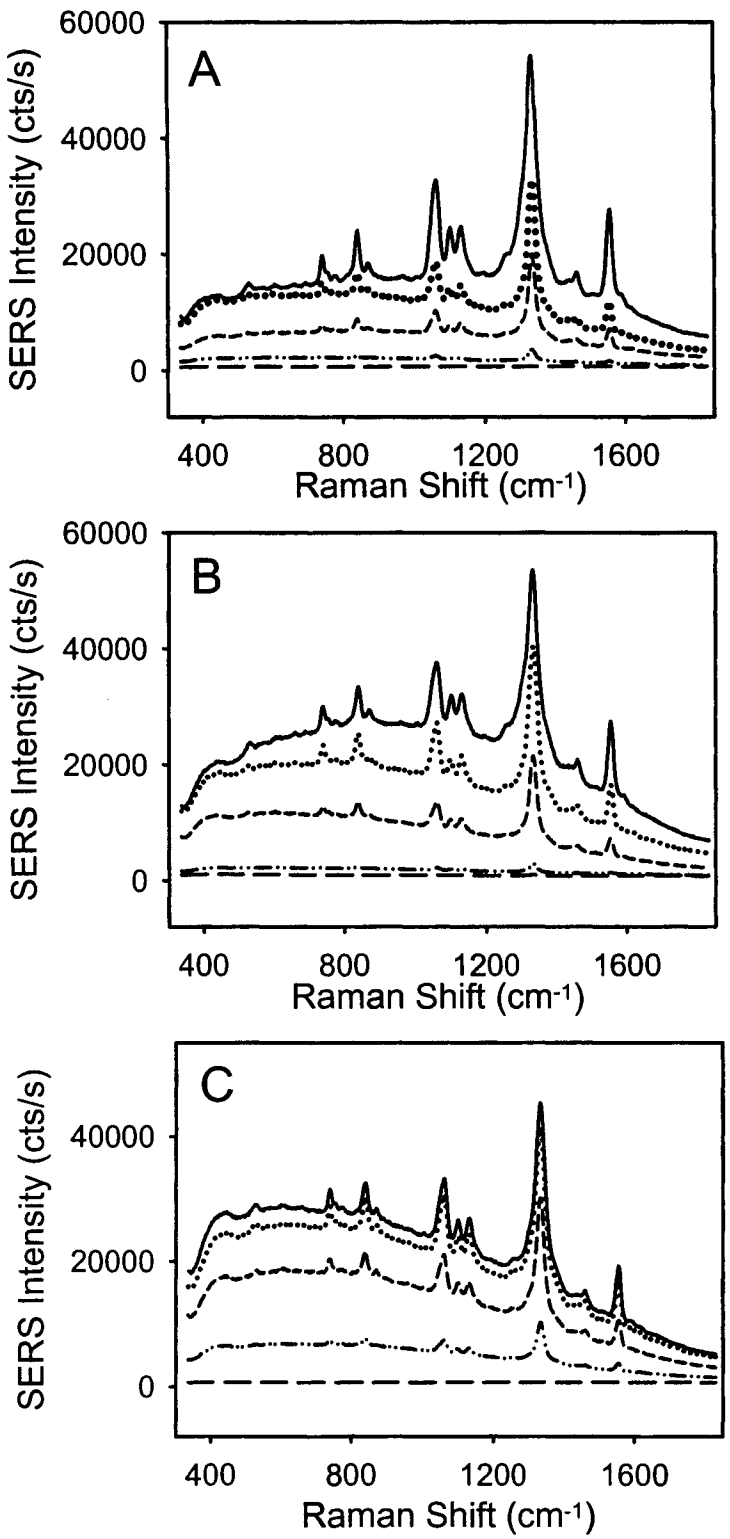
A
B
C
SERS Intensity (cts/s)
60000
40000
20000
0
400
800
1200
1600
Raman Shift (cm-1)

Figure 1.

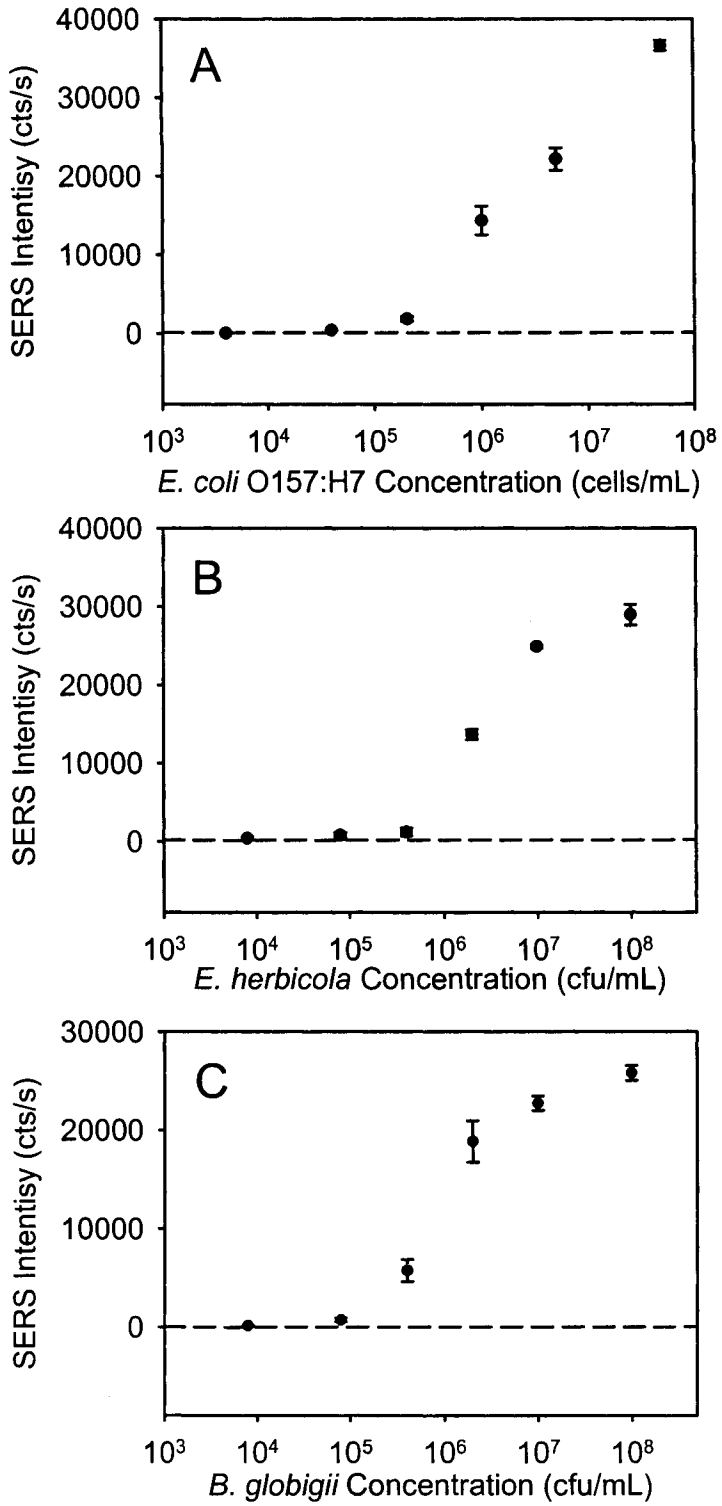
A
SERS Intentisy (cts/s)
40000
30000
20000
10000
0
10^3 10^4 10^5 10^6 10^7 10^8
E. coli O157:H7 Concentration (cells/mL)
B
SERS Intentisy (cts/s)
40000
30000
20000
10000
0
10^3 10^4 10^5 10^6 10^7 10^8
E. herbicola Concentration (cfu/mL)
C
SERS Intentisy (cts/s)
30000
20000
10000
0
10^3 10^4 10^5 10^6 10^7 10^8
B. globigii Concentration (cfu/mL)

Figure 2.

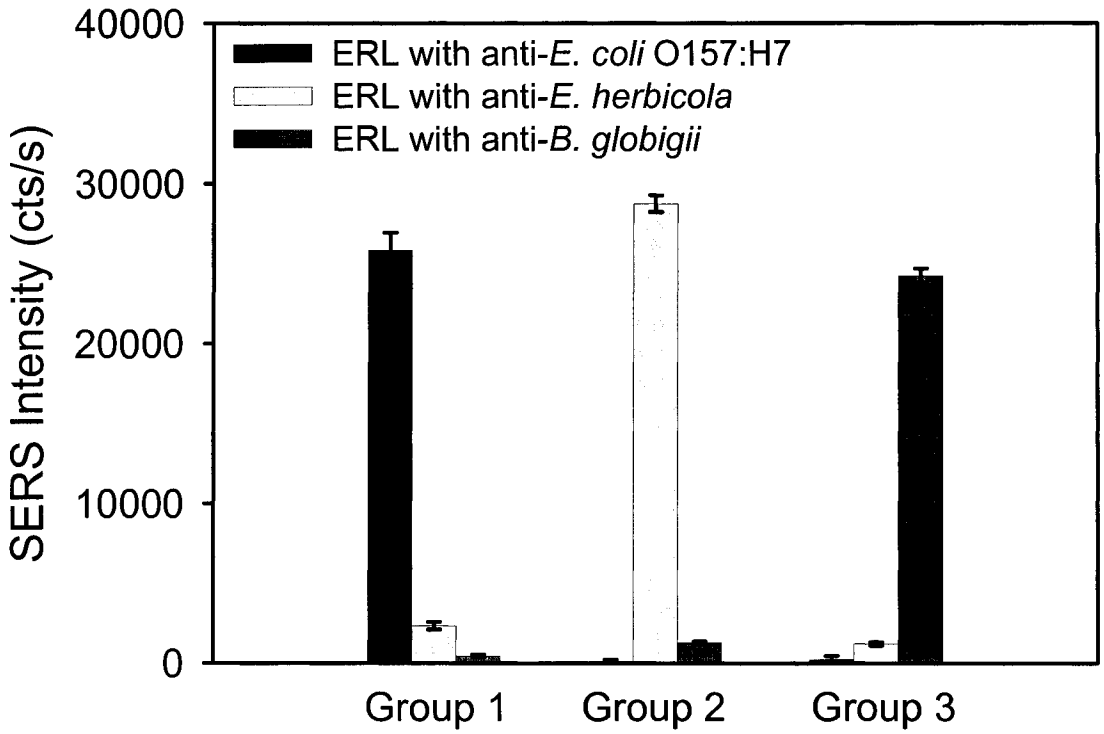
40000
30000
20000
10000
0
SERS Intensity (cts/s)
ERL with anti-E. coli O157:H7
ERL with anti-E. herbicola
ERL with anti-B. globigii
Group 1
Group 2
Group 3

Figure 3.

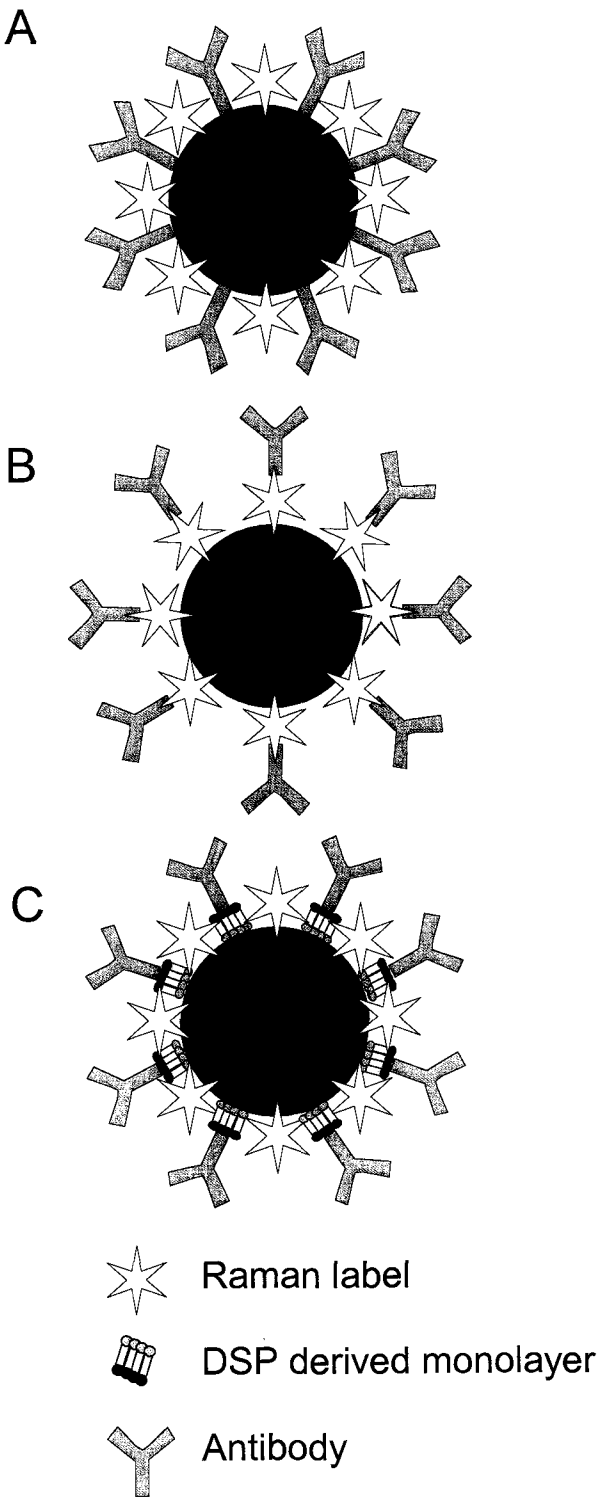

Figure 4.

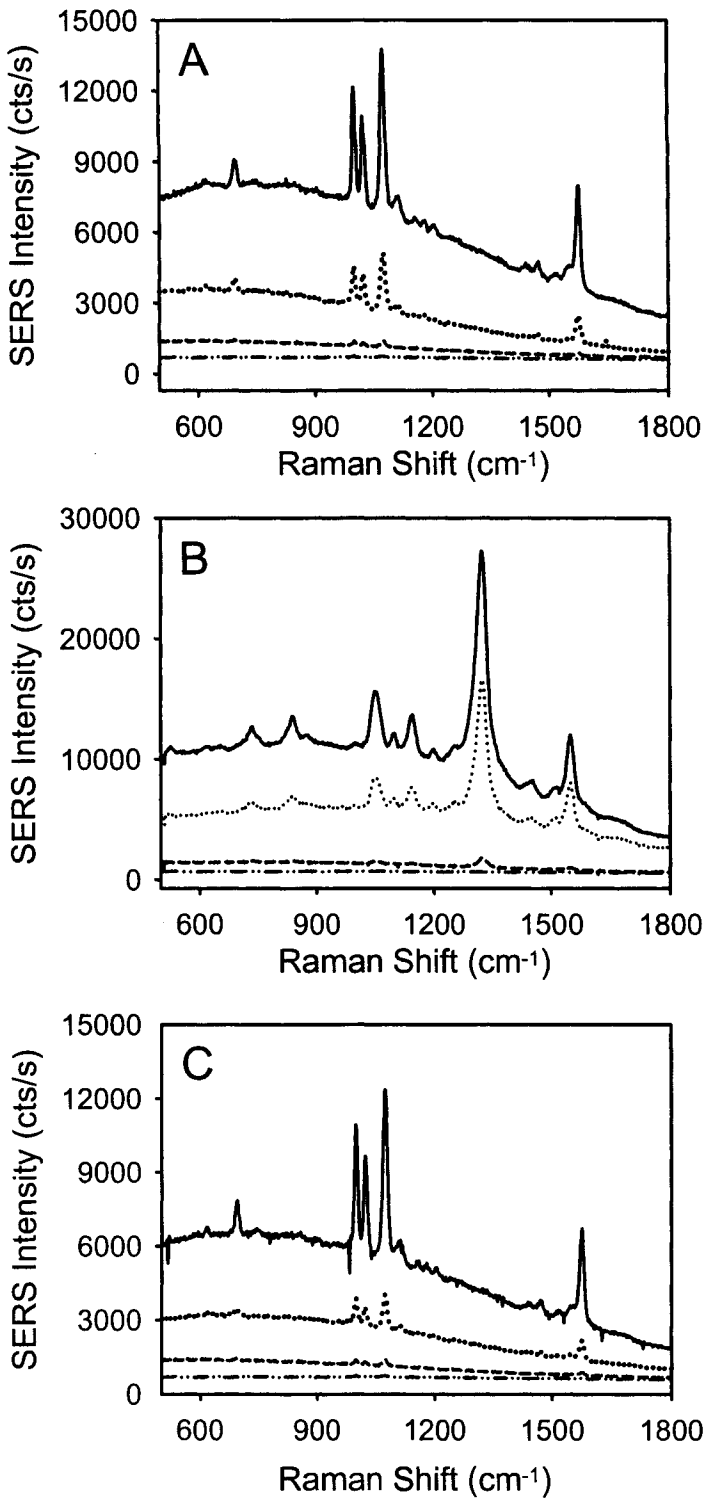
A
SERS Intensity (cts/s)
15000
12000
9000
6000
3000
0
600
900
1200
1500
1800
Raman Shift (cm-1)
B
SERS Intensity (cts/s)
30000
20000
10000
0
600
900
1200
1500
1800
Raman Shift (cm-1)
C
SERS Intensity (cts/s)
15000
12000
9000
6000
3000
0
600
900
1200
1500
1800
Raman Shift (cm-1)

Figure 5.

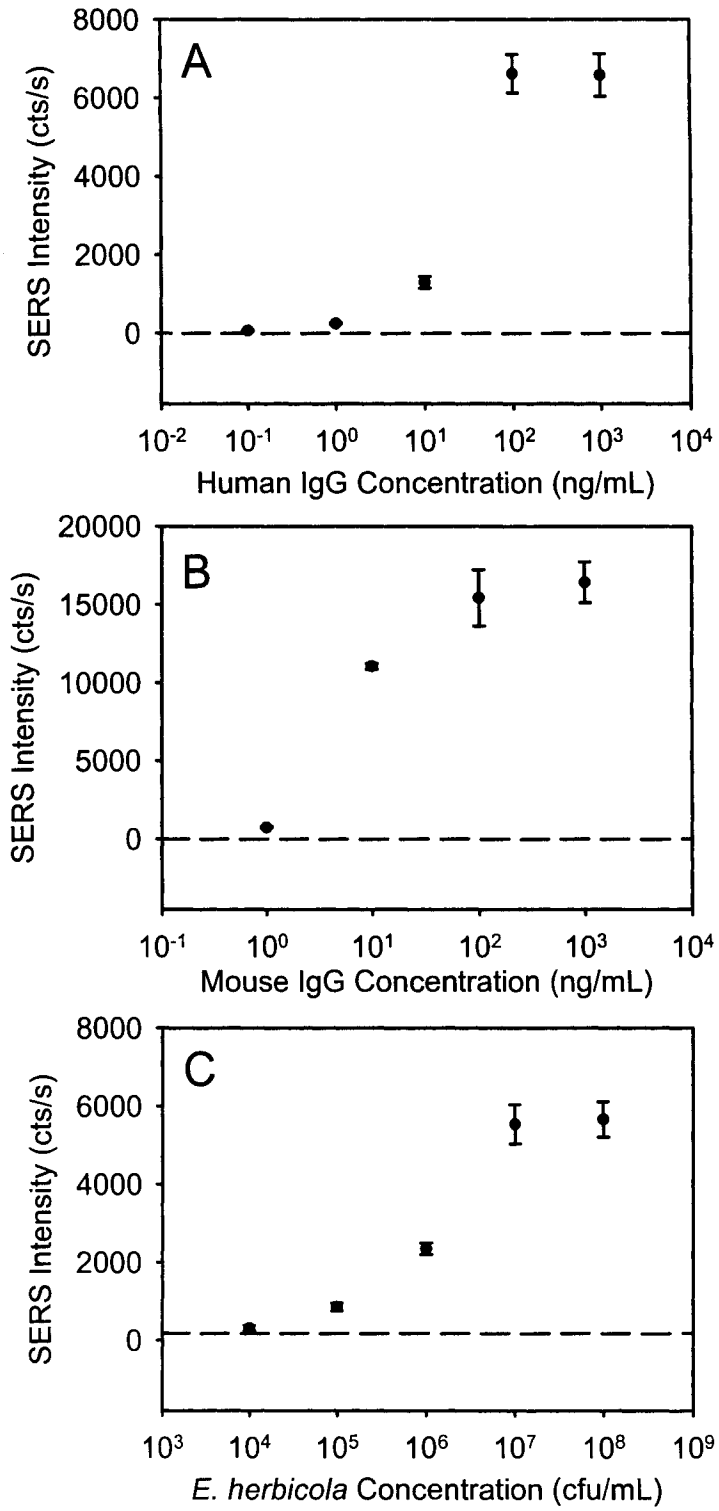
A
SERS Intensity (cts/s)
8000
6000
4000
2000
0
10^{-2} 10^{-1} 10^{0} 10^{1} 10^{2} 10^{3} 10^{4}
Human IgG Concentration (ng/mL)
B
SERS Intensity (cts/s)
20000
15000
10000
5000
0
10^{-1} 10^{0} 10^{1} 10^{2} 10^{3} 10^{4}
Mouse IgG Concentration (ng/mL)
C
SERS Intensity (cts/s)
8000
6000
4000
2000
0
10^{3} 10^{4} 10^{5} 10^{6} 10^{7} 10^{8} 10^{9}
E. herbicola Concentration (cfu/mL)

Figure 6.

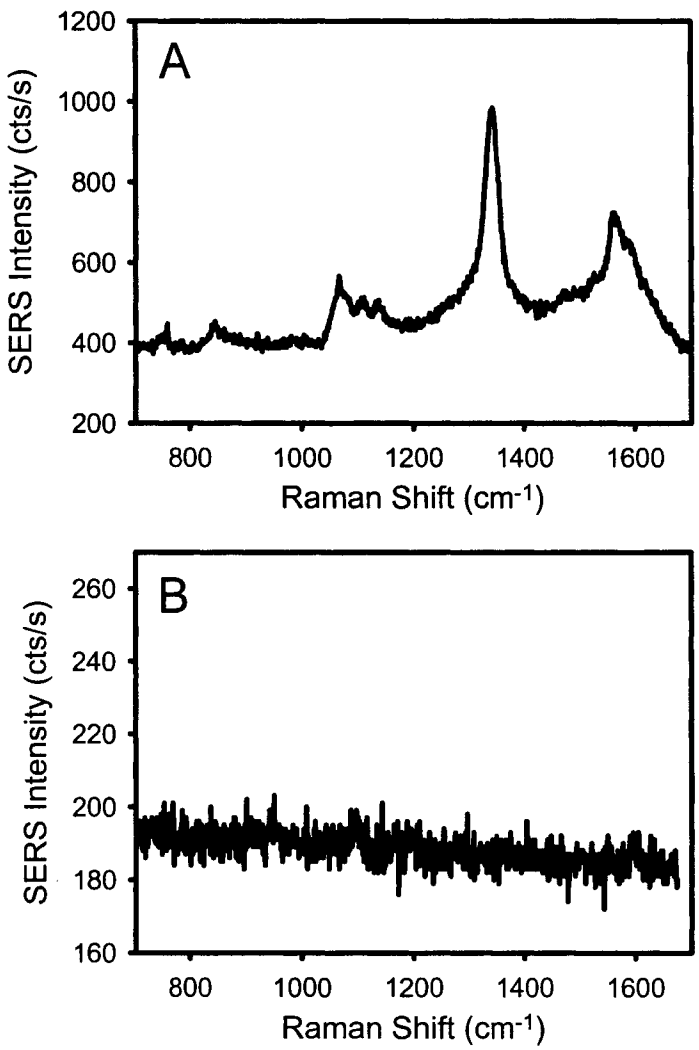
A
SERS Intensity (cts/s)
1200
1000
800
600
400
200
800
1000
1200
1400
1600
Raman Shift (cm-1)
B
SERS Intensity (cts/s)
260
240
220
200
180
160
800
1000
1200
1400
1600
Raman Shift (cm-1)

Figure 7.

CHAPTER 4. CONTROL OF ANTI-PROSTATE SPECIFIC ANTIGEN ADSORPTION USING MIXED SELF-ASSEMBLED MONOLAYERS OF TRI (ETHYLENE GLYCOL) MONOMETHYL ETER - AND N-HYDROXYSUCCINIMIDYL- TERMINATED ALKANETHIOLS ON GOLD

A manuscript in preparation for submission to *Langmuir*

Hye-Young Park[1] and Marc D. Porter[1,2]

Abstract

Surface antibody density was controlled by using mixed self-assembled monolayers. The mixed monolayers were prepared from dithiobis(succinimidyl undecanoate) (DSU) and triethyeneglycol monomethyl ether (EG3OMe)-terminated thiol. Mole fraction of DSU (χ_{DSU}) was varied. Borate buffer solution containing anti-PSA was incubated on the mixed monolayers. Atomic force microscopy was used to image individual anti-PSA on mixed monolayers. As χ_{DSU} increased, number of anti-PSA on the surface increased. IRRAS measurement verified the covalent binding of anti-PSA on DSU derived monolayer.

Introduction

Control of capture antibody coverage is important in multi-analyte sandwich immunoassays utilizing a single address. Investigations of individual antigen-antibody binding events based on scanning force microscopy also often require spatial separation of individual capture antibodies.[1-4] Our novel immunoassay readout method using Raman labeled immunogold nanoparticles, also called Extrinsic Raman labels (ERLs), showed potential for multiplexing.[5] ERLs are coupled with Raman reporter molecules for strong

[1] Ames Laboratory – U.S. DOE and Department of Chemistry, Iowa State University, Ames, Iowa 50011
[2] Corresponding Author

Raman signal and antibodies for biospecificity. While ERLs present successful assay results for single analyte assays[6,7] and qualitative assays for dual-analytes,[8] quantitative dual-analyte assay was complicated by steric hindrance, i.e., if ERL of analyte A has greater binding affinity and if analyte B is located close to analyte A, the ERL of analyte B cannot bind on its analyte (Figure 1). Therefore, correlations between SERS signal versus concentration of each analyte affected the binding affinities of each ERLs.[2] In another format of immunoassay, gold nanoparticles of different sizes were utilized for dual-analyte assays of IgGs. The study also suggested that the reduced response for one analyte comes from steric and diffusional constraints. Therefore, creating capture substrates to address those issues is important. By carefully controlling the surface antibody coverage, the capture antibodies can be separated out to have inter-antibody separations larger than the size of labeled antibodies. It is also important to minimize nonspecific adsorption of labeled antibodies while maximizing epitope density.

In developing capture antibody surfaces to meet those requirements, mixed self-assembled monolayers (SAMs) can provide well-defined structure with a well-defined average surface density and be a good model system to study the effect of the fraction of the different functionalities on the adsorption of protein.[9] Dong *et al.* utilized mixed monolayers formed from two different components, one with ability to couple the antibody and the other one without specific interaction with antibody, and showed that by varying molar ratio between the two components, antibody coverage could be varied.[3] However, SAMs formed from thiols with shorter chain length are known to be less ordered and less stable than those formed from thiols with a longer chain length. Also, butanethiol is not well known for resisting protein and the authors observed some nonspecific adsorption, although not discussed in detail.

Surfaces that resist the nonspecific adsorption of proteins are of particular importance as functional coatings to reduce background response.[10-14] Poly (ethylene glycol) (PEG) is known to be protein-repelling due to steric repulsion originating from the high conformational freedom of the chains and tightly bound water molecules.[15-19] In the past decade, self-assembled monolayers (SAMs) of OEG moieties have also proven to resist the adsorption of biomolecules and have become the standard for comparison.[20-26] One of the most studied groups of OEG is 1-undecanethiolate with a methoxy-terminated tri(ethylene glycol) (EG3-OMe). Studies on the interaction of water with OEG suggest that the resistance in the OEG-terminated SAMs is result of the ability of the different conformations to bind water, resulting in the stability of interfacial water that prevents the protein from contacting the surface. [27-33]

We employed two different precursors to form mixed monolayers with longer chain alkanethiolates (n>10) which are known to provide more ordered monolayers. Two SAMs used in our mixed monolayer study are that formed from dithiobis succinimidyl undecanoate (DSU) and that formed from (undec-11-mercapto-1-yl) triethylene glycol (EG3-OMe). DSU has succinimidyl functional groups which react with the primary amine group on protein forming a covalent binding. The solution ratio between EG3OMe and DSU was varied and subsequently exposed to anti-PSA. Atomic force microscopy (AFM) was used to image and count the number of antibody molecules bound on each surface.

Experimental section

Reagents. Capture anti-human f-PSA was purchased from BiosPacific. Tween 80, bovine serum albumin (BSA), octadecanethiol (ODT), 11-bromoundec-1-ene, triethylene glycol monomethyl ether, sodium hydride, 9-borabicyclononane (9-BBN) in hexane, sodium

hydroxide, hydrogen peroxide, sodium bicarbonate, pyridine, tosyl chloride, and hydrochloric acid were purchased from Sigma-Aldrich. Borate buffer packages were obtained from Pierce. Two-part epoxy was obtained from Epotek. Dithiobis (succinimidyl undecanoate) (DSU) was synthesized by a modification of a literature procedure.[34] Deionized water (18 MΩ), purified with a Millipore system, was used in the preparation of all aqueous solutions.

Synthesis of EG3OMe. All the reactions were performed under a purge with N_2 gas and all the solvents were carefully dried prior to use. In a volumetric flask with 150 mL of tetrahydrofuran, 13.2 mL of 11-bromoundec-1-ene, 4.77 mL of triethylene glycol monomethyl ether, and 2.30 g of sodium hydride were added. The reaction mixture was stirred overnight. This step, via nucleophilic substitution, produces (undec-10-en-yl) triethylene glycol methyl ether. To the mixture, 1 mL of 2-propanol and 2 mL of deionized water were added and the mixture was further diluted with 20 mL of DI water, extracted three times with hexane, and the organic layer was rotor evaporated to remove the solvent.

In the second step, to the reaction flask, 9-BBN was added and stirred for 4 h, followed by the addition of ethanol, 6 M NaOH, 30% hydrogen peroxide, and a 1-h reflux. Then, saturated sodium bicarbonate was added and the organic layer was rotor evaporated. This process produced (undec-11-hydroxy-1-yl) triethylene glycol monomethyl ether.

In the third step, pyridine and tosyl chloride were added sequentially to the flask in ice bath and stirred for 1 h. The mixture was refrigerated overnight. The next day, 15 mL of deionized water was added to the mixture, which was then extracted three times with methylene chloride and back extracted three times with 10% hydrochloric acid. The organic layer was dried with magnesium sulfate, filtered, and rotor evaporated. In this step, (undec-11-tosyl-1-yl) triethylene glycol monomethyl ether is produced.

Finally, to the product of the third step was added degassed ethanol and thiourea and refluxed for 4 h and rotor evaporated. The product was stirred with 1.10 g sodium hydroxide in 10 mL deionized water overnight. This step formed the final product, (undec-11-mercapto-1-yl) triethylene glycol (EG3-OMe) monomethyl ether. The aqueous solution was boiled for 15 min and 15 mL of deionized water was added. Then, the aqueous layer was acidified with concentrated sulfuric acid. The solution was extracted three times with methylene chloride, dried with magnesium sulfate, and finally rotor evaporated. The product was characterized with H_1 NMR ($CDCl_3$): δ 3.5 (15H) and 1.5(22H).

Substrate preparation. Three different gold substrates were prepared, based on annealing, template-stripping, or e-beam evaporation methods, to create atomically smooth surfaces. A highly smooth surface is required in order to readily image the nanometer-sized footprints of the covalently coupled antibodies to the mixed monolayer surfaces. First, single crystal gold surface was prepared by a flame annealing method.[35] Cleaned gold wire was melted in an oxygen-hydrogen flame, and the surface was cooled in deionized water. The gold surfaces formed from this method are reported to be Au(111)- facets.[35] Gold surfaces were also fabricated by e-beam evaporation under high temperature (200 C°) and a slow rate of evaporation (0.05 Å/s). Finally, template-stripped gold (TSG) substrates were formed. In this procedure, silicon (111) wafers were cleaned in hexanol, acetone, and methanol, respectively, under sonication for 30 min each, and dried with high purity nitrogen gas. The cleaned wafers were placed in an evaporator (Edwards) and coated with a 300-nm gold film. Next, glass slides were cut into 1 x 1 cm sections and sonicated in surfactant (Contrad) containing water, deionized water, and methanol (30 min each), and dried under a stream of nitrogen gas. Two-part epoxy was used to affix the glass pieces on the gold on silicon wafers. The substrate was then baked in the oven at 150 °C for 90 min.

By carefully detaching the glass section, a freshly exposed gold side was obtained. The antibody-covered area was defined by using a poly (dimethylsiloxane) stamp (Dow Corning) coated with ODT.[36]

The gold substrates for IRRAS measurements were prepared by the resistive evaporation of gold layers (300 nm) with chromium adhesion layer (15 nm) in a vacuum evaporator (Edward).

Monolayer preparation. Ethanolic solutions with various mole fractions of DSU and EG3OMe were prepared, spanning solutions of only EG3OMe to only DSU. The total concentration of the two thiols was fixed to 0.1 mM. The adlayers were formed by immersing the ODT-stamped gold substrate in each solution for 24 h. The samples were then rinsed with ethanol, and dried under a stream of high purity nitrogen gas.

Binding of anti-PSA. The antibody modification step pipetted 35 μL of 100 μg/mL of anti-PSA in 50 mM borate buffer (pH 9.0) onto each gold substrate; The derivatization reaction was allowed to proceed for 12 h. After incubation, the substrates were rinsed in 25 mM borate buffer with 1% Tween 80.

AFM. All images were obtained in TappingMode^{TM} under ambient conditions using a Multimode NanoScope III AFM (Digital Instruments). The instrument was equipped with a 125-μm tube scanner. The tips were silicon TESP probes (Nanosensors), with resonance frequencies between 298 and 365 k Hz.

Infrared reflection absorption spectroscopy (IRRAS). For IRRAS, a Nicolet 750 FT-IR spectrometer, which is purged with liquid N_2 and equipped with a liquid-N_2 cooled HgCdTe detector was used. All spectra were collected using *p*-polarized light at an incident angle of 82° with respect to the surface normal. The spectra were recorded as $-\log(R/R_0)$, where R is the reflectance of the sample and R_0 is the reflectance of an octadecanethiolate-

d_{37} monolayer-coated Au(111) reference. The spectra are an average of 512 scans and were taken at a resolution of 2 cm^{-1} with Happ-Genzel apodization. These samples were prepared using as evaporated gold substrates, supported on glass slides. After acquiring the IR spectra of the mixed monolayers, samples were exposed to a solution of anti-PSA in borate buffer for 12 h. The samples were again rinsed with buffer and deionized water, dried with N_2, and characterized by IRRAS.

Results and Discussion

Fabrication of gold substrate. As a starting point, gold substrates prepared from e-beam evaporation-, flame annealing-, and TSG- methods were compared. Figure 2 presents AFM images of gold substrates prepared by the three methods. Gold film prepared by e-beam evaporation provided rough surfaces with large islands (Figure 2A). This suggests that the gold island formed initially went through melting and growing cycles, leading to surface with rough features.[37]

Single crystal gold (111) prepared by flame annealing method provided large smooth areas (Figure 2B) (up to about several tens of mm^2). The surface showed cross-hatching shaped lines which are indicating the crystalline structure. Zooming into much smaller area revealed the gold (111) atomic structure of the surface. Roughness throughout the surface was ~0.7 nm.

The gold surface prepared by TSG method showed the largest atomically smooth areas (Figure 2C). The roughness was less than 0.5 nm on most of the sample area (~1cm^2). Although gold surfaces fabricated by flame annealing method provided surface with comparable roughness on large area, their shape (ball type) made it challenging to be imaged by AFM. Therefore, TSG substrates were used for the imaging of anti-PSA.

Monolayer formation. On the TSG substrates, mixed monolayers were formed then imaged with AFM to verify surface smoothness. In order to image antibodies that are several nanometers in size, monolayers must be featureless. As will be discussed in Chapter 5, nonspecific adsorption of biomolecules is also influenced by surface topography such as defect sites and roughness. Figure 3A shows AFM image of DSU monolayer. There are many objects bound on the monolayer surface, feature sizes varied from about 3-5 to 40-50 nm. These objects are probably from remaining impurity from synthesis procedure. DSU was recrystallized one more time to study the effect of purification. As shown in Figure 3B, the monolayer from DSU after recrystallization presents a much lower number of the objects. Therefore, for the antibody immobilization, monolayers formed after multiple recrystallizations of the precursors were used. Figure 3C shows corresponding Raman spectra of the DSU derived monolayers. Huge fluorescence background profile from the impurity disappeared after purification of DSU. Also, the total concentration of ethanolic solution of DSU and EG3OMe was important as fewer features were observed on the monolayers formed from solution with total concentration 0.1mM of DSU and EG3OMe than that formed from solution with total concentration of 1 mM.

Figure 4 shows the examples of EG3OMe monolayer (Figure 4A) and mixed monolayer formed from DSU and EG3OMe (Figure 4B). In both cases, monolayers were nearly featureless. The mixed monolayers from all the tested χ_{DSU} values exhibited similar surface images.

The monolayers were characterized by IRRAS. Figure 5 show IR spectra of SAMs from DSU and EG3OMe. For DSU-derived monolayer, bands in 1787 cm^{-1} and 1750 cm^{-1} are attributed to in-phase and out-of-phase C=O stretches of the succinimidyl group respectively and the band in 1816 cm^{-1} is from C=O stretch of the ester. The bands at 1218

cm^{-1} and 1077 cm^{-1} arise from the C-N-C stretch and N-C-O stretch from the succinimidyl group.[38] For EG3OMe-derived monolayer, a distinctive band at 1125 cm^{-1} is from C-O-C stretch mode and small peaks around 1353 cm^{-1} are from OCH_2 wag modes.[30] These IR spectra verify the formation of SAMs of the DSU and EG3OMe.

Anti-PSA binding. Anti-PSA (100 μg/mL in borate buffer, pH 9.0) was incubated on the mixed monolayers formed from the solutions of mixture with χ_{DSU} value of 0, 0.048, 0.09, 0.17, 0.29, 0.41, 0.5, and 1.

The AFM results from anti-PSA binding on mixed monolayers are presented in Figure 5. It is clear that the number of anti-PSA increases as χ_{DSU} increases. For the monolayer formed from EG3OMe (Figure 6A), minimal binding of anti-PSA was observed. There was only 0-2 anti-PSA bound on the surface of EG3OMe derived monolayer indicating an excellent ability to resist anti-PSA binding. This control experiment suggests that the anti-PSA binding is mainly because of portion of monolayer formed from DSU.

For the mixed monolayer substrates containing DSU monolayer, anti-PSA started to appear (Figure 6B-G)). Figure B shows anti-PSA randomly spread out on the surface of mixed monolayer with χ_{DSU} of 0.048. Only height measurements were performed due to the tip convolution effect of AFM.[39] The height of anti-PSA varied from 1-3 nm indicating random orientation of antibodies. The height of anti-PSA appeared to be small compared with that estimated from X-ray experiments (10 nm)[40] and that from the experiment done previously in Shannon's laboratory (7 nm).[3] This is probably due to the drying procedure prior to imaging, causing dehydration of anti-PSA. A greater number of anti-PSA was observed on the surface of mixed monolayer with χ_{DSU} of 0.09. For the rest of the substrates, the number of anti-PSA was observed to continue to increase for higher DSU contents until it reached χ_{DSU} of 0.5. On the mixed monolayer with χ_{DSU} of 0.5, surface was fully packed

with anti-PSA as no underlying monolayer was seen. Figure 6H shows anti-PSA on monolayer from all DSU (i.e., χ_{DSU} =1.0). Surface is fully covered with anti-PSA as in the mixed monolayer formed from solution with χ_{DSU} of 0.5. However, anti-PSA showed more aggregated state on the monolayer from all DSU.

Figure 7 shows a plot of the number of anti-PSA as a function of χ_{DSU}. There is a nearly linear increase in the number of anti-PSA in the region as the value χ_{DSU} increases from 0 to 0.5. Desired surface anti-PSA coverage can be achieved by simply varying χ_{DSU} value.

IRRAS was used to verify the chemistry, i.e. covalent binding of anti-PSA on DSU derived monolayer. Figure 8 shows IRRA Spectrum of DSU derived monolayer after exposure to anti-PSA. For monolayer of DSU, upon exposure to anti-PSA, the magnitude of bands responsible for the succinimidyl and ester functionalities decreased and new bands have appeared at 3295, 1666, and 1544 indicative of a N-H stretch, the amide I, and amide II modes, respectively.[38] When the monolayer was formed from EG3OMe entirely, the features on the spectra did not change after exposure to the anti-PSA confirming minimal binding of anti-PSA on EG3OMe monolayer.

Conclusions

We have shown that surface antibody coverage can be controlled by using mixed monolayer formed from dithiobis(succinimidyl undecanoate) (DSU)and triethylene glycol monomethyl ether (EG3OMe) terminated thiol. The results showed that number of anti-PSA increases correspondingly as χ_{DSU} increases linearly and maximizes at χ_{DSU} of 0.5. Minimal binding of anti-PSA was observed on EG3OMe derived monolayer demonstrating

ability of EG3OMe monolayer to prevent nonspecific adsorption of anti-PSA. The IRRAS verified covalent binding of anti-PSA on DSU derived monolayer.

Acknowledgement

This work was supported by Ames Laboratory, operated for U.S. Department of Energy by Iowa State University under Contract No. W-8405-eng-82.

References

(1) Driskell, J.; Kwarta, K.; Kenseth, J. R.; Porter, M. D. *Combinatorial Materials Science*; Wiley, In press.

(2) Kenseth, J. R. In *Chemistry*; Iowa State University: Ames, 2000.

(3) Dong, Y.; Shannon, C. *Anal. Chem.* **2000**, *72*, 2371.

(4) Jones, V. W.; Kenseth, J. R.; Porter, M. D.; Mosher, C. L.; Henderson, E. *Anal. Chem.* **1998**, *70*, 1233.

(5) Ni, J.; Lipert, R. J.; Dawson, G. B.; Porter, M. D. *Anal. Chem.* **1999**, *71*, 4903.

(6) Grubisha, D. S.; Lipert, R. J.; Park, H.-Y.; Driskell, J.; Porter, M. D. *Anal. Chem.* **2003**, *75*, 5936.

(7) Driskell, J. D.; Kwarta, K. M.; Lipert, R. J.; Porter, M. D.; Neill, J. D.; Ridpath, J. F. *Anal. Chem.* **2005**, *77*, 6147.

(8) Ni, J.; Lipert, R. J.; Dawson, G. B.; Porter, M. D. *Anal. Chem.* **1999**, *71*, 4903.

(9) Love, J. C.; Estroff, L. A.; Kriebel, J. K.; Nuzzo, R. G.; Whitesides, G. M. *Chem. Rev.* **2005**, *105*, 1103.

(10) Kasemo, B. *Surf. Sci.* **2002**, *500*, 656.

(11) Holland, N. B.; Qiu, Y.; Ruegsegger, M.; Marchant, R. E. *Nature (London)* **1998**, *392*, 799.

(12) Niklason, L. E. *Science (Washington, D.C.)* **1999**, *286*, 1493.

(13) Tampieri, A.; Celotti, G.; Landi, E.; Sandri, M.; Roveri, N.; Falini, G. *J. Biomed. Mater. Res., A* **2003**, *67A*, 618.

(14) Lee, L. K.; Roth, C. M. *Curr. Opin. Biotechnol.* **2003**, *14*, 505.

(15) Desai, N. P.; Hubbell, J. A. *Biomaterials* **1991**, *12*, 144.

(16) Jeon, S. I.; Lee, J. H.; Andrade, J. D.; De Gennes, P. G. *J. Colloid Interface Sci.* **1991**, *142*, 149.

(17) Jeon, S. I.; Andrade, J. D. *J. Colloid Interface Sci.* **1991**, *142*, 159.

(18) Szleifer, I. *Biophys. J.* **1997**, *72*, 595.

(19) Halperin, A. *Langmuir* **1999**, *15*, 2525.

(20) Pale-Grosdemange, C.; Simon, E. S.; Prime, K. L.; Whitesides, G. M. *J. Am. Chem. Soc.* **1991**, *113*, 12.

(21) Prime, K. L.; Whitesides, G. M. *Science (Washington, D.C.)* **1991**, *252*, 1164.

(22) Feldman, K.; Haehner, G.; Spencer, N. D.; Harder, P.; Grunze, M. *J. Am. Chem. Soc.* **1999**, *121*, 10134.

(23) Schwendel, D.; Dahint, R.; Herrwerth, S.; Schloerholz, M.; Eck, W.; Grunze, M. *Langmuir* **2001**, *17*, 5717.

(24) Zhu, B.; Eurell, T.; Gunawan, R.; Leckband, D. *J. Biomed. Mater. Res.* **2001**, *56*, 406.

(25) Zheng, J.; Li, L.; Tsao, H.-K.; Sheng, Y.-J.; Chen, S.; Jiang, S. *Biophys. J.* **2005**, *89*, 158.

(26) Pertsin, A. J.; Hayashi, T.; Grunze, M. *J. Phys. Chem. B* **2002**, *106*, 12274.

(27) Pertsin, A. J.; Grunze, M. *Langmuir* **2000**, *16*, 8829.

(28) Archambault, J. G.; Brash, J. L. *Colloids Surf., B* **2004**, *33*, 111.

(29) Zheng, J.; Li, L.; Chen, S.; Jiang, S. *Langmuir* **2004**, *20*, 8931.

(30) Harder, P.; Grunze, M.; Dahint, R.; Whitesides, G. M.; Laibinis, P. E. *J. Phys. Chem. B* **1998**, *102*, 426.

(31) Zolk, M.; Eisert, F.; Pipper, J.; Herrwerth, S.; Eck, W.; Buck, M.; Grunze, M. *Langmuir* **2000**, *16*, 5849.

(32) Pertsin, A. J.; Grunze, M.; Garbuzova, I. A. *J. Phys. Chem. B* **1998**, *102*, 4918.

(33) Wang, R. L. C.; Kreuzer, H. J.; Grunze, M. *J. Phys. Chem. B* **1997**, *101*, 9767.

(34) Wagner, P.; Kernen, P.; Hegner, M.; Ungewickell, E.; Semenza, G. *FEBS Lett.* **1994**, *356*, 267.

(35) Hossick Scott, J.; White, H. S. *Langmuir* **1994**, *10*, 486.

(36) Kumar, A.; Biebuyck, H. A.; Whitesides, G. M. *Langmuir* **1994**, *10*, 1498.

(37) Doron-Mor, I.; Barkay, Z.; Filip-Granit, N.; Vaskevich, A.; Rubinstein, I. *Chem. Mater.* **2004**, *16*, 3476.

(38) Frey, B. L.; Corn, R. M. *Anal. Chem.* **1996**, *68*, 3187.

(39) Butt, H.-J.; Gerharz, B. *Langmuir* **1995**, *11*, 4735.

(40) Silverton, E. W.; Navia, M. A.; Davies, D. R. *Proc. Natl. Acad. Sci. U.S.A.* **1977**, *74*, 5140.

Figure Captions

Figure 1. Schematic of dual-analyte assay using ERL.

Figure 2. AFM images of gold substrates prepared by (A) e-beam evaporation method, (B) oxygen-hydrogen flame annealing method, and (C) TSG method.

Figure 3. AFM images of DSU monolayer (A) before and (B) after extra recrystallization, and (C) corresponding Raman spectra of DSU monolayer.

Figure 4. TappingMode™ topographic AFM images of (A) EG3OMe derived monolayer and (B) mixed monolayer formed from ethanolic solution with mixture of DSU and EG3OMe with $\chi_{DSU} = 0.5$. The monolayers were allowed to form for 24 h.

Figure 5. IRRAS spectrum of DSU (upper) and EG3OMe (lower) derived monolayers at gold substrates.

Figure 6. TappingMode™ topographic AFM images of anti-PSA incubated on mixed monolayers of DSU and EG3OMe with χ_{DSU} value of (A) 0, (B) 0.048, (C) 0.09, (D) 0.17, (E) 0.29, (F) 0.41, (G) 0.5, and (H) 1.0.

Figure 7. Number of anti-PSA immobilized on mixed monolayers formed from ethanolic solution of mixture of DSU and EG3OMe as a function of χ_{DSU}.

Figure 8. IRRA spectrum of DSU derived monolayer after binding of anti-PSA. The anti-PSA was incubated on DSU for 12 h.

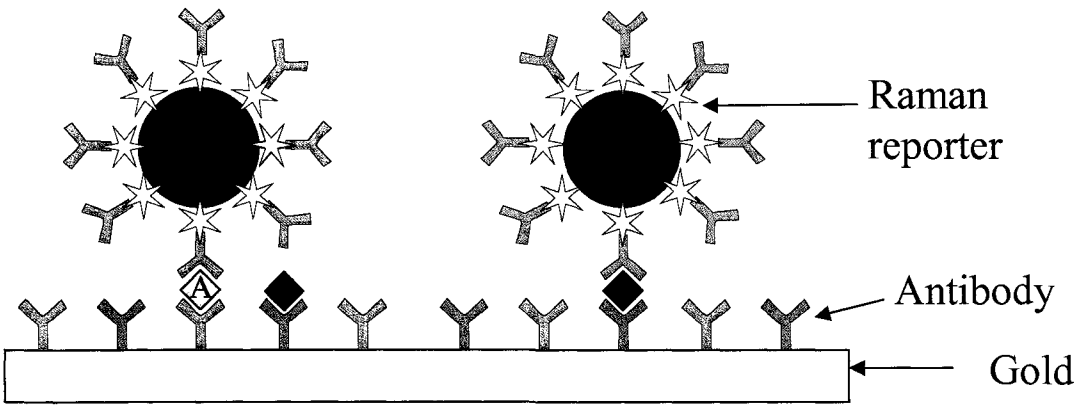

Figure 1.

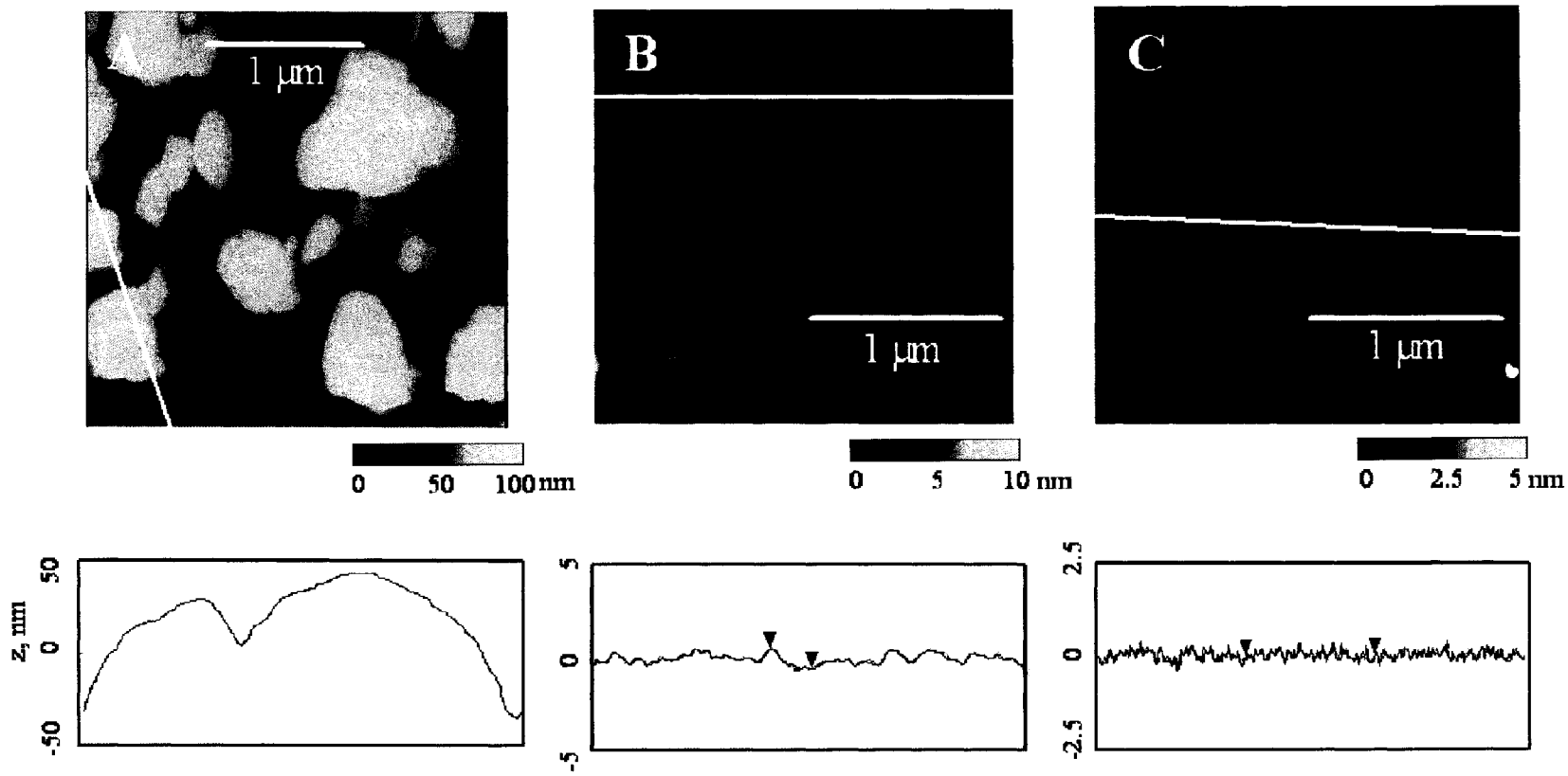

Figure 2.

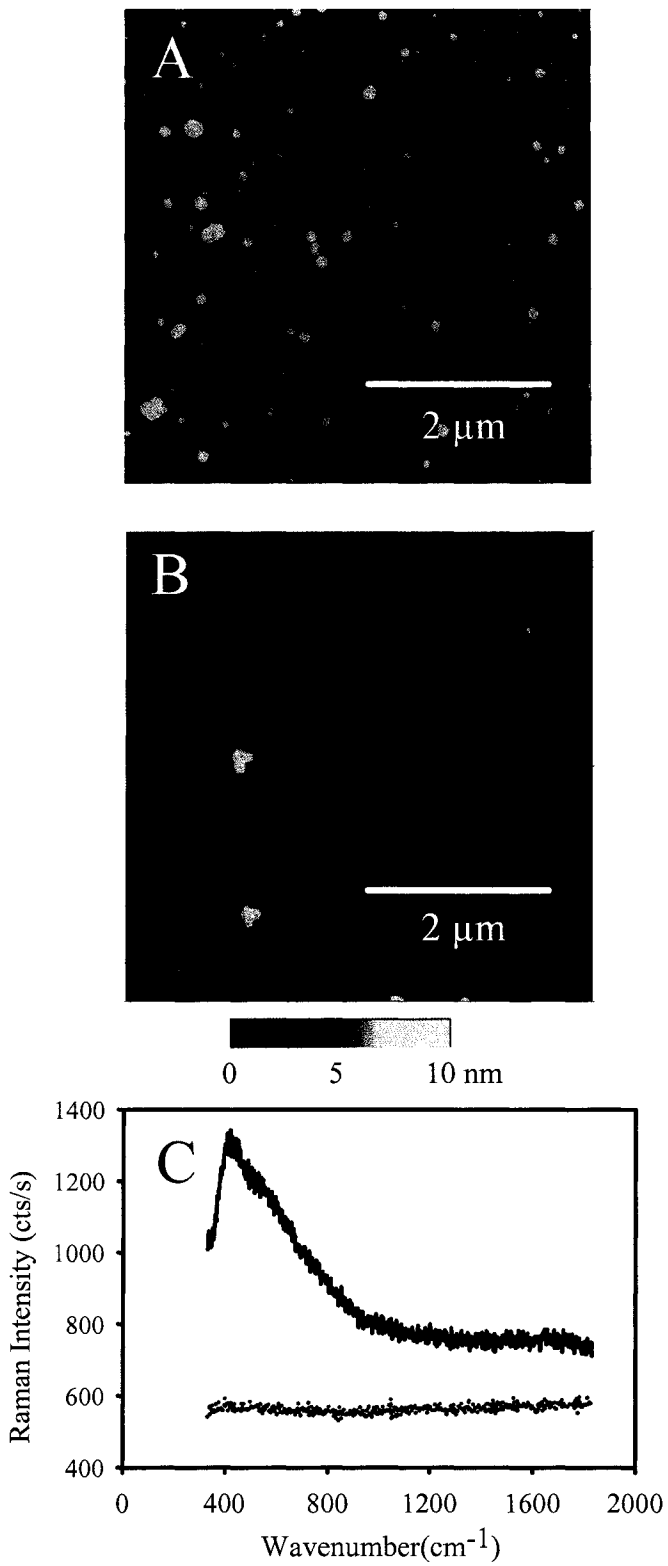
A
2 μm
B
2 μm
0
5
10 nm
C
Raman Intensity (cts/s)
1400
1200
1000
800
600
400
0
400
800
1200
1600
2000
Wavenumber(cm-1)

Figure 3.

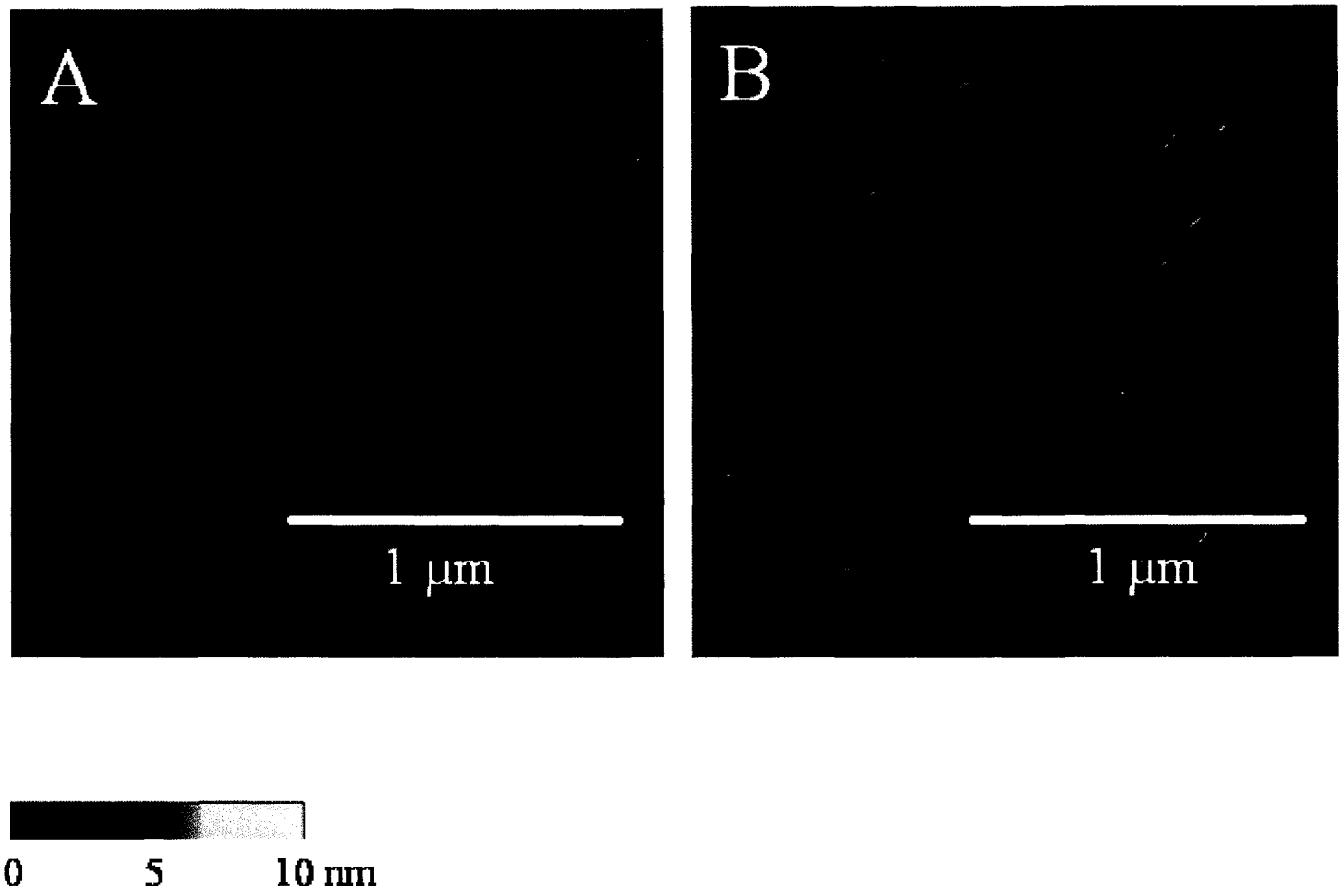

Figure 4.

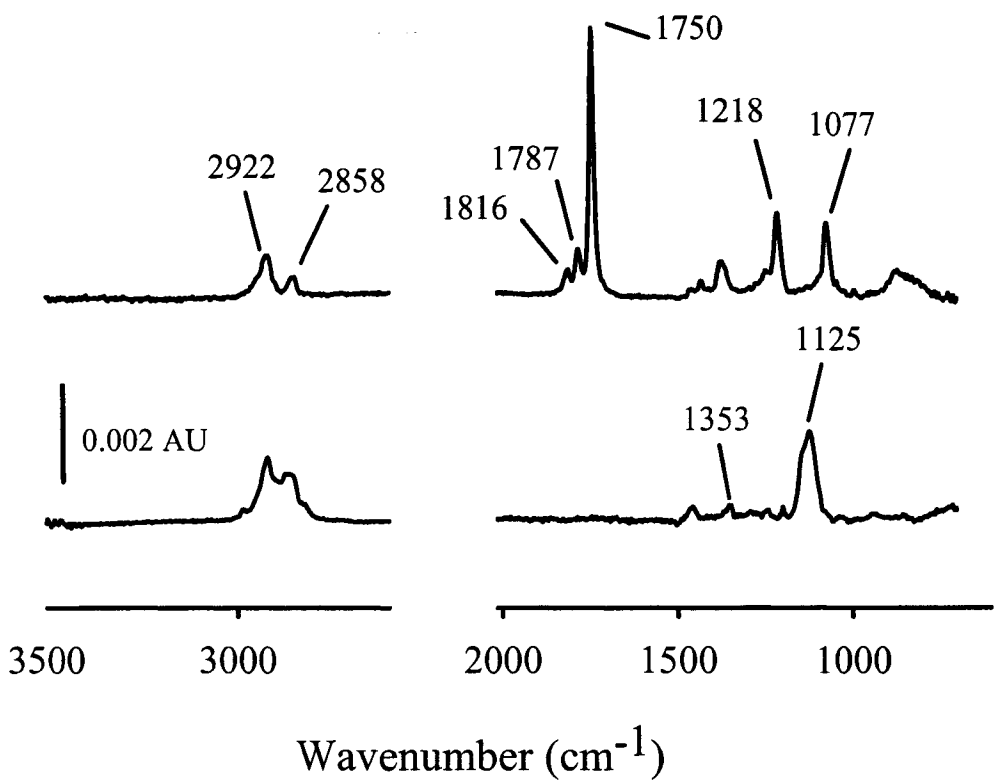
1750
1218
1077
1787
1816
2922
2858
1125
1353
0.002 AU
3500
3000
2000
1500
1000
Wavenumber (cm-1)

Figure 5.

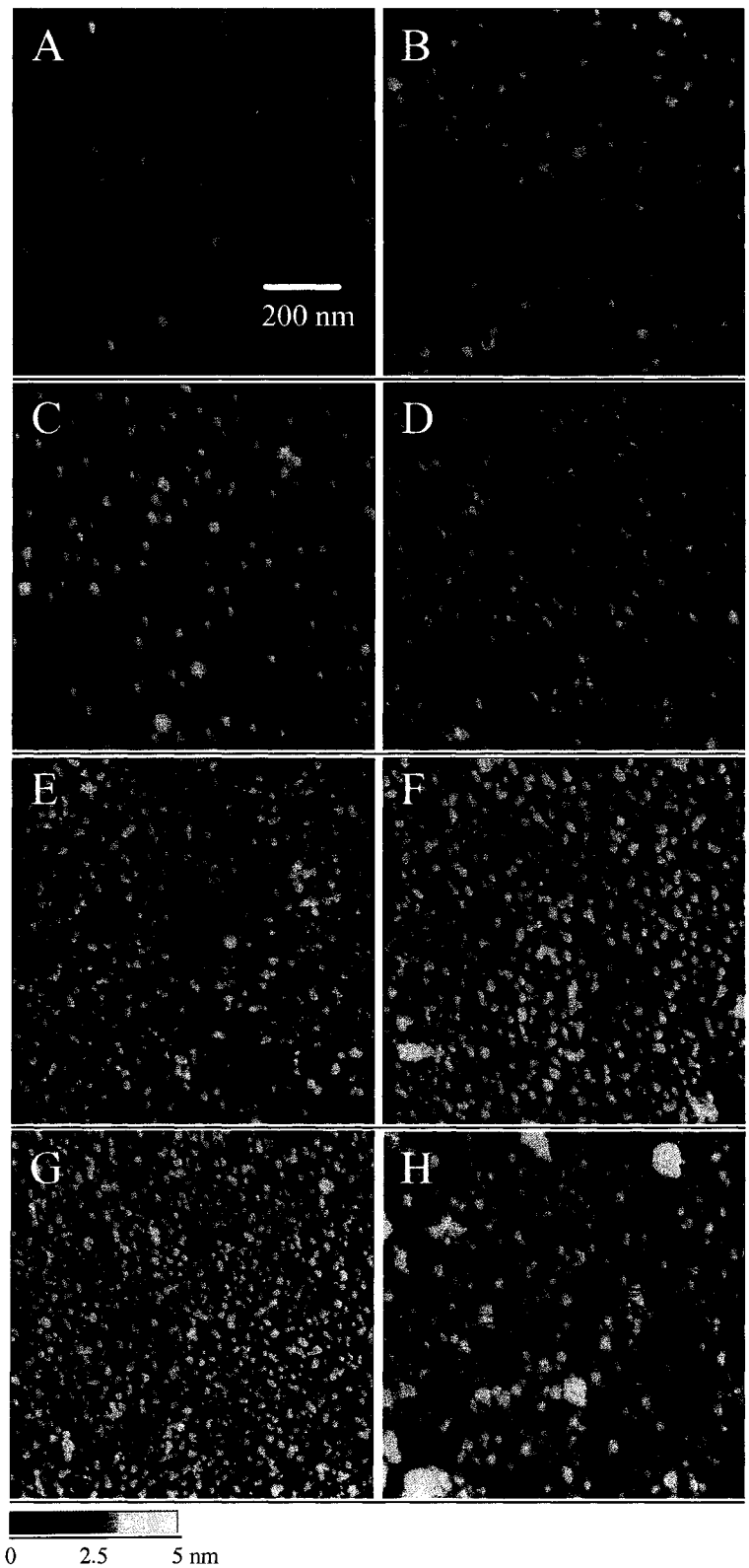

Figure 6.

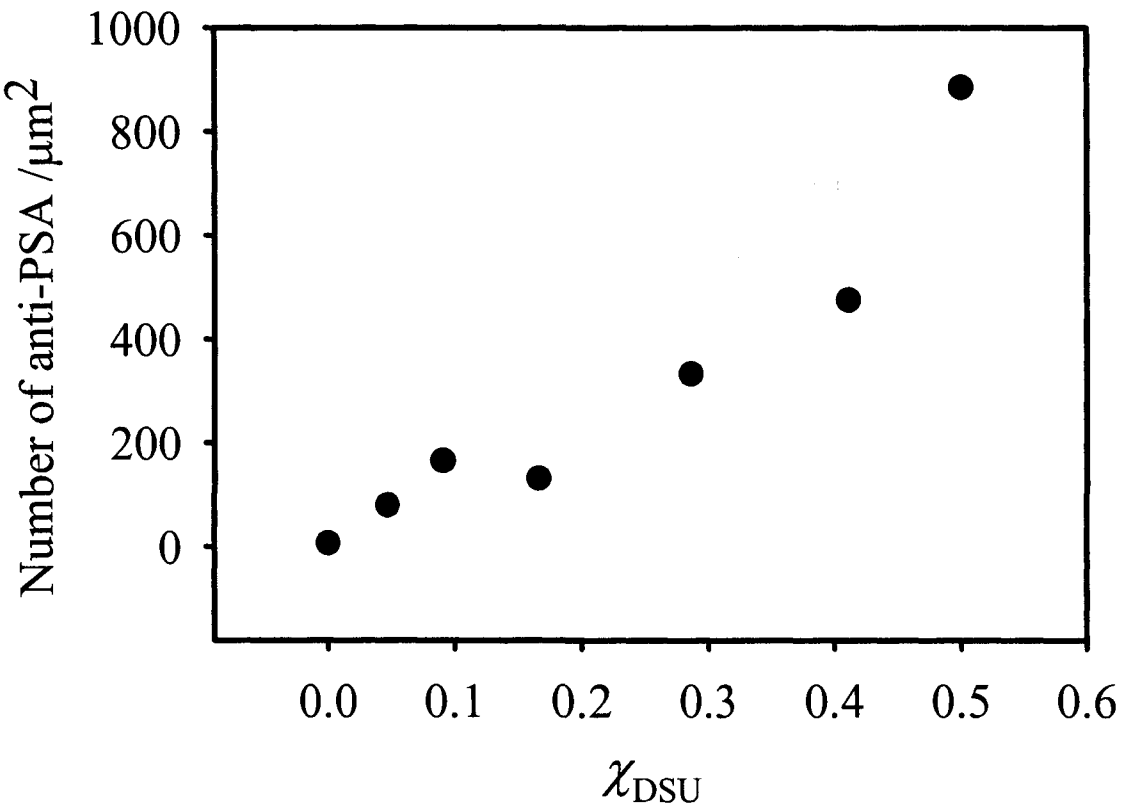
1000
800
600
400
200
0
Number of anti-PSA /μm2
0.0
0.1
0.2
0.3
0.4
0.5
0.6
χDSU

Figure 7.

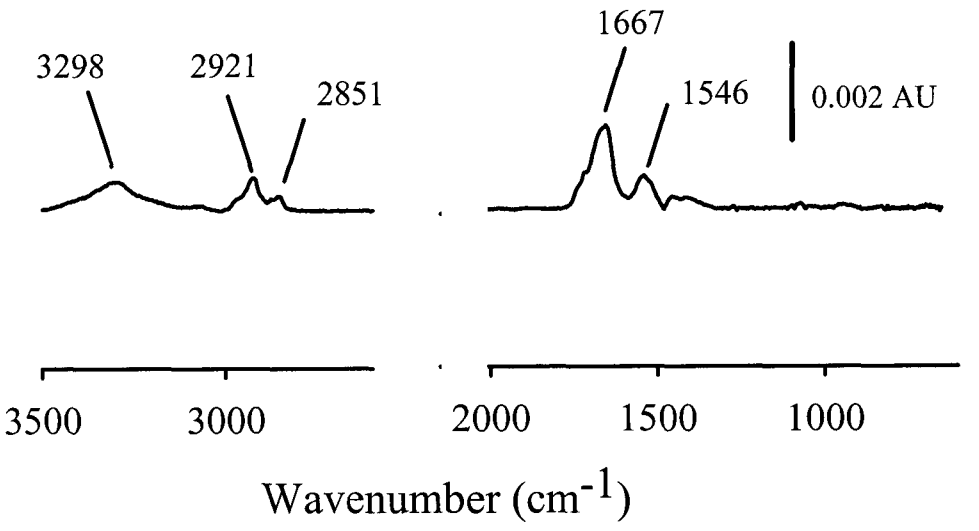
3298
2921
2851
1667
1546
0.002 AU
3500
3000
2000
1500
1000
Wavenumber (cm-1)

Figure 8.

CHAPTER 5. SINGLE MOLECULE ADSORPTION AT COMPOSITIONALLY PATTERNED SELF-ASSEMBLED MONOLAYERS ON GOLD: ROLE OF DOMAIN BOUNDARIES

A manuscript in preparation for submission to *Langmuir*

Hye-Young Park,[1] Hung-wing Li,[2] Edward S. Yeung,[2] and Marc D. Porter[1,3]

Abstract

This paper examines the single molecule adsorption of YOYO-I labeled λ-DNA at compositionally patterned self-assembled monolayers (SAMs). The interactions of fluorescently labeled λ-DNA molecule with the compositionally patterned SAMs comprised of different functional groups (i.e., amine-, alcohol- and acid- terminated thiols) was monitored using total internal reflection fluorescence microscopy (TIRFM) at optically transparent gold films. The role of solution pH, λ-DNA concentration, and domain size was investigated. In addition to further delineation of the relative adsorption strength as a function of the terminal group identity (NH_2 > COOH > OH), the potential importance of structural defects was also delineated. The latter result, found both at the disordered boundaries between domains and at adlayers in which structural order is affected by the length of the alkyl chain, points to the subtle but preferential adsorption of the "sticky ends"

[1] Ames Laboratory-USDOE, Departments of Chemistry and of Chemical and Biological Engineering, and the Institute for Combinatorial Discovery, Iowa State University, Ames, Iowa 50011.

[2] Ames Laboratory-USDOE, Department of Chemistry, Iowa State University, Ames, Iowa 50011.

[3] Corresponding author: (Tel) 515-294-6433; (Fax) 515-294-3254; (E-mail) mporter@porter1.ameslab.gov

of λ-DNA. These findings also demonstrated an intriguing dependence of preferential adsorption with respect to domain size.

Introduction

The dynamics of adsorption and retention of DNA at the liquid-solid interfaces are central to the development of biosensors, chip-scale platforms, and chromatographic materials.[1-5] Moreover, gaining fundamental insights into these dynamics is critical to cell and protein adhesion and numerous other areas in biotechnology.[6-18]

This paper extends our recent investigation in which the adsorption dynamics of fluorescently-labeled (YOYO-I), λ-DNA was monitored at the single molecule level at self-assembled monolayers (SAMs).[19] That work exploited the ability to construct substrates with well defined surface functionalities for use as models of various chromatographic packings by the chemisorption of thiols with different terminal groups on optically transparent gold films.[20-22] That work also took advantage of recent advances in the technical ability to directly monitor adsorption by single molecule spectroscopy;[23,24] these methods not only enable the direct observation of the real-time random motion of individual λ-DNA molecules, but can also collect high contrast images at a sub-millisecond temporal resolution and submicron spatial resolution.[25,26]

By coupling those two technologies, our earlier study began to delineate the importance of various interactions (e.g., electrostatic and hydrophobic) to λ-DNA adsorption at adlayers comprised of carboxylic acid-, hydroxyl-, EG3OMe- (triethylene glycol methyl ether), and methyl-terminal groups by the systematic manipulation of solution

pH. Furthermore, these experiments revealed that the exposed purine and pyrimidine groups at the 12-base, unpaired ends of λ-DNA (i.e., the "sticky ends") play an important role in the initial stages of the adsorption of each molecule. The work reported herein, designed to examine these systems in more detail, led to another interesting finding – the importance to adsorption of structural order and defects in the adlayer. This paper presents these observations and examines possible origins.

Experimental Section

Reagents. Mercaptohexadecanoic acid (MHDA), mercaptoundecanol (MUL), and mercaptohexanol (MHL) were purchased from Sigma-Aldrich. Aminoundecanethiol (AUT) was obtained from Dojindo. Millipore-purified deionized water (18 MΩ) was used for the preparation of all aqueous solutions. Two-part epoxy was obtained from Epotek.

Buffer solutions (pH 4.0-7.0) were prepared from 1.0 M aqueous solutions of acetic acid, sodium acetate and sodium chloride. A.C.S. grade or higher glacial acetic acid, sodium acetate and sodium chloride were purchased from Fisher Scientific. As detailed previously,[27] the final mass balance of acetate ion was 25 mM, as was the nominal ionic strength, unless otherwise specified. All the solutions were then photo-bleached for ~12 h under a mercury lamp and passed through a 0.2-μm filter immediately prior to use.

YOYO-labeled λ-DNA. λ-DNA (48502 bp) was obtained from Life Technologies. All DNA samples were prepared at a concentration of 500 pM in 10 mM Gly-Gly buffer, pH 8.2 (Sigma). λ-DNA, which has a fully extended length of ~16 μm,[27] was labeled with YOYO-1 (Molecular Probes) at a ratio of one dye molecule per five base pairs. These

solutions were diluted to 50 pM with each buffer prior to the start of a single molecule imaging experiment.

Substrate preparation. For the TIRFM studies, optically-transparent gold substrates were prepared. Glass coverslips (25 x 25 mm) were first cleaned by sonication in an aqueous detergent (Contrad), deionized water, and high purity methanol (30 min each). The cleaned coverslips were then placed in a high vacuum evaporator (Edwards) and coated with a 1-nm chromium adhesion layer, followed by a 20-nm film of gold (99.99% purity) at a deposition rate of 0.1-0.2 nm/s. This thickness of gold allowed adequate light transmission for TIRFM excitation while maintaining an effectively uniform coverage. Upon removal from the vacuum chamber, the substrates were either immediately modified or stored in a dessicator.

For AFM imaging, template stripped gold (TSG) samples were prepared via a previously reported procedure.[28] Silicon(111) wafers were cleaned by sequentially sonicating for 30 min in hexane, acetone, and methanol, and then dried under stream of high purity nitrogen. The cleaned wafers were placed in a vacuum evaporator and coated with 300 nm of gold. Next, glass slides were cut into 1 x 1 cm sections and cleaned by the same procedure used for the TIRFM substrates. After drying with a stream of nitrogen, a drop of Epotek 377 epoxy was applied to surface of the glass substrate, which was then affixed directly to the gold surface on the silicon wafer. This process sandwiches the gold film between the glass and silicon wafer. Preparation was completed by baking the sandwiched platform in a muffle furnace at 150 °C for 90 min. By carefully detaching the glass slide, a smooth gold surface is obtained.

Adlayer preparation and patterning. The compositionally patterned monolayers were prepared in a multi step process. SAMs were formed by immersing the gold substrates in ethanolic solutions of desired thiol solutions (1 mM) for ~20 h. Samples were rinsed with ethanol and dried under a stream of nitrogen gas.

Nickel transmission electron microscopy (TEM) grids and chromium patterned quartz plates were used as masks for UV photolithography. Both mesh [2000 mesh (hole size: 7.5 μm, bar size: 5 μm) and 600 mesh (hole size: 30 μm, bar size: 10-16 μm)] and parallel bar grids (bar width: 40 μm, bar spacing: 25 μm) (SPI Supplies) were employed. The mask was sandwiched between a monolayer-coated gold substrate and a quartz slide. A medium pressure mercury UV lamp was used at an irradiation time of 20 min. This process removes the monolayer exposed to the light that passes through the photomask by the generation of ozone, which creates various oxygenated forms of sulfur that can readily be removed by rinsing with water and other mild solvents.[29,30] These samples were then rinsed with deionized water and ethanol and dried under nitrogen. Finally, the samples were immersed into a second thiol solution, which filled in the uncoated regions of gold created by the photopatterning process. This step completes the fabrication of the compositionally pattered samples.

Total Internal Reflection Fluorescence Microscopy (TIRFM). Figure 1 shows a partial schematic of the experimental setup, which has been previously described.[27] An argon ion laser at 488 nm was used as an excitation source and was coupled to a Zeiss Axioskop microscope mounted with a CCD camera (Cascade 650, Roper Scientific) that was thermoelectronically cooled to -35°C. A 488-nm holographic notch filters was positioned between the objective and the CCD. With this setup, the angle of incidence at

the prism-sample interface was ~66°, which yielded an evanescent field thickness of ~150 nm. The 40x microscope objective (Zeiss Plan-Neofluar (oil 1.3 NA)) was optically coupled to the coverslip by immersion oil (type FF, n=1.48, Cargille). Single-molecule timing was performed using a mechanical shutter synchronized with the CCD. Finally, the optically transparent gold substrate was mounted on the fused silica prism.

Atomic Force Microscopy. All the AFM images were taken using Multimode AFM (Digital Instruments), equipped with a 125-μm tube scanner and operated in TappingMode™ at a scan rate of 1 Hz. The tips were silicon TESP probes (Nanosensors) with resonance frequencies between 298 and 365 kHz.

Results and Discussion

The interactions between DNA and the various modified surfaces include electrostatic, hydrogen bonding, and hydrophobic contributions. Interactions between neighboring λ-DNA adsorbates may also play an important role. The combined weight of these interactions, coupled with factors which affect solubility (e.g., pH and ionic strength), determines the strength of λ-DNA adsorption. Thus, by manipulating solution pH, interactions affecting λ-DNA adsorption can be probed.

In our earlier study using SAMs, the adsorption of λ-DNA increased as pH decreased.[19] This dependence primarily reflected the importance of electrostatics on solubility, which modulated the strength of interaction with the terminus of the adlayer. That study also showed that there were subtle differences in how the sticky ends of the

adsorbates interacted with polar terminal groups at low pH, which appeared to play a major role in the early stages of the adsorption process. The investigation herein was designed to examine these observations in more detail by using compositionally-patterned monolayers in which the direct comparison of adsorption at two different domains of functional groups would enable a more effective assessment of the relative strength of adsorption. Furthermore, these experiments were carried out to determine if the structural order of the adlayer contributed to adsorption, noting that SAMs with longer chain lengths are more ordered than those with shorter chain lengths.[31]

General observations. Figure 2 shows a series of TIRFM images for three different concentrations (20, 25, and 50 pM) of YOYO-I labeled λ-DNA at three different compositionally patterned adlayers (i.e., AUT/MHDA, MUL/MHDA, and MHL/MUL). These images are representative of those from a much larger data set that spanned pH values from 4.0 to 8.2, and correspond to pH values in which preferential adsorption at one of the two domains for a patterned adlayer was first observed as the pH was lowered. The set of images in Figure 2A therefore correspond to those for a patterned adlayer composed of an amine-terminated adlayer (AUT) in the square-shaped addresses and a carboxylic acid-terminated adlayer (MHDA) in the grid regions, with the leftmost image at a λ-DNA concentration of 50 pM and the center and rightmost images at 25 and 20 pM, respectively. The images in Figures 2B,C follow the same order with respect to λ-DNA concentration. However, those in Figure 2B are images for a surface patterned using the parallel bar grid and is composed of a carboxylic acid-terminated adlayer in the wider lanes and a hydroxyl-terminated adlayer in the narrower lanes. Furthermore, Figure 2C represents the results at a surface composed of hydroxyl-terminated SAMs, with the square-shaped islands

modified with a longer chain adlayer (11 methylene groups) and the grid regions derivatized with a shorter adlayer (six methylene groups).

From a compositional viewpoint, the differences in the images presented in Figures 2A-1 and 2B-1 are qualitatively comparable to those in our earlier report.[19] Figure 2A-1 shows a clear preference for adsorption at the amine-terminated islands over the carboxylic acid terminated grids around these islands. This result is attributed to the presence of protonated amines and deprotonated carboxylic acids at pH 8.2.[32-34] The driving force for the adsorption of negatively charged λ-DNA is therefore electrostatically favored at the AUT-derived islands. This preference in adsorption continues as the pH is lowered (data not shown). However, the magnitude of the difference diminishes, with both domains showing comparable levels of adsorption at pH 5.0 and lower. Moreover, the number of adsorbed molecules undergoes an increase with decreasing pH. The evolution of these observations is ascribed in large part to a contribution of electrostatic interactions (i.e., the reduction in the total negative charge of λ-DNA and the change in the extent of ionization of the terminal groups at the AUT and MHDA domains). More detailed studies, including assessments of the acid strengths of the two terminal groups, will be necessary in order to unravel the contributions of these and other (e.g., hydrophobic) factors.

Closer inspection of Figure 2B-1 reveals another intriguing spatial dependence of adsorption – the tendency for adsorption at the boundary between domains (i.e., an "edge effect"). This result points to the potential role of defects in the adlayer with respect to adsorption in a manner that resembles, at least in part, the mixed mode adsorption phenomenon described by various chromatographic theories.[35]

Along the same lines, Figure 2C-1 shows favored adsorption at the short chain (MHL) over the long chain (MUL) hydroxyl-modified surface at pH 5.0. Increases in pH revealed a decrease in the extent of adsorption, but little observable differentiation at the two domains. Decreases in pH led to an increase in the number of adsorbed λ-DNA; however, subtle differences in preferential adsorption were observed in only a few images. These findings are consistent with the lower order with respect to chain packing of shorter chain monolayers, which exposes more of the hydrophobic interior of the adlayer for interactions with the sticky ends of λ-DNA.

Concentration dependence. To investigate the observed edge effect further, the concentration dependence of adsorption was examined at the same three types of patterned samples and at the sample pH values used in the images described in the last subsection. Two different λ-DNA concentrations were tested, 20 and 25 pM, and are represented by the images in the rightmost and center panels of Figures 2A-C, respectively. All the images exhibit the same preference for adsorption with respect to the identity of the terminal group and chain length as found at the 50 pM concentrations. These results also show that the adsorption of λ-DNA is partially favored at domain boundaries. In fact, the edge effect is more apparent at the two lower concentrations, with adsorbed λ-DNA outlining the boundaries between the islands and grids in the images sets in Figures 2A, C, and those between the lanes in Figure 2B.

Some of the lower concentration images also showed λ-DNA anchored with one end located at a boundary and its opposite end at a neighboring domain boundary. An example of this observation is given in Figure 2A-2. This patterned adlayer has a separation between the amine-terminated domains of 5-7 μm, which is less then the length (~16 μm) of an

extended λ-DNA molecule. Note also that the bridging adsorbates are extended along the same general direction. This situation, as discussed by Kang *et al.*,[27] reflects the low level of solution flow (20-200 nm/ms) across the surface that can be induced by the coverslip when placed on top of the sample solution immediately before an experiment begins. Other images, in contrast, show extended sections of λ-DNA that appear to have both ends adsorbed in the same domain, or have one end fixed at a domain boundary and the other in the surrounding grid. The image in Figure 2C-1 is an example of such an observation, and is a reflection of the distance (30-40 μm) between the square-shaped islands being greater than the fully extended length of λ-DNA.

These results collectively argue that the adsorption of λ-DNA is a complex process, especially at surfaces with the heterogeneity of our patterned adlayers. Moreover, the observed preferential adsorption at the domain boundaries for samples composed of the hydroxyl-terminated adlayers with different chain lengths points to structural disorder as an important contributor to this tendency.

AFM characterization of the domain boundaries. As a further investigation of the origins of the edge effects, AFM imaging was used to examine the structural topography across the patterned samples. These experiments were carried out using samples prepared on the atomically smooth surfaces of TSG. Figure 3 shows topographic AFM images for (A) AUT(square)/MHDA(grid), (B) MUL(square)/MHDA(grid), and (C) MHL(square)/MUL(grid), and their respective cross-sectional plots. Each image contains features tractable to the photopatterning process. More importantly, some of the images display an obvious disruption in topography at the domain boundaries. Figure 3A, for example, exhibits an almost undetectable difference in the absolute height of the two

domains, but clearly undergoes a large drop in height at the domain boundary. These changes, while less than the thickness of either adlayer, are between 700 and 900 nm in width. This finding represents, we believe, the uncertainty in the edge definition from the photopatterning process, which relies on the gradual top-down degradation of the adlayer by UV-generated ozone.[29,36]

The same qualitative description applies to the image in Figure 3B, noting that the structural variations in the AFM-measured depth and width at the domain boundaries are less then in Figure 3A. Some samples, like that in Figure 3C, did not show an obvious disruption in topography at the domain boundary. Together, these images reveal that there is often a structural irregularity in the sample at the domain boundaries.

Adsorption dependence on immersion time for adlayer formation. As another investigation of role of edge effects on λ-DNA adsorption, a preliminary study of the influence of the immersion time employed for the formation of a MHDA adlayer, which is known to alter the packing density of SAMs,[31] was carried out. This study, summarized in Figure 4, revealed that the number of λ-DNA molecules which are permanently adsorbed on the MHDA surface was significantly higher for samples with an immersion time shorter than 10 s. At a 1-s immersion time, the number of λ-DNA permanently adsorbed (~200 per image) was comparable to that on bare gold at the same pH (4.5). However, the adsorption of λ-DNA decreased rapidly as immersion time increased, reaching to the minimum at ~30 s to 1 h. This change is consistent with the formation of a MHDA-derived monolayer on the gold surface. Interestingly, the amount of adsorbed λ-DNA then undergoes an increase at longer immersion times. We, at present, suspect that this increase results from the formation of hydrogen-bonds between the partially ionized acidic terminus of the adlayer.

Recent work has indicated that the driving force for hydrogen-bonding is more than sufficient to overcome the barrier to form gauche kinks that would potentially impede hydrogen-bonding.[37] It was also proposed that the formation of hydrogen-bonds exposed portions of the methylene spacer groups, which would provide a hydrophobic site for adsorption of the λ-DNA sticky end. Clearly, a more in-depth series of investigations along these lines are needed. These results nevertheless begin to support the importance of structural disorder to λ-DNA adsorption.

Patterns with Smaller Domains. Lastly, the effect of domain size was examined by creating compositionally patterned adlayers using the same UV photopatterning technique but with a chromium mask composed of circular holes having a 3-μm diameter. Samples composed of an AUT-based monolayer formed in the circular addresses that were surrounded by MHDA were studied. The results are presented in Figure 5. As is evident, the surfaces exhibit clear evidence for adsorption at one domain (AUT) over the other (MHDA). These findings are diagnostic of the larger strength of adsorption for λ-DNA at the amine-terminated groups, which are protonated at this pH, with respect to all the other terminal groups tested. There is another interesting aspect from this set of experiments. Only a few (1-3) adsorbates were found in each circular domain. At the 3-μm addresses, the average area per adsorbate, when we consider the area of each address (~7 μm^2), spans from 2 to 7 μm^2. Presumably the steric interference of λ-DNA molecules with one another prevented higher adsorption densities.

Conclusions

This paper examined the adsorption of individual λ-DNA molecules at compositionally patterned SAMs. λ-DNA showed a preferential adsorption onto one component that was pH and domain size dependent. These differences result from the combination of electrostatic, hydrogen-bonding, and hydrophobic interactions as well as steric effects. In addition, surface topology affected the initial stages of adsorption; i.e., λ-DNA was preferentially anchored at the boundary between two adlayers. This effect was also observed using an adlayer formed from thiols with a shorter chain length. Experiments are currently being designed to further examine the fundamental underpinnings of each of these intriguing observations.

Acknowledgments

This work was supported by the Institute for Combinatorial Discovery of Iowa Sate University and the Ames Loboratory-U.S.D.O.E. The Ames Laboratory is operated for the U. S. Department of Energy by Iowa State University under contract W-7405-eng-82.

References

(1) Scotchford, C. A.; Gilmore, C. P.; Cooper, E.; Leggett, G. J.; Downes, S. *J. Biomed. Mater. Res.* **2002**, *59*, 84.

(2) Raut, V. P.; Agashe, M. A.; Stuart, S. J.; Latour, R. A. *Langmuir* **2005**, *21*, 1629.

(3) Frutos, A. G.; Brockman, J. M.; Corn, R. M. *Langmuir* **2000**, *16*, 2192.

(4) Gillmor, S. D.; Thiel, A. J.; Strother, T. C.; Smith, L. M.; Lagally, M. G. *Langmuir* **2000**, *16*, 7223.

(5) Schouten, S.; Stroeve, P.; Longo, M. L. *Langmuir* **1999**, *15*, 8133.

(6) Keller, C. A.; Kasemo, B. *Biophys. J.* **1998**, *75*, 1397.

(7) Ostuni, E.; Yan, L.; Whitesides, G. M. *Colloids Surf., B* **1999**, *15*, 3.

(8) Gaus, K.; Hall, E. A. H. *Anal. Chim. Acta* **2002**, *470*, 3.

(9) Chapman, R. G.; Ostuni, E.; Yan, L.; Whitesides, G. M. *Langmuir* **2000**, *16*, 6927.

(10) Jordan, C. E.; Corn, R. M. *Anal. Chem.* **1997**, *69*, 1449.

(11) Silin, V.; Weetall, H.; Vanderah, D. J. *J. Colloid Interface Sci.* **1997**, *185*, 94.

(12) Mrksich, M.; Grunwell, J. R.; Whitesides, G. M. *J. Am. Chem. Soc.* **1995**, *117*, 12009.

(13) Singhvi, R.; Kumar, A.; Lopez, G. P.; Stephanopoulos, G. N.; Wang, D. I. C.; Whitesides, G. M.; Ingber, D. E. *Science (Washington, DC, United States)* **1994**, *264*, 696.

(14) Lahiri, J.; Ostuni, E.; Whitesides, G. M. *Langmuir* **1999**, *15*, 2055.

(15) Roberts, C.; Chen, C. S.; Mrksich, M.; Martichonok, V.; Ingber, D. E.; Whitesides, G. M. *J. Am. Chem. Soc.* **1998**, *120*, 6548.

(16) Mark Sonny, S.; Sandhyarani, N.; Zhu, C.; Campagnolo, C.; Batt Carl, A. *Langmuir* **2004**, *20*, 6808.

(17) Gani, S. A.; Mukherjee, D. C.; Chattoraj, D. K. *Langmuir* **1999**, *15*, 7130.

(18) Wang, Y.; Vaidya, B.; Farquar, H. D.; Stryjewski, W.; Hammer, R. P.; McCarley, R. L.; Soper, S. A.; Cheng, Y.-W.; Barany, F. *Anal. Chem.* **2003**, *75*, 1130.

(19) Li, H.-W.; Park, H.-Y.; Porter, M. D.; Yeung, E. S. *Anal. Chem.* **2005**, *77*, 3256.

(20) Chen, C. S.; Mrksich, M.; Huang, S.; Whitesides, G. M.; Ingber, D. E. *Science (Washington, D. C.)* **1997**, *276*, 1425.

(21) Lopez, G. P.; Albers, M. W.; Schreiber, S. L.; Carroll, R.; Peralta, E.; Whitesides, G. M. *J. Am. Chem. Soc.* **1993**, *115*, 5877.

(22) Mrksich, M.; Chen, C. S.; Xia, Y.; Dike, L. E.; Ingber, D. E.; Whitesides, G. M. *Proc. Natl. Acad. Sci. U.S.A.* **1996**, *93*, 10775.

(23) Antia, M.; Islas, L. D.; Boness, D. A.; Baneyx, G.; Vogel, V. *Biomaterials* **2005**, *27*, 679.

(24) Friedsam, C.; Seitz, M.; Gaub, H. E. *J. Phys.: Condens. Matter* **2004**, *16*, S2369.

(25) Xu, X.-H.; Yeung, E. S. *Science (Washington, D. C.)* **1997**, *275*, 1106.

(26) Xu, X.-H. N.; Yeung, E. S. *Science (Washington, D. C.)* **1998**, *281*, 1650.

(27) Kang, S. H.; Shortreed, M. R.; Yeung, E. S. *Anal. Chem.* **2001**, *73*, 1091.

(28) Stamou, D.; Gourdon, D.; Liley, M.; Burnham, N. A.; Kulik, A.; Vogel, H.; Duschl, C. *Langmuir* **1997**, *13*, 2425.

(29) Lewis, M.; Tarlov, M.; Carron, K. *J. Am. Chem. Soc.* **1995**, *117*, 9574.

(30) Norrod, K. L.; Rowlen, K. L. *Anal. Chem.* **1998**, *70*, 4218.

(31) Porter, M. D.; Bright, T. B.; Allara, D. L.; Chidsey, C. E. D. *J. Am. Chem. Soc.* **1987**, *109*, 3559.

(32) Sugihara, K.; Shimazu, K.; Uosaki, K. *Langmuir* **2000**, *16*, 7101.

(33) Wang, J.; Frostman, L. M.; Ward, M. D. *J. Phys. Chem.* **1992**, *96*, 5224.

(34) Matulis, D.; Bloomfield, V. A. *Biophys. Chem.* **2001**, *93*, 37.

(35) Hancock, W. S.; Sparrow, J. T. *J. Chromatogr.* **1981**, *206*, 71.

(36) Ye, T.; McArthur, E. A.; Borguet, E. *J. Phys. Chem. B* **2005**, *109*, 9927.

(37) Arnold, R.; Azzam, W.; Terfort, A.; Woell, C. *Langmuir* **2002**, *18*, 3980.

Figure Captions

Figure 1. Experimental setup: (A) sample mounted on fused silica prism and optically coupled with microscope objective for monitoring the movement of single λ-DNA molecule excited in the evanescent field; (B) sample solution with λ-DNA interacting with patterned SAM surfaces on optically transparent gold film.

Figure 2. Fluorescence images (60 x 80 μm) at three different compositionally patterned adlayers as a function of YOYO-I- λ-DNA molecules concentration: (A) AUT(square)/MHDA(grid) (pH 8.2, 25 mM Gly-Gly buffer solution) using 2000 mesh TEM grids; (B) MUL(lane)/MHDA(grid) (pH 5.0, 25 mM sodium acetate/acetic acid) using parallel bar TEM grids; and (C) MHL(square)/MUL(grid) (pH 5.0, 25 mM sodium acetate/acetic acid) using 600 mesh TEM grids. In each case, the concentration of λ-DNA in the leftmost, middle, and rightmost frames equaled 20, 25, and 50 pM, respectively.

Figure 3. Topographic AFM images and corresponding cross section plots for three different compositionally patterned adlayers: (A) AUT(square)/MHDA(grid); (B) MUL(square)/MHDA(grid); and (C) MHL(square)/MUL(grid). The spikes in the cross sectional view in Figure C are due to the defects on TSG surfaces.

Figure 4. Plot of λ-DNA surface concentration on a MHDA adlayer as a function of immersion time for adlayer formation. These measurements were carried out using 50 pM of YOYO-I labeled λ-DNA (pH 4.5, 25 mM sodium acetate/acetic acid) was pipetted on the substrate.

Figure 5. (A) Fluorescence images (60 x 80 μm) of YOYO-I labeled λ-DNA at AUT(circle, 3 μm)/MHDA(grid, 10 μm) (pH 8.2, 25 mM Gly-Gly buffer solution). The concentration of DNA was 50 pM. (B) A topographic AFM image and corresponding cross section analysis of the AUT(circle)/MHDA(grid).

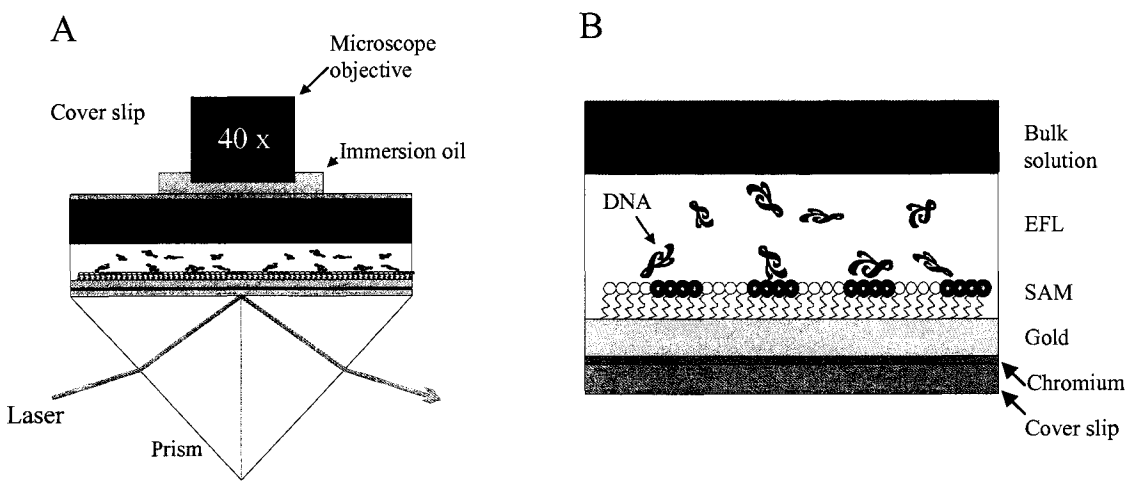
A
Microscope objective
Cover slip
40 x
Immersion oil
Laser
Prism
B
Bulk solution
DNA
EFL
SAM
Gold
Chromium
Cover slip

Figure 1.

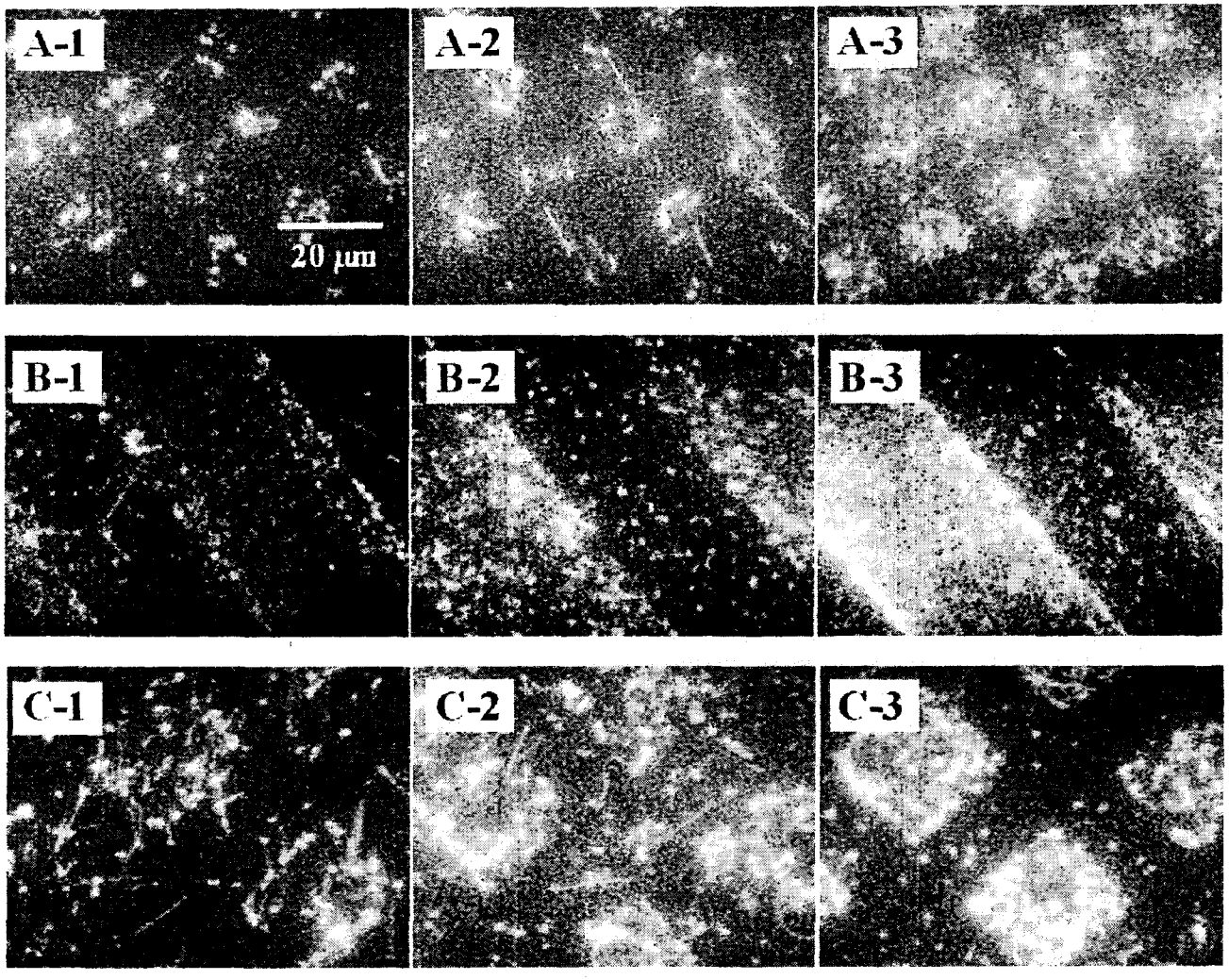

Figure 2.

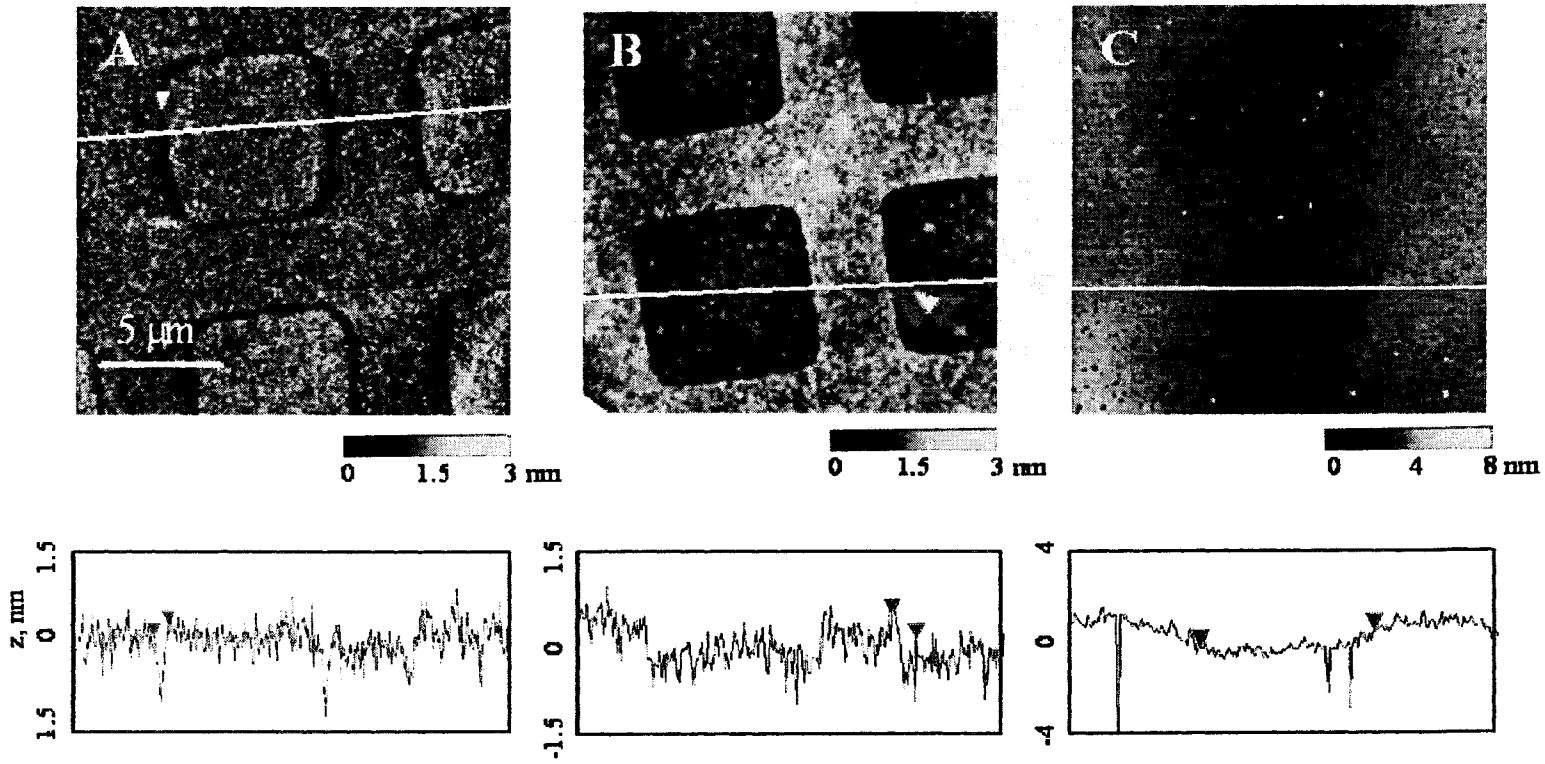

Figure 3.

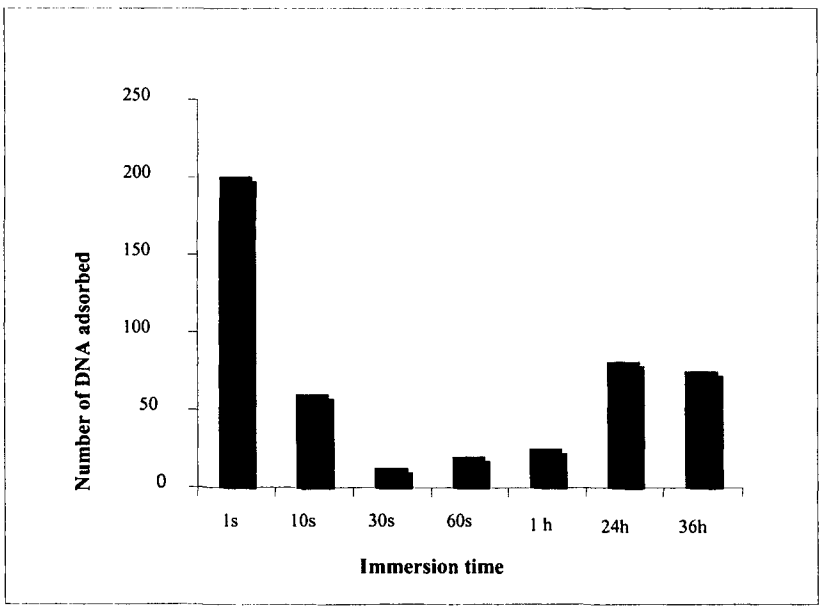
250
200
150
100
50
0
Number of DNA adsorbed
1s
10s
30s
60s
1 h
24h
36h
Immersion time

Figure 4.

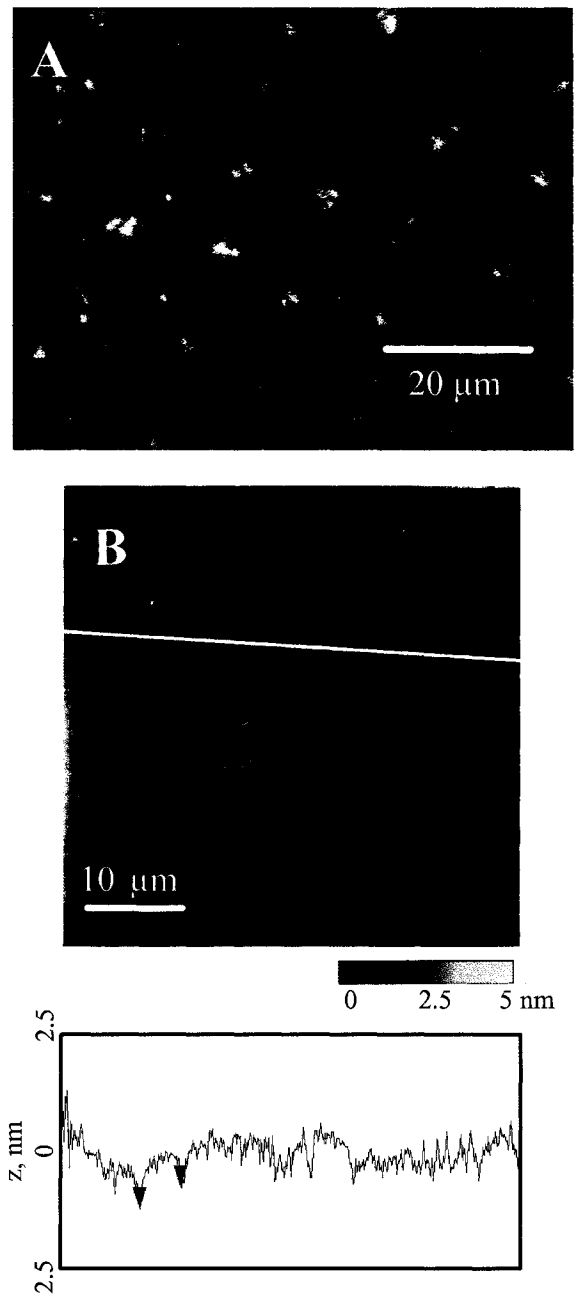

Figure 5.

CHAPTER 6. GENERAL CONCLUSIONS AND PROSPECTUS

This dissertation has explored the development and application of a high sensitivity immunoassay readout method based on SERS. Chapter 2 explored the effect of particle size on SERS signal employed in sandwich immunoassays. Sandwich immunoassays of f-PSA were performed using ERLs created from various sizes of gold nanoparticles. By correlating SERS signal and AFM particle analysis, average SERS signal per particle was obtained as a function of particle size. Also, SERS signal from individual gold particles coated with Raman reporter molecule DSNB was recorded using an in-house assembled Raman-microscope. The results show that SERS signal increases as particle size increases for particle sizes tested (30-80 nm) on assay substrate. Single gold nanoparticle SERS showed consistent results where particles larger than 70 nm gave the largest signals.

Chapter 3 demonstrated the application of ERLs in the detection of *Erwinia herbicola* and *Bacillus globigii,* simulants for biological warfare agents and the pathogen *Escherichia coli* O157:H7. ERLs prepared by 80-nm gold nanoparticle were utilized and showed low level detection of the analytes. The limit of detection (LOD) for *E. coli* O157:H7 was 1,000-2,000 cells/mL, with those for *E. herbicola* and *B. globigii*, roughly 8,000 and for 4,000 cfu/mL, respectively. A new ERL scheme based on mixed monolayer was created by covering the gold nanoparticles with a mixture of two thiolates, one covalently binds antibody to the particle and the other produces a strong Raman signal. The mixed monolayer ERLs were applied in the detection of IgGs and bacteria and have shown to perform as well as ERLs based on bifunctional reporter molecule.

Chapter 4 introduced assay platform based on mixed SAMs of DSU and EG3OMe-terminated thiol. Mixed SAMs prepared from ethanolic solution with mixture of

DSU and EG3OMe with various fraction of DSU. Then, the mixed SAMs were incubated with anti-PSA. Using AFM, individual anti-PSA was imaged and counted. The results revealed that the number of immobilized anti-PSA increased as χ_{DSU} increased. Use of EG3OMe terminated thiol showed ability to resist binding of protein. The covalent binding of antibody onto DSU- derived monolayer region was evident as verified by IRRAS.

Chapter 5 described adsorption behavior of single YOYO-1 labeled λ-DNA at compositionally patterned SAMs. Patterned SAMs were created with various combinations of thiolates with different functional groups, i.e., -COOH, $-NH_2$, -OH via UV photopatterning process. TIRFM was used to monitor adsorption of individual λ-DNA on the substrates as a function of solution pH and concentration of λ-DNA. The study revealed that λ-DNA preferentially adsorbed on one component showing clear patterns with dimensions comparable to those of photomasks at carefully controlled pH. This behavior was attributed to the fact that balances between the interactions governing the adsorption of λ-DNA, i.e. electrostatic, hydrophobic, and hydrogen bonding interactions, changed as pH changed. Defect sites, chain length of the thiolate, and domain size also played a role in giving preferential adsorption of λ-DNA. λ-DNA initially adsorbed onto the boundary regions of the addresses which exhibit topographical defects as verified by AFM. This study showed the ability of λ-DNA to probe both chemical and physical heterogeneity.

The ability to measure signal from single nanoparticle allows us to study fundamental aspects of SERS. The difficulty in performing experiments to elucidate the size-, shape-, particle-particle interaction-, particle-substrate interaction- dependence of SERS has been mainly due to the difficulty in creating surfaces with high reproducibility

and defined shapes, i.e. controlling surface morphology. By using single-nanoparticle SERS, signal from individual particles with different shape and particle-particle distance and particle-substrate distance can be directly measured. With modeling and theoretical work for more complex systems, the origin of the enhancement of SERS can be better understood.

SERS based immunoassays will continue to find their applications in real world analytes as instrumentation develops to create hand-held device that will allow field-deployable system. Potential improvements can also come from sample introduction, i.e. microfluidic device which will allow high throughput analysis with minimum sample consumption, as well as sample preconcentration. While SERS based readout methods perform well for single analyte assays with ultra-low level of detection and for yes/no type dual-analyte assays, there are still issues to be addressed regarding quantitative dual- or multi- analyte assays. The problem may have come from, as discussed earlier, the difference in binding affinities between different ERLs. Therefore, assay platform with controlled antibody density (studied in Chapter 4) can be applied to further investigation. For example, the surface can be used to study viability of antibody. Also, incorporation of the platform in the dual- or multi- analyte assay can provide a capture surface with minimal steric hindrance in SERS based assay.